Polymer Design and Processing for Liquid-Core waveguides

Sagar, Kaushal Shashikant; Hassager, Ole; Ndoni, Sokol; Christiansen, Mads Brøkner

Publication date:
2012

Document Version
Publisher's PDF, also known as Version of record

Polymer Design and Processing for Liquid-Core Waveguides

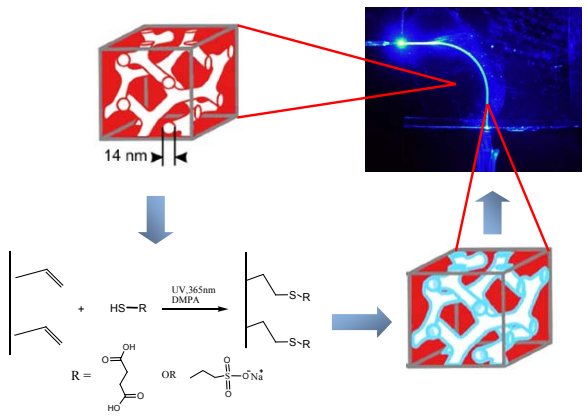

Kaushal Shashikant Sagar

Ph.D. Thesis

December 2011

DTU Chemical Engineering
Department of Chemical and Biochemical Engineering

Polymer Design and Processing for Liquid-Core Waveguides

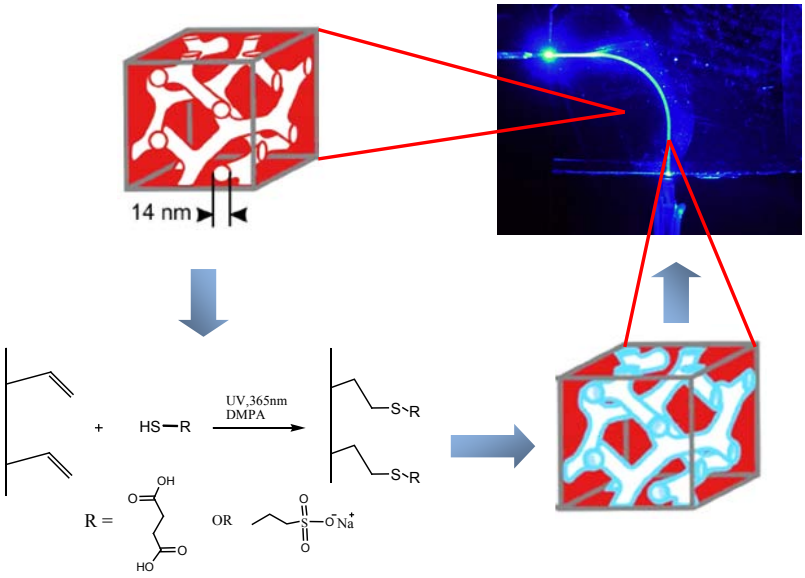

PhD thesis

Kaushal Shashikant Sagar

2011

DTU Chemical Engineering
Department of Chemical and Biochemical Engineering

Address: The Danish Polymer Centre
Department of Chemical and Biochemical Engineering
Technical University of Denmark
Building 227
DK-2800 Kgs. Lyngby
Denmark
Phone: +45 4525 2800
Web: www.dpc.kt.dtu.dk

Print: J&R Frydenberg A/S
København
April 2012

ISBN: 978-87-92481-68-9

Polymer Design and Processing for Liquid-Core Waveguides

Danish Polymer Center

Department of Chemical and Biochemical Engineering

Kgs. Lyngby Denmark

Kaushal Shashikant Sagar

December 2011

DTU Chemical Engineering
Department of Chemical and Biochemical Engineering

बुद्धियुक्तो जहातीह उभे सुकृतदुष्कृते
तस्माद्योगाय युज्यस्व योगः कर्मसु कौशलम्॥

Endowed with equanimity, one sheds in this life both good and evil.
Therefore, strive for the practice of this Yoga of equanimity.
Skill in action lies in (the practice of this) Yoga.

Acknowledgement

The work described here as PhD thesis is undertaken at the Danish Polymer Centre, Department of Chemical Engineering (KT), Technical University of Denmark (DTU) and Department of Micro and Nano technology (Nanotech), DTU Denmark and pursued for the period from 15 July 2008 to 14 July 2011. This Ph.D work is supervised by Professor Ole Hassager, DTU KT, Senior Scientist Sokol Ndoni, DTU Nanotech and Postdoc Mads Brøkner Christiansen, DTU Nanotech. The project was funded by the Danish Council for Strategic Research through project LiCorT (grant no. 09-063776/DSF) and by Department of Chemical & Biochemical Engineering.

I wish to convey sincere gratitude to my supervisor Ole Hassager for giving me the opportunity to carry out the PhD work. I would like to specially acknowledge Sokol Ndoni and Mads Christiansen for their tremendous support, cooperation, active participation and stimulating suggestions throughout the entire work period. I am sincerely indebted to Professor Anders Kristensen, DTU Nanotech and Peter Thomsen, Biomodics, Denmark for their active participation in the project, for the valuable discussions, suggestions and motivational talks. I appreciate kind cooperation from my project partners Nimi Gopalakrishnan and Anton Berthold. Their support, countless brainstorming sessions, and friendly outlook are highly acknowledged during the current work. I also take an opportunity to thank Professor Martin E. Vigild, DTU for giving me an opportunity to work with Nanoporous group and his guidance in the initial phase of my Ph.D.

I thank the entire Nanoporous group for hosting my first research endeavour and nourishing it for over 4 years. I would like to express my sincere gratitude to Lars Schulte, whose skilful inputs with polymer chemistry and microscopy are highly cherished. I thank some of the past members of nanoporous group, Li Li, Piotr Szewczykowski, Fengxiao Guo for the helpful discussions and friendly attitude which made a considerable difference both on the academic and personal front.

I thank Annette Christensen, Roskilde University for her assistance with solid state NMR spectroscopy and Lotte Neilsen, Nanotech DTU for her prompt assistance on various occasions. I also would like to thank Center for Electron Nanoscopy DTU, for stage-managing my microscopy experiments during the tenure of the Ph.D work.

I am greatly indebted to all my colleagues at Danish Polymer Center for their assistance with technical, practical and personal issues during my Ph.D work.

Last but perhaps the most important contribution which needs special mention is from my wife, Nehal. I thank her for being there for me, bolstering my confidence during the testing times and understanding my irrational behavior on many occasions. I am also grateful to my family and friends for their endless encouragement and great affection which has always guided me in my work.

December 2011, Kgs. Lyngby Kaushal Shashikant Sagar

Denmark

Abstract

Block copolymers are known for their self-assembling ability utilized for bottom-up nanostructure fabrication. It is particularly capitalized in the context of present work where nanoporous scaffolds are created from a 1,2-polybutadiene-*b*-polydimethylsiloxane (1,2-PB-*b*-PDMS) block copolymer precursor material. Upon attaining thermodynamically stable gyroid phase segregation, nanoporosity is induced by chemically removing PDMS, the so-called sacrificial block. The isotropic nanoporosity in the polymer is utilized in fabricating a novel type of waveguides for opto-fluidic applications, which we call solid-liquid core waveguides, shortly SLCW. The high refractive index core of a SLCW consists of nanoporous polymer (solid) rendered hydrophilic and filled with water (liquid), while the low refractive index cladding consists of air-filled hydrophobic nanoporous polymer. Under conditions of total internal reflection, light is confined within the solid-liquid core. Controlled regions of the originally hydrophobic nanoporous 1,2-PB are rendered hydrophilic by photochemical modification of the polymer in the presence of photo-lithographic masks. In contact with water the hydrophilic regions are spontaneously filled with water by capillary suction, forming the core, while the unmodified hydrophobic regions remain dry, forming the clad. Two types of photo-modification reactions are presented in this thesis: photo-oxidation and thiol-ene photo-clicking.

The hydrophilicity is firstly induced by surface photochemistry via UV photo-oxidation of nanoporous 1,2-PB. Detailed quantitative and qualitative analysis of photo-oxidation in the presence of air is carried out by gravimetry, titrimetry and spectrometry. Distribution study of the hydrophilic photo-products relative to the polymer-air interface shows high concentration at the nanoporous interface. Thus, the majority of cross-linked PB matrix remains unmodified. Distribution of the hydrophilic groups along the depth is carried out by energy dispersive x-ray spectroscopy. It shows a highly heterogeneous photo-oxidation reaction with most of the oxygen fixed close to the surface facing the UV source. Optical characterization of UV photo-oxidation based devices is performed to report various losses occurring during light guiding experiments.

Thiol-ene click reactions are also used for the hydrophilization of the internal surface area of nanoporous polymer. This is done by photochemical reaction of the vinyl unsaturations of 1,2-PB at the interface (*ene functionality)* with hydrophilic thiols in the presence of a photoinitiator. The reaction is monitored by UV-Vis, FT-IR and contact angle measurements. Quantum yields of the photochemical reactions are estimated. Kinetic aspects of the photo grafting reaction on the nanoporous wall are studied using gravimetry. The fabrication of solid-liquid core waveguides is done by adapting the know-how on thiol-ene photochemistry to standard microfabrication

cleanroom setup and UV lithography. Contrast curves for thiol-ene systems are reported to comment on the homogeneity of the polymer modification by the reaction. Finally optical characterization of devices is carried out to report propagation loss values.

The UV photo-oxidation of nanoporous 1,2-PB is found to be a simple but heterogeneous surface modification technique compared to thiol-ene photo-modofication. Reaction times for photo-oxidation are longer by factors of 50-300 than thiol-ene reaction times. Compared to the oxidation, the thiol-ene reaction imparts better control, homogeneity and results in about half propagation loss in the fabricated waveguides.

The fabricated waveguides are also tested in few preliminary biosensing experiments. Antibody fragments, Fab that quench fluorescence from the fluorescein dye are introduced into the nanopores. The distribution of Fab fragments in the hydrophilic core is mapped by confocal microscopy. The study of their ability to quench the fluorescence from the dye is work under progress.

Dansk Resume

Blokcopolymerers evne til at selvorganisere kan udnyttes i forbindelse med fabrikationen af nanostrukturerede materialer. Det er netop hvad vi har gjort i det arbejde som præsenteres her: nanoporøse materialer (NP) med porediameter af ca. 10 nm er skabt udefra en 1,2-polybutadien-*b*-polydimethylsiloxan (1,2-PB-*b*-PDMS) blokcopolymer. Nanoporøsiteten er induceret ved først at krydsbinde 1,2-PB blokken og derefter kemisk fjerne PDMS blokken fra PB-*b*-PDMS copolymeren, som fra polymersyntesestadiet er designet til at have gyroid struktur. Vi udnytter nanoporøsiteten i polymeren samt dens kemiske komposition til at fremstille en ny type bølgeledere med en blandet fast-flydende kerne, som potentielt kan bruges i en række optofluidiske applikationer. Det opnås ved at fremskaffe hydrofile mønstre på de oprindelige hydrofobe NP vha. to typer fotokemiske modifikationer. Brydningsindeks kontrast genereres ved at vand spontant fylder de veldefinerede hydrofile områder af polymeren mens den omkringliggende hydrofobe NP forbliver tør og dermed har en lavere effektiv brydningsindeks. Således vil lys under total refleksion propagere indenfor de hydrofile mønstre. Bølgelederen med blandet kerne viser potentielt samme høj følsomhed overfor små prøvevolumener som de mere traditionelle flydende kerne bølgeledere; dog, den vigtige nye funktion af *in situ* prøvefiltrering gør den nye type bølgeleder særlig velegnet til at analysere komplekse væsker som blod og mælk.

Den første mode at inducere hydrofilicitet på i den iboende hydrofobe nanoporøse polymer er *via* UV foto-oxidering af 1,2-PB, hvor ilt fra luften fotokemisk fikseres på porernes grænseflade i form af hydrofile grupper som hydroxyl og carboxylsyregrupper. En detaljeret kvantitativ og kvalitativ karakterisering af foto-oxidations reaktionsprodukter udføres ved at kombinere gravimetriske målinger, titrering og spektrometriske analyser, såsom infrarød spektroskopi og fast stof ^{13}C kerne magnetisk resonans. De fleste af foto produkterne viser sig at være placeret på en subnanometer tynd lag ved den meget udstrakte polymer-luft grænseflade. Fordelingen af iltholdige kemiske grupper langs prøvens dybde kortlægges vha. energi dispersive x-ray spektroskopi. Analysen viser en meget heterogen fordeling af foto-oxidations produkterne med 4-5 gange højere ilt koncentration på prøvens overflade vendt mod UV kilden end i områder som ligger dybere end 100 μm ind i prøven. Optisk karakterisering af bølgeledere fremstillet ved UV foto-oxidation er udført for at måle forskellige tab der opstår under lys propagering i bølgelederne.

For den anden type hydrofile modificering af den stor nanoporøse polymers overflade udnytter vi de meget effektive *thiol-ene* fotokemiske 'klik' reaktioner. Dette gøres ved at lade grænsefladens

vinyl dobbeltbindingerne i 1,2-PB (*ene* funktionalitet) fotokemisk reagere med udvalgte hydrofile *thiol* forbindelser i forvejen bragt ind i porerne. Reaktionen er overvåget vha. spektroskopi (UV-Vis, FT-IR) samt gravimetriske og kontakt vinkel målinger. Kvanteudbyttet af de anvendte fotokemiske reaktioner er også estimeret. Thiol-ene reaktionstiden er en faktor 50-300 kortere end foto-oxidations reaktionstiden. Thiol-ene reaktionen tillader en høj grad af kontrol overfor typen og mængden af de introducerede hydrofile grupper, meget homogen fordeling af grupperne i hele pore grænsefladen samt en intakt materiale mekaniske styrke. Know-how af thiol-ene reaktionens kemiske aspekter bliver anvendt til at fabrikere fast-flydende kerne bølgeledere. Fabrikationen sker ved hjælp af standard mikrofabrikations renrums teknikker og UV-litografi. Bølgelederne fabrikeret vha. thiol-ene modifikation viser betydelige mindre optiske tab end tilsvarende bølgeledere lavet vha. UV foto-oxidering.

Immobilisering af et antistof binding fragment (FAB) inde i porerne af thiol-ene modificeret nanoporøse grænseflade er demonstreret. Dette er et første skridt i at undersøge brugen af vores bølgeledere indenfor biosensor applikationer.

Preface

In modern day science multi-disciplinary work, carried out at the interface between classical scientific streams is highly promoted by the nanotechnology. The current work is also a result of such multidisciplinary approach, combining synthetic chemistry, polymer processing, microfabrication and optofluidics. It uses nanoporous polymers as starting materials to fabricate a new class of liquid-core waveguide systems. Nanoporous polymers are very interesting materials due to the very high internal surface area. This finds diverse applications for nanoporous polymers in the fields of chemical engineering, biology, micro and nanotechnology, etc. On the other hand, liquid-core waveguides are used for light guiding in lab-on-a-chip systems. These are typically used for an on chip analysis of a liquid. The understanding of these two scientific fields is combined in the present case to materialize a solid-liquid-core waveguide system, SLCW. SLCW integrates *in-situ filtration*, in addition to the original functions incorporated in traditional liquid core waveguides, i.e., *liquid transport* and *waveguiding*.

The purpose of the current work is to process precursor block copolymer for the fabrication of SLCW systems. It identifies different steps needed to fabricate functioning solid-liquid core devices. One of the important steps in the present work is surface functionalization of nanoporous polymer, to tune its affinity towards aqueous solutions. Much of the work focus is put on finding out different routes for effective hydrophilization of an intrinsically hydrophobic polymer. Two different methods, namely photo-oxidation and thiol-ene click chemistry are employed for the surface functionalization of the nanoporous polymer. Photo-oxidation of polymers has been extensively studied in the literature, mainly from the degradation point of view. The current work utilizes the knowledge of the nature of photo-products and utilizes it in a constructive manner for rendering hydrophilicity in the polymer. The evolved idea for surface modification is studied with the aim of carrying out fundamental studies related to the process and its implementation for the device fabrication. The current work makes important scientific contribution regarding certain aspects of polymer photo-oxidation, which has not been studied so far. The published results on photo-oxidation of nanoporous polymers are found in Appendix A. The published optical characterization of the solid-liquid core waveguides based on the photo-oxidation is found in Appendix B. However, efficiency and control of the photo-oxidation reaction was found to be a bottleneck for improved liquid-core waveguide systems. This inspired us to look for a different approach of surface functionalization namely- thiol-ene click chemistry. Click chemistry is a relatively newer trend in polymer science finding interesting applications due to its efficiency, quantitative nature, no strict reaction conditions and better control. We used these interesting

features of the thiol-ene reaction to obtain much efficient liquid-core waveguide devices. Like photo-oxidation, some fundamental study of thiol-ene based hydrophilization in nanoporous polymer is carried out to gain valuable insight of the reaction mechanism and kinetics. The published results are found in Appendix C. The surface functionalization step is followed by an important step of UV lithography for the fabrication of the solid-liquid-core waveguide devices. Different fabrication protocols are identified, essential for fabricating a functioning liquid-core waveguide based on the nanoporous polymer. The published results based on fabrication are found in Appendix D. Finally, the devices are used for biosensing applications. The functionalized nanoporous area of the polymer is used for carrying out some Fab-antigen binding inside the waveguide for detection purposes. These preliminary results are found in Annex I.

The current PhD thesis is divided into 7 chapters. These chapters are meant to create an overview of the theoretical background and scientific findings of the PhD work. The aim is to create an overall understanding of the present work, without detailed description of the results in the chapters. The detailed discussion of the results is found in the scientific communications, which are attached as appendices. The list of the appendices is as follows:

Appendix A: Kaushal S. Sagar , Mads B. Christiansen, Sokol Ndoni, Type and Distribution of Chemical Groups from Controlled Photo-Oxidation of Gyroid Nanoporous 1,2-Polybutadiene, *Polymer Degradation and stability* **2011**, *96,* 1866-1873

Appendix B: Nimi Gopalakrishnan, Kaushal. S. Sagar, Mads Brøkner Christiansen, Martin E. Vigild, Sokol Ndoni, and Anders Kristensen, UV patterned nanoporous solid-liquid-core waveguides, *Optics Express* **2010**, *18,* 12903-12908

Appendix C: Anton Berthold, Kaushal Sagar, Sokol Ndoni, Patterned Hydrophilization of Nanoporous1,2-PB by Thiol-ene Photochemistry, *Macromolecular Rapidcommunications* **2011**, *32,* 1259-1263

Appendix D: Kaushal Sagar, Nimi Gopalakrishnan, Mads Brøkner Christiansen, Anders Kristensen and Sokol Ndoni, Photolithographic fabrication of solid-liquid-core waveguides by thiol-ene chemistry, *Journal of Micromechanics and Microengineering* **2011**, *21,* doi:10.1088/0960-1317/21/9/095001

Thesis outline

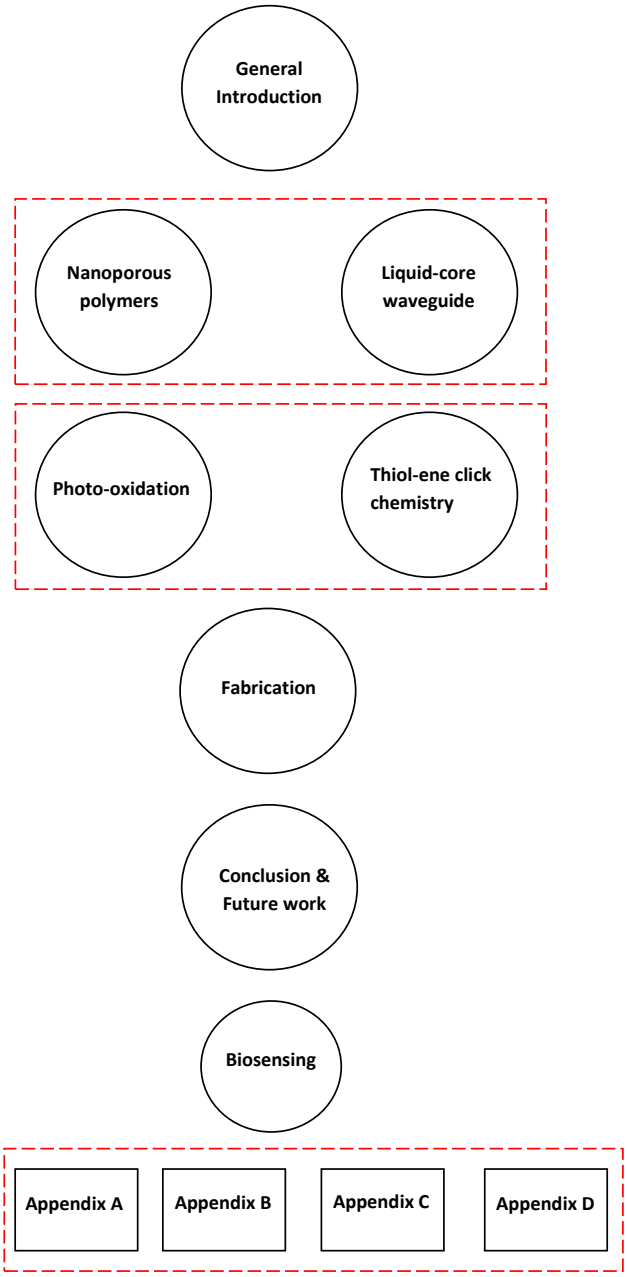

Chapter 1

Chapter 2 &3:
Theoretical background

Chapter 4& 5:
Surface modification

Chapter 6
Patterning of liquid-core waveguide devices

Chapter 7

Annex I: Application of liquid-core waveguide

Published journal articles

Contents

List of Abbreviations

ATR	Attenuated total reflectance
COOH	Carboxylic acid
EDX	Energy dispersive x-ray
FAB	Fragment-antigen binding
FT-IR	Fourier transform infrared
IgG	Immunoglobulin G
LCW	Liquid-core waveguide
MESNA	Sodium 2-mercaptoethanesulfonate
MSA	Mercaptosuccinic acid
NaOH	Sodium hydroxide
NIR	Near infrared
NMR	Nuclear magnetic resonance
NP	Nanoporous
PB	Polybutadiene
PDMS	Polydimethyl siloxane
PI	Photoinitiator
QY	Quantum yield
RI	Refractive index
SAXS	Small angle x-ray scattering
SEM	Scanning electron microscopy
SLCW	Solid-liquid-core waveguide
TBAF	Tetrabutylammonium fluoride
THF	Tetrahydrofuran
UV	Ultraviolet
μ- TAS	Micro total analysis

List of figures

1. General introduction

The present work is about fabrication of a new class of liquid-core waveguides. Liquid-core waveguides (LCW) guide light similar to a solid optical waveguide, but differs in its structure. It has a core constituted of liquid instead of a solid material, which is surrounded by a solid or liquid clad. The liquid filled core volume acts as a tunnel which guides an optical wave propagating in the waveguide. Figure 1.1 shows a schematic representation of a LCW.

The current PhD work is part of the multidisciplinary **LicorT** (**Li**quid-**cor**e Waveguide **T**echnology for Diagnostics Applications) project, involving different scientific streams like polymer chemistry, surface functionalization, microfabrication and optofluidics. Within the LicorT project, current work focus is mainly on fabricating liquid-core waveguide devices from the nanoporous polymers. Premise of the current work is illustrated in figure 1.2, showing its overlap with different scientific streams. The major contribution comes from the field of polymer chemistry, surface modification and microfabrication, with a smaller contribution from optofluidics. At this stage, we intend to introduce different scientific streams involved in materializing the current waveguide system. This way we can built the necessary foundation needed for further discussion about the proposed waveguide system. We start with the field of microfabrication and optofluidics. This is followed by introduction of nanoporous polymers used in fabrication and lastly different nanoporous surface modification techniques adopted for the current system.

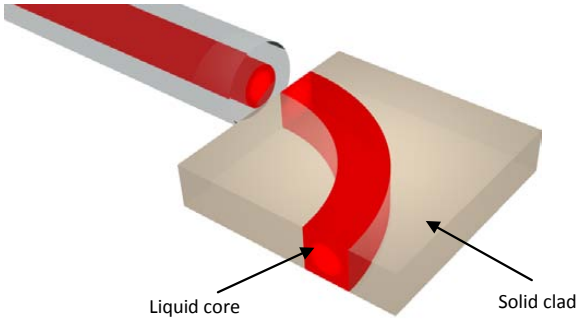

Figure 1.1. Schematic representation of a liquid-core waveguide system. The liquid core is embedded in a solid clad which works as a tunnel for guiding light.

The field of micro total analysis systems (μ- TAS) or Lab-on-a-chip systems has experienced a rapid growth in past three decades. This is due to its applicability in diverse fields like physics, analytical chemistry, chemical synthesis, biotechnology etc. One of the many applications of a

miniaturized lab-on-a-chip system is that it facilitates the concept of point-of-care system. It also offers several advantages such as low sample requirement, low cost, reduced analysis time etc[1]. The present focus in this field is on miniaturization of microfluidics parts to be able to accommodate analytical system on small size devices. Integrated optical circuit is one of the most important components of these microfluidic devices for data transferring to decoding units[2]. There has been a continuing progress in the field of optical waveguides. Today, optical waveguides are

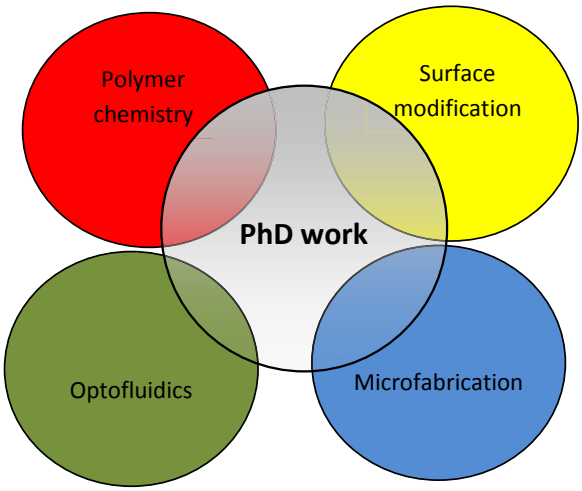

Figure 1.2. Diagram illustrating premise of the current PhD work between different scientific fields.

capable of transferring terabytes of information every second between different kinds of communication devices. The optical based detection systems that involve optical waveguide structures are popular in lab-on-a-chip analytical systems due to its sensitivity and small sample volume requirement. Thus, it can improve the detection limit of an on chip analysis. In such systems, the substance of interest is confined to a microchannel where illumination and detection is carried out with maximum possible collection efficiency. However, the problem with this approach is difficulty in fabricating these complicated designs on chips. Much simpler design would be to fabricate a Liquid-core waveguide (LCW) system. LCW systems function on the principle of total internal reflection, similar to an optical fiber. In LCWs, a high refractive index liquid core is surrounded by a low refractive index clad[1-5]. The application of LCW to lab-on-a-chip based systems would allow an on-chip channel to be utilized as an optical waveguide which increases path length of the on-chip detection system (more detailed are discussed in chapter 3).

After discussing liquid-core waveguides, let us introduce another scientific stream involved in the fabrication of the waveguides; polymer chemistry in the form of nanoporous polymers. The nanoporous polymers has porosity on a typical structural length scale of 10-100 nm and internal surface area of 50-500 m^2/g [6]. The nanoporous described in the current work are derived from self assembled block copolymers. These block copolymers are capable of forming highly ordered structures by 'bottom up' approach. The structural periodicity and orderliness on the nanometer scale is fetching interesting applications for nanoporous polymers. It can be used as a template for fabricating nanoscale structures. Its ability to get oriented in desired direction can be used as an ultra (nano) filtration membrane for numerous chemical and biochemical applications[7]. Nanoporous polymers can be an attractive option for applications in low dielectric constant materials[8, 9]. It also serves as catalysis substrates and in the field of controlled drug release[10].

After introduction of the nanoporous polymers, next step is surface functionalization of the vast nanoporous interface. In the current work, this step forms a linkage between polymer science and microfabrication field for the fabrication of liquid-core waveguides. The surface functionalization techniques adopted in the current work are UV photo-oxidation and thiol-ene click chemistry. It is appropriate to have an overview of these techniques at this stage before engaging into an in-depth discussion of relevant results in subsequent chapters on the thesis. Photo-oxidation of polybutadienes is a well studied system in literature from the degradation and stability point of view[11]. The studies mainly involve qualitative analysis of the photoproducts formed after degradation reaction. We apply this knowledge of photo-oxidation in a constructive way to obtain hydrophilic chemical groups rendered at the nanoporous interface. If these hydrophilic groups are present in high concentration, it can tune hydrophilicity of the polymer volume (details in chapter 4). Another approach for surface functionalization adopted in the current work is thiol-ene click reactions. Thiol-ene click chemistry is known for its efficiency, quantitative nature and high selectivity and not stringent reaction conditions[12]. A thiol molecule is highly selective towards vinyl unsaturation which results in clicking of thiol on to the vinyl groups. In our case, we use the commercial hydrophilic thiol molecule and graft it onto the pendant double bond at the polymer-air interface. The higher surface density of the clicked hydrophilic thiol groups can tune the hydrophilicity of the nanoporous polymer.

Thus, we have briefly introduced liquid-core waveguide systems, nanoporous polymers and the different surface functionalization routes up till now. The next step is to combine the understanding of these scientific streams for the production of our liquid-core waveguide system. Let us begin by understanding the nature of the problems associated with the liquid-core waveguide fabrication and later propose our approach for addressing these issues.

1.1 Defining the problem

Although the field of liquid-core waveguides looks rather interesting, it is important to understand the problems which act as *bottleneck* in commercial implementation of liquid-core waveguide systems. There are two major disadvantages with respect to the use of liquids in integrated optical sensing. Firstly, liquids are not stable in their physical shape; they have to be confined in a certain volume. Secondly, due to their relatively low density, their refractive indices are usually lower compared to solids[13].

1.2. Strategy of the work

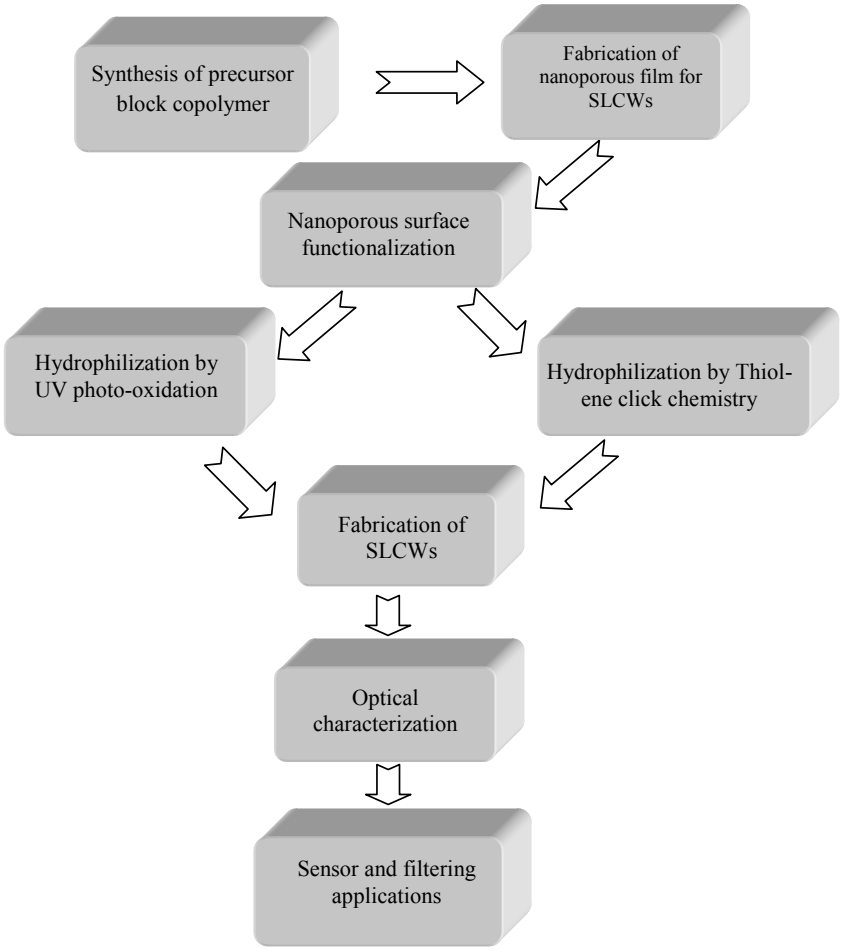

Figure 1.3. Flow diagram illustrating different steps required for reaching final goal of the work.

The second limitation emerges out to be a major area of concern. This is because the high refractive indices of most common lab-on-a-chip substrates like silica-based glasses (~ 1.46), PMMA (1.48), polycarbonate (1.58), polystyrene (1.59), and silicon (~ 3.50). Therefore, it is essential to find the liquid of refractive index higher than clad material to meet the condition of total internal reflection. Most of the important solvents such as water, methanol, ethanol, acetone, THF etc. have refractive indices well below those of silica based glasses[14].

Secondly, in liquid based opaque systems, the collection efficiency of the output signal is poor due to light scattering. Loss of signal efficiency can also occur from high coupling, surface or volume scattering losses (detailed discussion in section 3.3). This ultimately results in lower signal to noise ratio in the output which ultimately decreases the sensitivity of the system[15].

The use of nanoporous polymer addresses both the above mentioned issues. The nanoporous nature of the polymer considerably reduces the effective refractive index of the material making it suitable for liquid-core waveguides (details in chapter 3.4). Secondly the nanoporous nature works as an inbuilt filter for the turbid analyte solutions, separating liquid from the larger particles. The nanopores will selectively allow infiltration of the liquid, which eliminate the possibility of scattering of the propagating signal.

The present approach of fabricating liquid-core waveguides can be depicted in the flow diagram shown in figure 1.3 with different intermediate steps. It begins with synthesis of an asymmetric polybutadiene-*b*-polydimethylsiloxane block copolymer. The block copolymer synthesis is done using anionic polymerization technique. The synthesized polymer is in a paste form and required to undergo different steps to fabricate final nanoporous polymer film required for LCWs (details in chapter 2). It involves solvent casting of block copolymer with thermal cross-linker in a solvent. The solvent casted film undergoes thermal cross-linking step which produce a glassy block copolymer film. Finally the block copolymer film undergoes a chemical etching step for quantitative removal of polydimethylsiloxane block to obtain the nanoporous polymer. The nanoporous polymer is intrinsically hydrophobic in nature. For the LCWs application, it is essential to induce hydrophilicity in the nanoporous polymer (details in chapter 3). The hydrophilization of nanoporous polybutadiene is achieved by using two different approaches: photo-oxidation of 1,2-PB (details in chapter 4) and thiol-ene click reaction (details in chapter 5). The surface functionalization step is followed by fabrication of the LCWs. It involves usage of UV photolithography to produce desired hydrophilic regions or microchannels in the nanoporous polymer device (details in chapter 6). Finally the devices are characterized for its optical performance i.e. estimation of propagation losses in the system. The LCW devices can also be

used for bimolecular sensing (Annex I). This is a unique feature of a nanoporous polymer based LCW which can perform as biosensor.

2. Nanoporous polymers

2.1 Introduction

As stated in the introduction chapter, current work is based on nanoporous polymers. These nanoporous polymers are derived from a block copolymer precursor. The periodic nanoporous structures are created by capitalizing on self organizing ability of the block copolymers. The self organization can be well understood by first looking at thermodynamics of the polymer mixtures, and extending this knowledge to the block copolymer systems. The thermodynamic stability of a polymer mixture is governed by the change in Gibbs free energy of the mixture. If the Gibbs free energy is lower for the mixture than for the separate polymers, the homogeneous mixing of polymers into a one phase system can take place. This change in Gibbs free energy is the sum of entropic and enthalpic contributions and can be expressed as:

$$\Delta G_m = -T\Delta S_m + \Delta H_m \quad (1)$$

Where, ΔG_m is the Gibbs free energy of mixing, ΔS_m is the entropy of mixing, T is temperature and ΔH_m is the enthalpy of mixing. The entropic term is generally positive due to an increase in the degree of disorder produced by mixing as compared to the separate components. Therefore, due to the minus sign this term lowers the free energy of mixing. The major component of the entropy term is the so-called translational entropy, which relates to the position of molecules' centers of mass. In the case of small molecules the translational entropy of mixing is significant and compensates for a wide range of differences in chemical composition that show unfavorable enthalpy of mixing ($\Delta H_m > 0$, endothermal)[16, 17]. As a result many fluids composed of small molecules are miscible. However, the translational entropy contribution is significantly reduced in the case of polymer mixtures. This is due to the drastically reduced number of polymer molecules in a given volume as a result of the chemical linkage of a great number of repeating units or monomers forming a single polymer molecule, also called a macromolecule. Thus, blending of polymers is not greatly dependant on the translational entropy change of the system and even small positive values of the enthalpy of mixing between two polymers can result into positive Gibbs free energy of mixing, equivalent to a thermodynamically favored phase separation. The enthalpic contribution ΔH_m for polymers interacting by only Van der Waals forces is positive due to the stronger attractive energies between identical monomer units than between different monomer units[16]. Such a behavior of monomers opposes mixing. Most synthetic polymers, including the polymers we have worked with, are of this type. Therefore for these materials the general trend is that different polymers do not mix, and the thermodynamic immiscibility is

enhanced with increasing molar mass of the polymers. For a minority of synthetic polymers or for natural macromolecules showing electrostatic, massive dipole-dipole or hydrogen bonding interactions between two different polymers the enthalpy of mixing can be negative (exothermal mixing) and miscibility favored.

An expression for the enthalpy of mixing of two polymers 1 and 2 can be derived by the Flory-Huggins theory:

$$\Delta H_m = RT\chi_{12}n_c\phi_1\phi_2 \tag{2}$$

Where, R is the ideal gas constant, n_c can be taken as the total number of moles of monomers 1 and 2; ϕ_1, ϕ_2 are the volume fractions of each polymer, and χ_{12} is the Flory-Huggins interaction parameter. This parameter is empirical and dimensionless; it was originally introduced to characterize the enthalpy of mixing per monomer unit. A positive χ_{12} would characterize endothermal mixing, or, from the discussion above this should hint immiscibility between the two polymers. A negative or zero χ_{12} would signal miscibility between the two polymers. Within the Flory-Huggins theory the total moles of monomers n_c can be expressed as:

$$n_c = n_1N_1 + n_2N_2 \tag{3}$$

Where, n_i is the number of moles of polymer i and N_i its degree of polymerization ($i = 1, 2$). The polymers are idealized here as monodisperse macromolecules. In the case of a symmetrical binary blend ($N_1 = N_2 = N$), the theory predicts a critical value for the product $(\chi_{12}N)_{crit} = 2$. For values $(\chi_{12}N) > (\chi_{12}N)_{crit}$ phase separation is predicted, while for $(\chi_{12}N) < (\chi_{12}N)_{crit}$ the two polymers are expected to be miscible, forming one homogeneous phase.

In the form shown above the Flory-Huggins interaction parameter is expected to be inversely proportional to the absolute temperature T:

$$\chi_{12} \sim \Delta H_m / T \tag{4}$$

However, the experimental form of the parameter has been found to contain an additional temperature-independent term, which signals an entropic contribution to the interaction parameter:

$$\chi = (a/T) + b \equiv \chi_H + \chi_S \tag{5}$$

The experimentally correct interaction parameter is shown by χ and a, b are constants. The entropic contribution in this case must be different from the translational entropy mentioned above.

In the case of polymer blends it accounts for volume changes in the mixture relative to the sum of the separate volumes of the components, changes in the local mobility of monomer units at the contact zones between monomer *1* and *2*, etc.

The above discussion regarding polymer blends can be applied to understand a copolymer system, where each polymer chain contains at least two chemically different monomers. The copolymers can be random, alternating, graft or of block type. In random copolymer arrangement, different monomer units are randomly repeated in the polymer main chain. Alternating copolymer has an alternating arrangement of the different monomer units in the polymer chain. In a graft copolymer, one component forms the main chain of the polymer whereas, the second component is in the form of a chain, which is grafted covalently to the main chain. Block copolymers are chemically distinct repeat unit blocks or sequences covalently liked to form a copolymer chain. The current work uses a block copolymer system for obtaining nanoporous polymer, hence other copolymer systems are not considered for further discussion.

Many of the block copolymer systems studied in the past 20-30 years have been prepared by living anionic polymerization, which allows a high degree of control in degree of polymerization and composition. Different molecular architectures are possible to achieve di-block (2 step process), tri-block (3 step process) or star block copolymers from chemically different building blocks using polymer synthesis[18-20]. We concentrate the following discussion on diblock copolymers. In the discussion about polymer blends, we saw that the polymer mixtures tend to separate into two phases which is macroscopic in nature. In the case of block copolymers, the chemical linkage between two blocks inhibits such macroscopic phase separation, and the two blocks segregate, or self-assemble at mesoscopic length scales typical for the coils of the constituting blocks (5-100 nm). At length scales much bigger than these a block copolymer system appears homogeneous.

2.2 Block copolymer microphase diagram

The usual presentation of phase diagrams for binary polymer blends at atmospheric pressure is a plot of temperature as a function of blend composition, given for example by the volume fraction of polymer 1, ϕ_1. Boundary lines between two-phase and 1-phase regions are shown in such diagrams. Alternatively, for symmetric binary blends $N\chi$ is plotted as a function of blend composition. A phase diagram for a binary polymer blend is constructed by systematically changing the composition of the blend. For each composition a temperature scan is run monitoring the blend typically by scattering techniques (e.g. light scattering or x-ray scattering). The transition from one to two phase system is marked by a significant increase in the scattering intensity. At long enough times macroscopic phases may be formed. Whereas, a diblock copolymer is ideally

one component system with only one type of molecule; therefore a phase diagram for a block copolymer does not make sense. The self assembling phenomena of block copolymers are represented by a so-called microphase diagram. This microphase diagram is constructed by changing the composition of different blocks in a copolymer. Thus, each data point marked on the microphase diagram corresponds to a distinct block copolymer system, which is studied at different temperatures.

Most presentations of the self-assembling of block copolymers are direct generalizations of the Flory-Huggins theory of polymer blends. In the case of diblock copolymers the microphase diagram is a plot of $N\chi$ as a function of block copolymer composition. N is the total degree of polymerization of the block copolymer. The reason for this preferred representation can be found by adapting the expression (3) above to the case of block copolymers. The number of moles n_1 and n_2 are always equal in the case of a diblock copolymer: $n_1 = n_2 \equiv n$ due to the fact that each molecule contains one of each block. Therefore eq. (3) can be written as follows:

$$n_c = n\,(N_1 + N_2) = n\,N \tag{6}$$

The expression above shows that the product χN is quite naturally describing the interaction between blocks in a block copolymer. The interface between the two segregated phases is dependent on its value. There are three different regimes of microphase separation based on χN. A regime at $\chi N \approx 10$ is called weak segregation regime (WSL), $\chi N \approx 20$ is an intermediate segregation regime, (ISL) and $\chi N >> 10$ is a strong segregation regime (SSL)[18, 21, 22]. The higher Nχ would result in sharper micro domain boundaries facilitated by chain stretching and reduced contact between two components (narrow interfaces). Similarly, the lower Nχ value would result in a mixed interface of the polymer blocks and at sufficiently lower values; a homogeneous disordered system is formed[22-24].

The microphase diagram of block copolymer shows transition from the disordered (homogeneous) to an ordered microphase and also the transitions between two ordered phases. TEM and small-angle scattering techniques are widely used analytical techniques to analyze the microphase diagrams of block copolymers. It is important to realize difference between a phase diagram for polymer blends and a block copolymer microphase diagram. The phase diagram can be generated by varying the volume contribution of different polymers in the same mixture. Whereas in case of microphase diagram, each measurement is done with a different block copolymer having different chain length.

Similar to the polymer blends, the deciding factor for block copolymer architecture is the product χN. Variation in the composition of the diblock copolymer expressed as ϕ_1, will result in unequal stretching and packing of polymeric blocks resulting in different morphologies as shown in figure 2.1. The diagram shows sequence of different thermodynamically stable phases in a real system. When the product χN is below a critical value, the block copolymer is in a disordered state. Above the critical value, block copolymer microphase separation takes place into periodically ordered structures, where the sequence of different morphologies depends upon the composition of the copolymer[22].

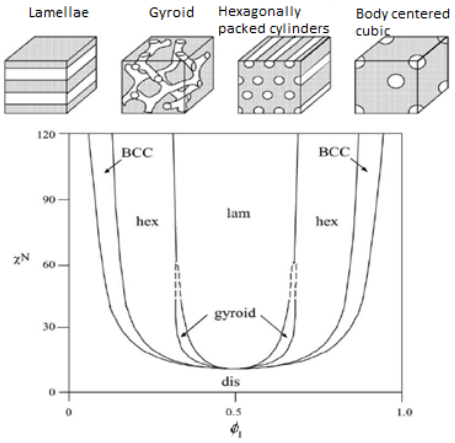

Figure 2.1. Phase diagram of a PS-*b*-PI diblock copolymer showing equilibrium morphologies. In the phase diagram, stable phases of lamellae (lam), gyroid, hexagonally packed cylinders (hex) and body centered cubic (BCC) are indicated[22].

polystyrene-*b*-polyisoprene (PS-*b*-PI) system is taken as an example to demonstrate various microphase segregated morphologies in the ordered state[23]. At ϕ_1 = 0.17 (volume fraction of polystyrene in this case) result in microspheres ordered on body centered cubic lattice of PI. At 0.17< ϕ_1 < 0.28 the morphology is changed to hexagonally packed cylinders. Between 0.28 <ϕ_1< 0.34, an ordered bi-continuous gyroid phase segregation is created in the PI matrix. From 0.34 < ϕ_1 < 0.62 a lamellar phase microstructure is created. Beyond this volume fraction, an inverse of the above mentioned morphologies are reported[41-43]. Another class of a metastable microphase in diblock copolymers is the hexagonally perforated layer structures (HPL). Such intermediate structures are observed on heating between the lamellar and hexagonal-packed cylindrical phase. It is considered to be long-lived non-equilibrium structure involved in the formation of a gyroid phase[25, 26]. In the present work, we use the gyroid morphology for fabrication of the solid-liquid

core waveguide applications. Therefore in the next section, gyroid morphology is conferred in details, without considering other morphologies for further discussion.

2.3 Gyroid morphology

Gyroid is the name of a minimal surface with $Ia\bar{3}d$ symmetry. Gyroid morphology divides the polymer matrix into two interpenetrating equally sized channels as shown in figure 2.2[27]. A gyroid structure model, based on rod-type connectors depicts the two volumes (represented in two different colors). This morphology was first misinterpreted as ordered bicontinuous double diamond (OBDD) in the initial phase of its realization[27-29]. The minority block in this case forms channels embedded in a matrix phase. This matrix phase is formed by the majority component where channels are subdivided into two distinct interpenetrating networks. Both the components (majority and minority) in a gyroid system are threefold continuous lattice with periodicity. The channels are joined as triads and these two continuous networks are mirror image of each other.

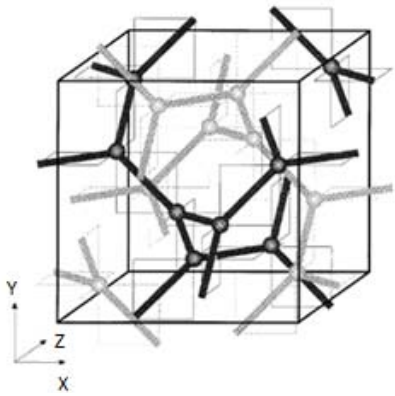

Figure 2.2. Real space geometrical representation of the gyroid phase. Different colored interpenetrating networks constitute bi-continuous minority phase embedded into a majority block polymer matrix[27].

As already discussed, the gyroid morphology is formed from slightly asymmetric block copolymer ($0.3<\phi_1<0.5$) system. Due to higher volume fraction of the minority block compared to other equilibrium phase morphologies i.e. HEX, BCC, it can produce highly porous systems, if the minority block is removed quantitatively from the system. The lamellar morphology can also yield such highly porous systems but retention of the porosity can be challenging. On the other hand, gyroid structure can retain the high degree of volume porosity in polymer matrix and this porosity can be continuous in nature, with open pores available at the surface. Optical transparency is also expected in a gyroid nanoporous polymer due to its isotropic threefold continuous lattices. Due to all the above mentioned advantages, we chose gyroid morphology for our application.

2.4 Concept of nanoporosity

The current work uses polybutadiene-*b*-polydimethylsiloxane (***PB-b-PDMS)*** asymmetric block copolymer system for making nanoporous polymers. The PDMS block is used as a minority component with $\phi_1 \approx 0.4$. This block copolymer system generates gyroid phase transition at elevated temperature which is preserved into the PB matrix by cross-linking reaction. Later, the PDMS block is quantitatively removed by chemical etching to produce gyroid shaped nanoporosity in the PB matrix.

2.4.1 Anionic block copolymer precursor

The PB-b-PDMS block copolymer is synthesized by living anionic polymerization technique. Sec-butyllithium is used as an initiator for the anionic synthesis. The polymerization of 1,3-butadiene is carried out under argon at -20^o C for 3 h in THF. Next step is the addition of hexamethylcyclotrisiloxane monomer to the living polybutadienyllithium end. The reaction temperature at this stage is raised to 0^o C. The polymerization of the later block is carried out for 3 days. After achieving the desired block copolymer molecular weight, reaction is terminated by adding 3 molar excess of trimethylchlorosilane. The polymer is precipitated in methanol and dried for molecular weight and polydispersity characterization.

2.4.2 Cross-linking of 1,2-PB

Cross-linking of polymers is widely known phenomena for reducing the chain mobility. It is done by linking polymer chains using covalent or ionic bonds. The cross-linking is either done using a multifunctional monomer unit during polymerization or in a second step after polymerization, to link linear or branched polymer chains[30]. In the present case, we opt the second approach of cross-linking. The reaction is carried out by free radical polymerization of 1,2-PB pendant unsaturation. The Cross-linking reaction imparts considerable stiffness to the polymer melt, above its glass transition temperature. If the degree of cross-linking is not very high for e.g. 1 cross-link per 100 monomers, the polymer possess elastomeric properties; thereby recovers the deformation after the stress release. Very high degree of cross-linking can result in enhanced brittleness of the polymer, since the segmental motion of the polymer chains is ceased. Thus the flexibility after cross-linking reaction is a function of degree of cross-linking, polymer structure and molecular weight[30, 31].

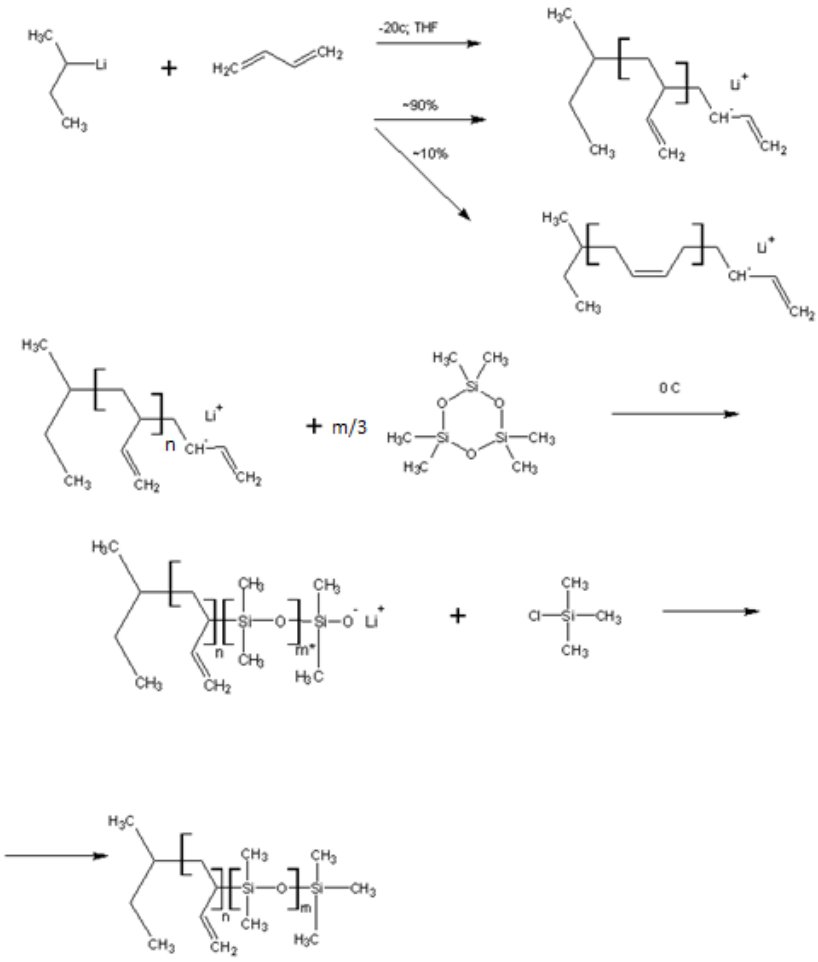

Scheme 2.1. Reaction scheme of anionic polymerization of *PB-b-PDMS* diblock copolymer

The need of cross-linking 1,2 PB matrix in our case is for the retention of nanoporosity after chemical etching of gyroid minority block (PDMS). The high internal surface created due to nanoporosity would like to minimize its area, thereby applying pressure on the nanopores. High degree of cross-linking (60-80% of the PB double bonds) of the matrix phase would counter this internal pressure for the retention of the nanoporosity. Secondly, the polymer melt after high degree of cross-linking is easy to handle due to its glassy behavior.

In the present block copolymer system, we observe gyroid morphology of the PDMS block close to 140^{o} C[32, 33]. Therefore, we capture the morphology by high degree of cross-linking of the PB phase at this temperature. The solvent casting of block copolymer and dicumyl peroxide which is used as a thermal cross-linker (1 mol % relative to the pendant unsaturation in 1,2-PB) in THF is

done on a glass or silicon substrate. Dicumyl peroxide (DCP) is chosen as a thermal cross-linker due to its high quantum yield close to the block copolymer gyroid transition temperature[34, 35]. After evaporation of THF, the polymer melt is cross-linked in an air tight steel cylinder; filled with inert gas to insure no trace of oxygen in the cylinder. The inert atmosphere (under nitrogen/argon) is chosen to prevent oxidative degradation of the copolymer during thermal cross-linking. Cross-linking reaction of the polymer is carried out for 2 h. The reaction converts 60-80% of the polybutadiene double bonds, which makes the polymer glassy and imparts needed mechanical stability and handlability[36].

2.4.3 Etching of PDMS

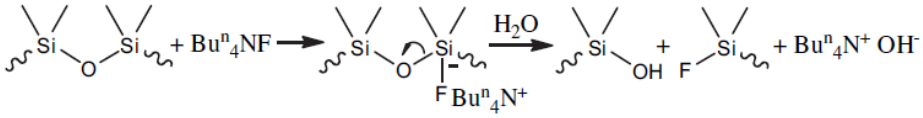

Scheme 2.2. Anticipated reaction scheme of degradation of PDMS block by TBAF[32].

In order to generate porosity in the highly cross-linked PB matrix, minority component (PDMS) is chemically degraded. The degradation of PDMS is carried out using tetrabutylammoniumfluoride (TBAF) in THF[37-39](scheme 2.2). In the case of TBAF in THF (and in the presence of water), the etching reagent behaves as a base undergoing S_N2 Si mechanism resulting in cleavage of silyl ethers to alcohols[32]. The reaction with TBAF is taking place in THF which can swell the cross-linked PB matrix, facilitating efficient degradation of the PDMS block. The chemical etching process is carried out between 5-36 h depending upon the film thickness. An etched film is subjected to washing in THF, which is gradually mixed with methanol in steps (each step of 20% methanol addition) until pure methanol stage is reached. Each step for washing lasts for 20-30 min and after last step (pure methanol) the nanoporous films are dried under vacuum or inert gas flow[32, 33].

2.4.4 Characterization of nanoporosity

Etched polymer films are characterized for nanoporosity using a variety of techniques. It is done using FT-IR spectroscopy where Si-O stretch and CH_3 stretch coming from PDMS group are disappeared after etching[32]. SAXS data also proves nanoporous nature of the etched sample by recording roughly two orders of magnitude higher scattering intensity compared to non-etched cross-linked sample[32]. This is due to the increased electron density contrast between PB matrix and the air filled nanopores compared to the contrast between PB and PDMS. Microscopic techniques such as AFM, SEM and TEM also indicate the nanoporous nature of the sample[32, 37]. An example of nanoporosity is depicted in figure 2.3. SEM image of a typical knitting pattern characteristic of

gyroid nanoporous polymer sample is shown figure 2.3a. The TEM image shown in figure 2.3b indicates the wagon wheel projections, also characteristic of gyroid morphology. The nitrogen adsorption is used for measuring internal surface area of the nanoporous sample. Very high surface area (283±14 m^2/g) recorded by adsorption of liquid nitrogen onto the polymer-air interface proves the nanoporous nature of the cross-linked polymer.

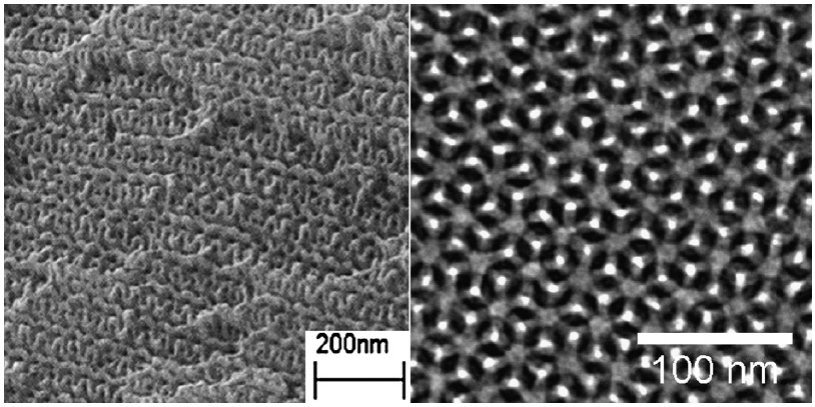

Figure 2.3. a) SEM image showing characteristic knitting pattern and b) TEM image indicating wagon wheel projection typical of the gyroid nanoporosity[32].

2.4.5 Mechanical stability of nanoporous polymer

The PB-*b*-PDMS block copolymer films tend to crack after thermal cross-linking step. The fragile nature of the nanoporous polymers can be a serious obstacle; restricting its applicability in different areas. Therefore, it is very important to understand the reasons for the brittle behavior of the polymer after cross-linking step. Cracking of the cross-linked polymer film can be due to the following:

1) Thermal cross-linking takes place at 140^{o} C where equilibrium chain conformation of the polymer is different than at room temperature. This induces shrinkage stresses in polymer network, resulting in cracking of the film
2) Very high degree of cross-linking (60-80% of the PB double bonds) ceases segmental motion of the polymeric chain, enhancing brittleness of polymer film. The degree of cross-linking can be adjusted such that, it can retain nanoporosity in the PB matrix and also impart flexibility to the polymer film. This type of work is not conducted in the present case but it is one of the proposed activities for the future.
3) The configuration of 1,2-PB is also responsible for the brittle behavior of the polymer. The pendant groups restrict close packing of the polymer chains resulting in lack of loss

mechanism in the system. This can be reduced by hydrogenation of PB[40-42] to impart greater elasticity. In the present work, we have not addressed this approach, but we recommend it in the future work for the improvement of the existing nanoporous polymer system.

3. Liquid-core waveguides

3.1. Introduction

As briefly described in the introduction chapter, an optical waveguide typically consists of a solid core of high refractive index (RI) surrounded by lower RI clad. If this solid core is replaced with a liquid core the system is called as a *liquid-core waveguide (LCW)* [43-45]. LCW system offers variety of advantages for an optical based detection system such as low sample volume requirement, high sensitivity, and possibility of fabrication on existent micro and nano technology platform[14, 46-49]. The first commercial application of the LCW was introduced in early 1970, when hexacholorobutadiene based system was a serious candidate for long distance telecommunications[50]. Later the drive for usage of LCW shifted towards chemical and biological sensing applications, where the content of the liquid core is of interest. Despite of the numerous advantages, LCW is yet an evolving system due to the fact that most biological and chemical sensing analytes are aqueous. The RI of water (1.33) is much smaller than most of the candidates suitable for making a waveguide clad (polymers, glass, metal etc). However, some clever approaches have made it possible to fabricate and implement this technology for various sensing applications. The following section of the chapter briefly describes different state-of-the art LCW technologies.

Total internal reflection (TIR) based waveguides

The literature reports different types of liquid-core waveguide systems such as TIR, non-TIR and interference based systems. Out of which only TIR based waveguides find relevance with the current work hence other type of waveguides are not considered for the discussion. The TIR based LCWs offer an important advantage of lossless propagation along the desired direction and not along the other principle directions[51]. The loss of signal in this case is only arising from the imperfections like surface scattering or absorption. Majority of TIR based LCWs are made with low refractive index polymer Teflon AF (RI= 1.26), as discussed in the introduction chapter[2, 4, 13, 47]. Nanoporous clad based LCWs is another class which uses low RI clad material by adding nanopores thereby, reducing the effective refractive index[52]. The limited choice of solid clad material can be resolved by using another type of LCW with a liquid clad around a liquid core. This type is known as liquid-liquid core or L^2 waveguides[53]. Recent developments in the field of LCW include slot waveguides which are capable of guiding light in nanoscale cross sections. This facilitates the LCW based sensing into nanometer regime with pico or subpicoliter sample volumes[54].

3.2 State-of-the art liquid-core technologies

Liquid-core waveguides fabricated in glass capillaries (uncoated glass) were first used in Raman spectroscopy by Schwab et al[55] and in absorption applications by Tsunoda et al[56] These devices guide light by means of total internal reflection at the glass–air interface, represented a significant development in water-based light guides. They were the first water-filled waveguides which demonstrated low loss values for borosilicate-glass tubes filled with water.

Liquid-core fibers consisting of glass capillaries with polymer coating internally and/or externally serve several practical advantages over bare glass structures such as no contamination on the exterior surface and improved flexibility and breakage resistance[14] Liquid-core fibers based on tubing lined with polymers have been reported by Gilby et al[57] and Dress et al[13] who investigated glass tubes coated internally with poly(tetrafluoroethylene), also called as Teflon AF 2400. Hong and Burgess also used internal coating of Teflon AF on porous polypropylene tubes for liquid core waveguide applications. However, neither of these groups actually performed the optical properties measurements of their liquid-core fibers. Dress et al[4] reported for the first time a detailed mathematical model of light propagation in their Waveguide. Later, liquid-core waveguide based on externally coated silica tubing was recently reported by Altkorn et al[14] who obtained lower propagation loss as compared to Dress et al results.

Another way to achieve liquid core waveguide is by choosing an appropriate high refractive index liquid. Carbon disulphide (CS_2) has a refractive index higher than that of glass (1.63) and was chosen early on for this purpose by Fujiwara et al[58]. The practical usefulness of CS_2 based liquid core waveguides is restricted due to its strong odor and toxic nature. Some aqueous solutions of high viscosity, e.g., concentrated solutions of sucrose (saturated aqueous solution of refractive index = 1.50) is used as a high index liquid core showed high transmission with low-refractive index polymeric capillaries. Tsunoda et al. demonstrated fluorinated ethylene-propylene copolymer (refractive index = 1.34) based arrangement in working with ethanol (Refractive index= 1.36). Hong et al showed that, by preparing high concentrations of ethylene glycol (refractive index=1.43) in aqueous liquids, the overall refractive index can be raised sufficiently to obtain good light transmission in polytetrafluoroethylene capilaries[59]. Nanoporous clad based liquid core waveguides are demonstrated by Korampally et al[60] where etched silicon cladding was used for biosensing applications.

Despite of all the diverse technologies, the current state-of-the art liquid core waveguide research mainly concentrate on the low refractive index Teflon AF 2400^{R} (refractive index = 1.29 at λ = 632.8 nm). It is a commercially available polymer manufactured by Dupont^{TM}. Numerous

applications of LCW based on Teflon AF are in spectroscopy, electrophoresis, and pollution measurements.

After discussing relevant state-of-the-art liquid-core systems, let us look into some of the relevant theoretical concepts of the waveguides. They are important to understand the functioning and optimization of the liquid-core waveguides which will be dealt in succeeding chapters.

3.3 Theory of waveguides

When a beam of light travels from one medium to another with a difference in the refractive index the light is refracted according to Snell's law[61, 62]:

$$n_1 \sin(\theta_1) = n_2 \sin(\theta_2)$$

where n_1 and n_2 are the refractive indices of the first and second material respectively, and θ_1 is the incident, and θ_2 is the refracted angle with respect to the normal. When moving from a higher to a lower RI material ($n_1 > n_2$), there is no solution for the equation when θ_1 exceeds a critical angle θ_c which is

$$\theta_c = \arcsin\frac{n_2}{n_1}$$

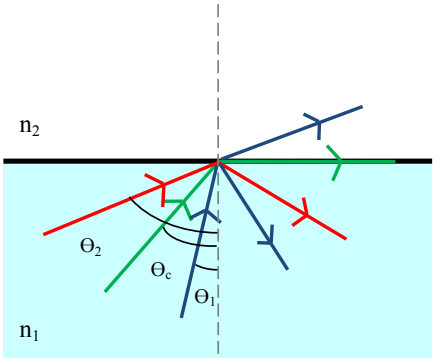

Figure 3.1. Schematic representation of principle of total internal reflection. Light passing through s higher RI medium surrounded by a lower RI medium tends to reflect back (red arrow) at an angle greater than critical angle. On the other hand, incident light at an angle lower than the critical angle (blue arrow) tend to refract out of the medium.

As illustrated in figure 3.1, the incident angle of the light $\theta_1 < \theta_c$ the beam is partly reflected, and partly refracted at the interface. Larger the incident angle, larger the part of light which gets reflected back into the system. For a beam entering at an angle $\theta_2 > \theta_c$, no light is refracted. Instead

all light undergoes total internal reflection[62,63]. Based on total internal reflection, the planar waveguides are designed whose principle of operation is shown in figure 3.2. If a ray of light enters the waveguide with an angle larger than the critical angle θ_c, the ray will be reflected, and remain in the waveguide.

The ray will propagate, since the incident angle is the same for every reflection, as long as the waveguide is straight. The ray entering at an angle θ_2, smaller than the critical angle will be partly refracted out of the waveguide, and partly reflected. The refraction continues at the next point resulting in rapid decaying of the signal.

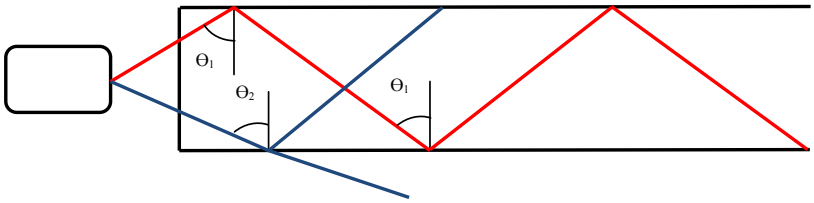

Figure 3.2. Propagation of light in a waveguide: red arrow- above critical angle, propagating in the channel. Blue arrow- Below critical angle results in refraction of light (loss of signal).

3.4 Losses in waveguides

When an electromagnetic wave propagates in a waveguide, the attenuation of signal occurs, this is considered as loss in the waveguide. The Loss of a signal intensity of propagating wave can occur due to scattering, radiation or absorption. This loss is recorded in decibels (dB) which is the ratio of light coupled in to the light collected at the exit. This is often expressed on the $10.\log_{10}$ scale per unit length of the waveguide. Scattering loss can be further divided into surface and volume scattering[64]. Surface scattering is evidently found in the waveguides contributing mainly to the total loss. Volume scattering is a loss occurring due to volume imperfections such as impurity, holes etc. Different types of losses which include both-surface and volume scattering components in a waveguide are as follows[64-66]:

1) Coupling loss- occurs due to many reasons such as misalignment of the optical fiber and the waveguide (lateral, longitudinal and angular), roughness of the fiber and the waveguide end and air gap between the optical fiber and the waveguide. It also accounts for fresnel reflection based losses which occur due to change in the RI of a medium.
2) Transition loss- occurs due to change in the waveguide section-from straight to bend, causing the propagating mode mismatch

3) Propagation loss-occurring due to the absorption and scattering characteristic of the waveguide (volume and surface)
4) Radiation or bending loss- due to distortion of the propagating wave in the bend portion of a waveguide. It depends on the RI contrast between the core and the clad, bend radius, wavelength of light and core diameter. It is a very important factor to take into consideration while designing the bend section of a waveguide.

3.5. Concept of solid-liquid-core waveguide

After relevant discussions about nanoporosity and liquid-core waveguides, let us combine their understanding to develop the concept of Solid-liquid-core waveguides (SLCW). Fundamental difference between the proposed design and other state-of-the art LCW designs is, they use different materials for clad and for core. In our system, different volumes of the same polymer chip are used as the core and the clad respectively.

The average pore size of a typical nanoporous polymer is 10-20 nm. The matrix periodicity between two pores is about 20-40 nm. In the visible light spectrum, the polymer stays transparent and the transmitting light takes into account the effective refractive index of nanoporous system. The transmitted or guidied light has to pass through cross-linked matrix and air/water filled nanopores, which is why the system is called solid-liquid-core waveguide. The nanoporous polymer is intrinsically hydrophobic and this is used as a clad layer (filled with air). The core is filled with water by rendering hydrophilicity in the certain volume of nanoporous polymer. This way water filled core posseses higher refractive index (RI) than the air filled pores which acts as the clad. Using refractive index contrast between liquid filled volume and air filled volume, the coupled light, above critical angle will guide itself in a waveguide.

3.5.1 Working principle of SLCW

Conceptual understanding of fabrication of the SLCW system is depicted in figure 3.3. Figure 3.3a shows schematic drawing of a cross-linked gyroid PB-b-PDMS block copolymer. The refractive index of a block copolymer is 1.46, calculated using Lorentz-Lorenz relation[67]. Chemical etching of PDMS block results in reduction of effective RI of the nanoporous polymer from 1.46 to 1.26 as depicted in figure 3.3b. The nanoporous polymer is hydrophobic in nature at this stage. In order to induce hydrophilicity in the intended volume of the polymer, surface modification of air-polymer interface is carried out. Figure 3.3c illustrates the surface modified hydrophilic nanoporous volume which is filled with water. The refractive index at this stage is calculated to be 1.42. The hydrophilic part of the nanoporous polymer acts as a core of a SLCW with higher RI than the hydrophobic volume surrounding it, which acts as a clad. Since the high RI volume is surrounded by low RI volume, at the conditions of total internal reflection, waveguiding of light occurs.

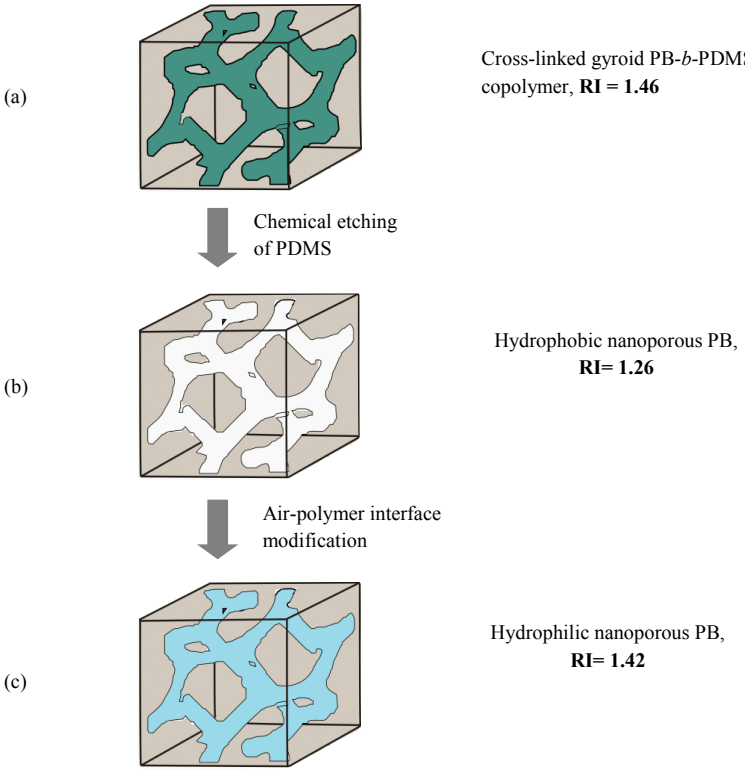

Figure 3.3. Conceptual scheme for fabrication of solid-liquid-core waveguide.

3.5.2 Advantages of SLCW

Different kinds of total internal reflection based LCWs are discussed in the beginning of the chapter. The proposed SLCW system also falls into the category of index guiding (TIR) type. However, it promises to be more effective in many areas compared to the other state-of-the-art waveguide systems. Some of the important advantages are as follows:

1) Since the core and the clad are made from the same nanoporous polymer, higher or lower degree of porosity will not hamper the waveguiding property. The water filled region would exhibit higher RI than air filled region in any case. This degree of flexibility in constructing a waveguide is unique.

2) Chemical nature of nanoporous polymer based SLCW can facilitate specific and unspecific binding sites in the waveguide region. These sites can be exploited for selective detection of molecules in an analyte solution which also acts as a core. Thus, the sensing capability of SLCW for biochemical and chemical analysis is not always straight forward for similar class of LCWs.

3) The pore diameter of gyroid nanoporous polymer is 10-20 nm. This facilitates filtering of large size particles from many turbid analytes like milk or blood, subjected to light guiding[68]. Optical analysis of turbid solutions is challenging due to light scattering caused by larger particles. The current SLCW system can perform filtering combined with waveguiding.

4) Many state-of-the art LCW designs cannot provide planer configurations required for lab-on-a chip devices. SLCWs can be planer in shape which increases its adoptability on the existing microtechnology platform.

After understanding the principle of working, method for fabrication and several advantages of SLCW system, it is appropriate to discuss the two different methods of surface modification for the fabrication of SLCW adopted in the current work. The process of surface modification is very important in the fabrication of SLCW system and it also constitutes as a major scientific contribution from the current work. Therefore, next 3 chapters are dedicated to surface modification by UV photo-oxidation, thiol-ene click chemistry and its application for the fabrication of SLCW devices.

4. Hydrophilization of 1,2-PB by photo-oxidation

4.1 Background and overview

Most synthetic polymers are durable leading to interesting applications where conventional materials like metals, ceramics and glass are substituted. Even though polymers are attractive in many ways, deprivation of mechanical and optical properties in case of prolonged environmental exposure has been an issue on many occasions. In such cases, the degradation process is mainly initiated by UV and visible light in the presence of oxygen. This created a foundation for systematic study of photochemical polymer degradation, and today it is a very well studied system. The main focus of this study is to understand and prevent the degradation of polymeric chains by absorbed light. However, degradation process can also impart interesting properties to the polymers, if the reaction is controlled and well understood. The present work studies photo-oxidative degradation of 1,2-Polybutadiene (1,2-PB) in the presence of air for surface functionalization[69-72]. Polybutadiene photo-oxidation is extensively studied in the past, mainly from the qualitative and kinetic aspects of photo-oxidation. It is reported in the literature that, photo-oxidation of 1,2-PB can form different photo-products which can be hydrophilic in nature. These photo-products are utilized in the context of the current work to produce functional nanoporous surfaces.

It is a known that 1,2-PB with a vinyl pendent group and a tertiary carbon atom acts as a reactive site which develops photosensitivity in the polymer. The initiation reaction happens when the absorbed energy resulting in $\pi \rightarrow \pi^*$ electronic transition in the pendant unsaturation activates C-H bond at the allyl position[73-76]. This in turn, activates tertiary hydrogen atom on the main chain generating polymer radicals by cleavage of C-H bond. Second possibility of initiation is due to impurities or structural defects in the polymer, which acts as a chromophore. Any radical formed due to presence of chromopheres would lead to hydrogen abstraction mechanism described above. Third possibility of initiation reaction would be addition of radical to the pendant vinyl unsaturation. The radical in the pendant group extracts proton from the tertiary carbon creating a stable radical. Further course of the reaction follows the above mentioned initiation mechanism[73, 77].

Most primary photo-products formed after initial photo-oxidation of 1,2-PB are hydroperoxides[70]. After sufficiently longer irradiation times, the hydroperoxide groups are converted into other photo-products. FT-IR study reveals the formation of hydroxyl groups is also derived from the hydroperoxide intermediates[74, 78]. Further decomposition of hydroperoxide results in formation of

carbonyl compounds. These are unconjugated (saturated) and conjugated (unsaturated) keto aldehyde and carboxylic groups[79]. Mass spectrometry compositions of the gasses generated by UV irradiation in air also reveals formation of H_2O, C_2O, CO_2[77].

Wavelength of UV irradiation also plays an important role in deciding stoichiometry of the photo-products. Study reveals that shorter wavelength with higher energy of photons result in higher population of carbonyl compounds[77]. Gel formation or cross-linking reaction is also induced as a consequence of photo-oxidation. Like carbonyl groups, enhancement of the degree of cross-linking is obtained with shorter wavelengths of irradiation[81]. Thus, during the course of photo-oxidation, there is a competition between the chain scission (formation of carbonyl compounds) and cross-linking reaction.

After taking a glimpse of the relevant past work in the area of photo-oxidation of 1,2-PB, we focus on the experimental findings of nanoporous 1,2-PB photo-oxidation reaction. The photo-oxidation reaction in the present case is characterized by spectroscopy i.e. FT-IR, solid state NMR and UV-Vis to determine the nature of chemical groups formed and to investigate the quantitative aspects of the photo-products. The overall surface density of the hydrophilic photo-products and its distribution relative to the polymer-air interface is estimated by gravimetry and titrimetry. The distribution of photo-products along the sample depth is also mapped by energy dispersive X-ray in SEM. Finally the photo-oxidation is used for patterning of hydrophilic structures in the nanoporous polymer for solid-liquid core waveguide optical characterization.

4.2 Photo-oxidation at $\lambda > 300$ nm

A non-collimated UV source with an overall intensity of 14-16 mW/cm^2 is used for photo-oxidation experiments. The nanoporous polymer films of thickness ~ 500 μm are UV irradiated from one side in the presence of air at 38±2^o C for 24 h. It is widely cited in the literature that the absorbance maximum for PB is in the range of 210-230 nm with no absorbance above 290 nm[79]. However, highly cross-linked nanoporous 1,2-PB in the present case shows an absorbance maxima at ~ 300 nm with an absorbing tail up to 390 nm as shown in figure 4.1. This behavior of cross-linked nanoporous PB is studied by UV-Vis spectroscopy in the presence of different solvents to understand the absorbance behavior at higher wavelengths. Figure 4.1 shows cross-linked PB homopolymer and nanoporous polymer films of same thickness in air, methanol and in THF. Methanol is used as a solvent medium for nanoporous polymer since it can compensate for the possible surface scattering of UV which is interpreted at absorption in the UV-Vis spectrometer. This is due to the ability of methanol to fill the nanopores and replace air, which will reduce the refractive index contrast between matrix polymer and nanopores. This results in reduction of the

possible surface scattering at the air-polymer interface. On the other hand, THF can swell the cross-linked polymer which can compensate for the density differences in the PB matrix after thermal cross-linking.

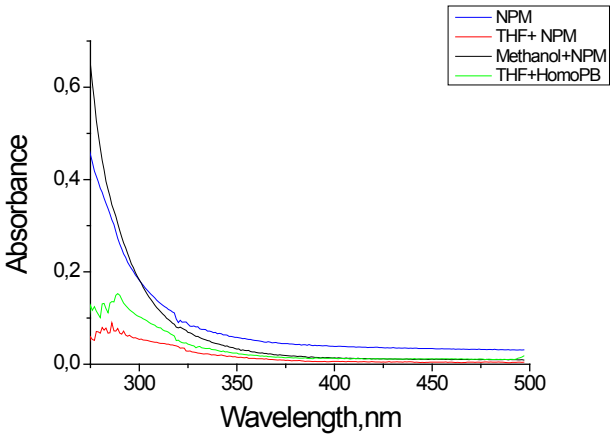

Figure 4.1. UV-Vis spectra of nanoporous and cross-linked homopolymer 1,2-PB film in different surrounding media. Dry nanoporous polymer and nanoporous polymer film in methanol show higher absorption indicating absorption is not due to surface imperfections. Nanoporous polymer in THF and cross-linked homo PB show lower absorption indicative of scattering phenomena due to differential degree of cross-linking across the PB matix.

The homopolymer cross-linked 1,2- PB film of equal thickness in THF is used to compare the absorption or in this case scattering with the nanoporous polymer film. The result shows no significant difference in the absorption behavior of nanoporous film placed in air and in methanol. This suggests the absence of surface scattering contribution at air-polymer interface since. On the other hand, the nanoporous polymer film and homopolymer 1,2-PB film immersed in THF shows absorbance decreased by a factor of 4 compared to nanoporous polymer dry film. This is primarily due to THF entering into the PB cross-linked matrix thereby, partly compensating for the different density zones created due to free radical cross-linking method. Thus, the probable explanation to the scattering of light is the inhomogeneous network density across the thickness of the sample. This difference in the density is causing scattering of light which passes through the polymer, reducing intensity of the transmitted light.

The absorption of nanoporous polymer in UV has an overlap with the emission spectra of the UV source ($300 < \lambda < 400$ nm). Spectra of the UV source used for photo-oxidation has a peak around 350 nm and from figure 4.1, it is evident that the polymer has limited absorption in this wavelength range. That's why the majority of the photons from the UV source can travel through

the entire sample thickness for the modification of the polymer. Thus, the limited absorption is the key in carrying out photo-oxidation of the entire thickness of nanoporous polymer. After this, let us discuss the experimental findings of the photo-oxidation reaction by different analytical techniques.

4.3 Qualitative and quantitative analysis of oxygen containing photo-products

The nature of the photo-products formed after chemical modification is studied by various spectroscopic techniques. The quantitative distribution of oxygen in the form various photo-products is also done using solid state NMR spectroscopy. Let us begin the discussing the FT-IR results of the photo-oxidized nanoporous samples.

FT-IR spectroscopy: FT-IR spectroscopy reveals newly developed overlapping peaks in the hydroxy (OH)/ hydroperoxy (OOH) region after 24 h of photo-oxidation. Further investigation regarding distinction between them is not performed since it is beyond the scope of the current work. A newly developed peak in the carbonyl region is deconvoluted for more specific information regarding its chemical nature i.e. ketones, aldehydes and carboxylic acid etc. It is done by treating photo-oxidized samples with NaOH solution in water. The polymeric carboxylic groups are expected to form carboxylate ions upon reacting with aqueous NaOH, developing new absorption peaks. NaOH staining shows shifting of absorption maxima for carbonyl peak to shorter wavenumber carboxylate ion peak. This confirms that the majority of carbonyl compounds present are in the form of carboxylic groups. The residual peak in the carbonyl region can be due to the presence of saturated ketone groups, as will be discussed with combined understanding of solid state ^{13}C NMR. This hypothesis is also supported by the fact that there is no signature absorption band observed for the C-H stretch in an aldehyde[74]. There are other newly evolved peaks in a photo-oxidized sample indicative of C-O bonds in aliphatic and vinyl ethers or alcohols.

An interesting development observed during photo-oxidation reaction is shown in figure 4.2. It illustrates ATR-FT-IR spectra of nanoporous sample photo-oxidized at different times. Sample with no UV exposure shows no absorption in the carbonyl region (around 1720 cm^{-1}). However, after 8 h of exposure, 2 distinct peaks i.e. at 1640 cm^{-1} and 1720 cm^{-1} are developing in tandem. The peak around 1640 cm^{-1} can be attributed to α-β unsaturated carbonyl compounds[80]. This is typical behavior for conjugated carbonyl compounds due to the de-localization of the π bond electrons of the C=O[75, 80]. At this stage, the saturated carbonyl peak at 1720 cm^{-1} is growing parallel to unsaturated ones. As the reaction grows in time, a tendency of rapid growth of saturated carbonyls compared to unsaturated compounds is observed. Formation of unsaturated carbonyls is

slowed down after a certain time whereas the saturated carbonyl peak grows with respect to the reaction time.

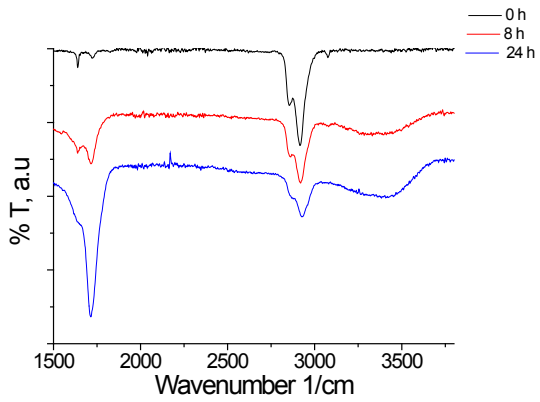

Figure 4.2. FTIR spectra of photo-oxidized nanoporous polymer at different UV irradiation times. Newly evolved peak at 1640 indicative of α-β unsaturated carbonyl and 1710 cm^{-1} indicative of carboxylic acid is seen after 8 h of UV irradiation. During the course of photo-oxidation reaction, peak developing at 1640 cm^{-1} tends to stop while peak at 1710 cm^{-1} continues to grow with time. The spectra are normalized to the hydrocarbon stretch 2917 cm^{-1} and shown offset for the sake of clarity.

Solid state 13C-NMR: Solid state NMR of the cross-linked sample reveals qualitative as well as quantitative information of the photo-oxidized nanoporous polymer. Sufficient trial runs are carried out for obtaining an adequate delay time for NMR before recording the final spectra of the photo-oxidized polymer. The delay time used for the current analysis is 15 s insuring relaxation of quaternary carbon atoms (ketone, aldehyde, carboxylic acids etc) for evolution of the complete peak. The ^{13}C-NMR provides vital information about the composition of the oxygen containing photo-products. It suggests that the oxygen photo fixation is carried out mainly from saturated carbon atoms (tertiary carbon) site. Based on the C:O ratio in different photo-products for e.g. 0.5 in COOH groups, and knowing total amount of reacted molecular oxygen per g of nanoporous polymer, we can calculate oxygen fixation in the form of different chemical groups. As per the results, we have COOH (43% of the oxygen-containing groups), ethers (23%), alcohols (24%), and saturated ketones (10%) present in the photo-oxidized sample. Large access of molecular oxygen in the nanopores causes formation of the oxygen radicals, driving the reaction towards Norrish I mechanism forming saturated and unsaturated carboxylic acid groups (Scheme 4.1). This is an important understanding of the process where an abundance of molecular oxygen can influence the nature of photo-products i.e. more hydrophilic groups (carboxylic acid) in this case resulting in hydrophilic behavior of the polymer.

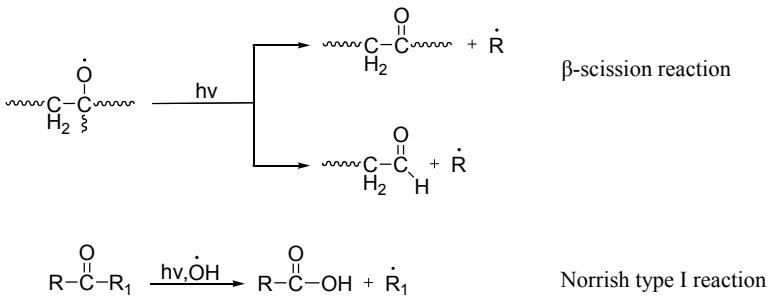

Scheme 4.1. Photo-oxidation of 1,2-PB forming ketones and carboxylic acid groups from alkoxy radical in the presence of abundant molecular oxygen.

UV-Vis spectroscopy: UV-Vis spectroscopic analysis of nanoporous polymer before and after photo-oxidation is also performed. After 24 h of photo-oxidation, absorbance in the visible range (λ = 400-475 nm) is increased compared to the unmodified sample. In other words, the absorption maxima experience a shift towards higher wavelengths. The nanoporous polymer samples absorbing in the 400-475 range or turning yellow can be attributed to the presence of α, β-unsaturated carboxylic acid or ketone groups. The probable explanation is that a normal double bond consists of a bonding and an anti-bonding π orbital. In case of a conjugated system, at the condition of co-planarity, π bonds on different carbon atoms in the main chain tends to overlap resulting in π-π conjugate which shifts the absorbance to the higher wavelengths. Thus, UV-Vis observations about possible presence of unsaturated carbonyl compounds falls in line with the earlier interpretations made with FT-IR[72, 74, 75, 78].

Static Contact angle measurement: Static contact angle measurement on the photo-oxidized nanoporous polymer film is presented in figure 4.3. It shows hydrophilic behavior of the nanoporous polymer after photo-oxidation reaction. This implies that the UV photo-oxidation renders sufficient surface density of the hydrophilic photo-products in nanoporous polymer system, tuning its affinity towards aqueous media. Original contact angle of a nanoporous polymer (hydrophobic) is measured to be 96^{o} (picture not shown). The water droplet doesn't evaporate completely even after 10 min from the hydrophobic surface. In the case of UV modified nanoporous polymer, within 7 min, a water droplet is pulled inwards by capillary forces exerted by the nanopores. This is due to carboxylic acid groups formed in on the polymer-air interface as a consequence of photo-oxidation reaction.

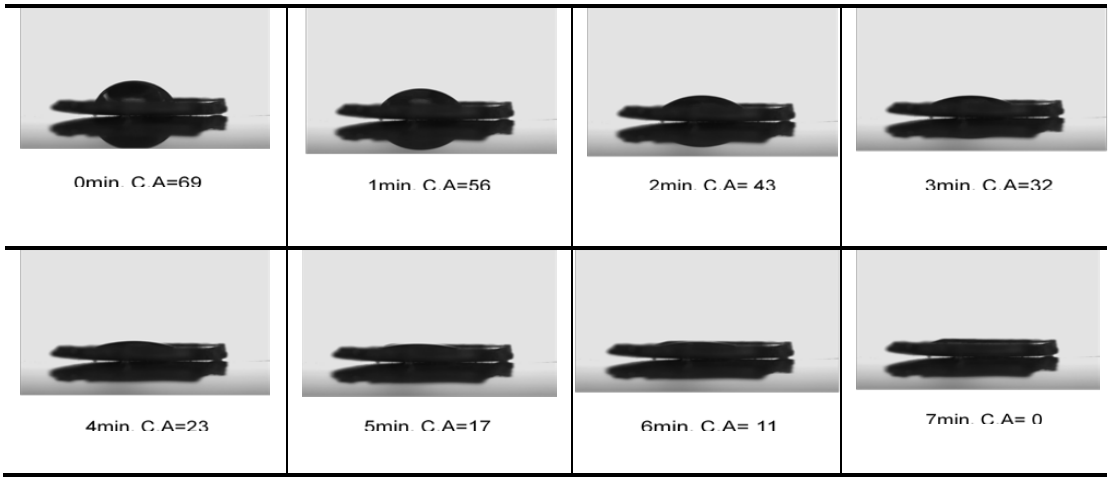

Figure 4.3. Static contact angle measurement on UV photo-oxidized nanoporous polymer (side facing the UV source). Contact angle of water on UV photo-oxidized sample is measured as function of time. It is evident that with passing time, the contact angle is reducing due to suction of water into the nanopores. After 7 min the entire droplet is pulled inwards indicative of hydrophilic polymer-air interface.

4.4 Distribution of carboxylic group relative to polymer-air interface

Nanoporous nature of the polymer provides vast internal surface area available for photo-fixation of molecular oxygen onto the polymer-air interface. The amount of oxygen fixed on to the nanopores can be quantified by simple gravimetric analysis to reveal vital information on the nanometer scale. In this case, gravimetric analysis is done before and after photo-oxidation and after NaOH staining to obtain information about the distribution of oxygen in the form of various photo-products. Gravimetric results indicate the fraction of oxygen present in the form of COOH groups is 57% of the total oxygen fixed in the polymer. The remaining 43% of the oxygen is present in the form other photochemical groups. This result is in agreement with the results obtained from solid state NMR which estimates 60% of the total oxygen present in the form of COOH groups.

An average surface density of carboxylic groups is also estimated by gravimetry of NaOH stained samples. The dry mass increase and the internal surface area of the nanoporous polymer are used as a basis for calculating overall surface density of carboxylic groups. The average surface density of carboxylic groups over the entire internal surface area of 280±40 m^2g^{-1} is calculated to be 5.4±0.7 nm^{-2}. Titration experiment is performed alongside gravimetry to obtain the average surface density of carboxylic groups. Titration of COOH groups is done by treating photo-oxidized polymer with basic NaOH (in excess), which is neutralized with potassium hydrogen phthalate.

The moles of NaOH neutralized and the internal surface area of the polymer are used to calculate the average surface density of carboxylic groups present in the polymer. The surface density calculated from this experiment is 5.5±0.9 nm^{-2}, which is in good agreement with the gravimetric analysis.

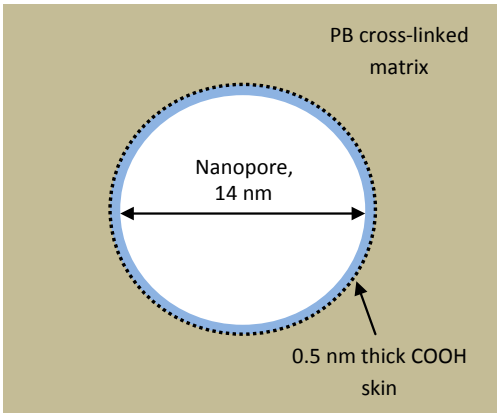

Figure 4.4. Schematic representation of distribution of COOH groups relative to the polymer-air interface in the nanoporous polymer.

Photo-oxidized samples treated with NaOH solution are used to map the distribution of carboxylic groups relative to the polymer-air interface. This analysis can give very important information about the possible concentration gradient of the carboxylic groups away from the nanopores interface. The distribution of such kind can greatly influence sharpness of the lithographic structures for solid-liquid core waveguides. Let us imagine if the concentration of the carboxylic groups is decaying gradually from the air-polymer interface to the bulk of the polymer. In this case, the boundary of the lithographic hydrophilic structures will be diffused and not sharp. This may result in the loss of an optical wave guiding in a liquid core due to surface scattering. Therefore, it is required to predict how controlled the photo-oxidative hydrophilization reaction is in order to understand the surface scattering losses that can incur in the liquid-core waveguide. The distribution analysis of carboxylic groups relative to the polymer-air interface shows about 93% of the total concentration located within the thickness of ~ 0.5 nm. This means that majority of the hydrophilic groups are located at the interface and a small fraction of the total concentration is located away from the nanoporous interface. The schematic representation of the distribution is shown in figure 4.4. This is very important information for the waveguiding purposes since it is expected to have low surface scattering losses while light guiding due to a step function of the concentration of hydrophilic groups relative to the nanoporous interface. The narrow oxidation

skin can be a consequence of the high degree of cross-linking of 1,2-PB matrix at the interface. This results in poor permeability of oxygen into the cross-linked matrix resulting in largely unmodified polybutadiene matrix.

4.5 Distribution of carboxylic groups relative to the sample depth

Distribution of polymeric carboxylic groups across the sample depth is characterized by Energy Dispersive x-ray spectroscopy (EDX) in SEM[81] and ATR FT-IR. EDX probe identifies various elements present in sample subjected for SEM analysis. In the present case, atomic % of 'C', 'O' and 'Na' across 500 μm sample thickness is identified. The results illustrate considerable reduction in oxygen concentration as a function of the sample depth. The surface facing UV irradiation registers about 4 times higher concentration of oxygen in the top 100 μm thickness than the rest 400 μm, which is a uniform concentration zone. This can be a consequence of shorter wavelength photons ($\lambda < 350$ nm) effectively absorbed within first 100 μm bringing about the surface modification. The longer wavelength (less energy) photons are capable of transmitting through the depth, thereby modifying the entire thickness of the sample. Similar trend is obtained when carboxylic groups mapping by Na abundance is done in EDX. This means the relative abundance of oxygen to carboxylic acid groups is same for the entire sample depth. This is compared with ATR FT-IR analysis done at different depths of the sample. At each level, 3 measurements at different spots are done to obtain statistical data for FT-IR measurements. Relative concentration of COOH groups obtained by FT-IR across the sample depth is in line with the experimental findings by EDX. The results obtained from EDX and FT-IR analysis shows that, the nature of modification virtually remains the same throughout the sample; with a difference in the concentration of photo-products across the depth. This indicates the abundance of COOH groups relative to the total fixed oxygen is constant for the entire sample thickness. The EDX measurement can also estimate the amount of oxygen present in the form of COOH groups relative to the total fixed oxygen. Relative areas under the curves of O and Na give an average fraction of oxygen present in the form of COOH groups as 0.61. This observation is in agreement with 0.60 obtained by solid state NMR and 0.57 given by the gravimetry.

4.6 Optical characterization

The following work is mainly carried out by Nimi Gopalakrishnan, responsible for the optics measurement in the project. It finds space in the report due to its immediate relevance in the context of photo-oxidation process.

Selection of appropriate wavelength of light for guiding experiment is important so that it does not get absorbed by the liquid-core waveguide device. As discussed in UV-Vis results in section 4.3,

the photo-oxidized nanoporous polymer tends to absorb light in the blue region. A transmission measurement is performed with green light (532 nm) and red light (655 nm) on the photo-oxidized sample. It shows that the green light in photo-oxidized region tends to absorb ~ 69 % of the incident light in the UV exposed region. In case of red light, due to the higher wavelength the transmission, it records no absorbance in the UV exposed region. Therefore, Red light source is chosen for the SLCW optical characterization. Propagation loss in the waveguide is measured using a cutback technique[82]. Waveguide cross section is 200 × 200 μm defined by UV photo - oxidation (lithography in this case) using appropriate masks. He-Ne laser (632.8 nm) is coupled into the SLCW with a multimode fiber and the other end of the waveguide is coupled to an optical spectrum analyzer with the similar fiber. Each waveguide has different straight length sections connected by a 90^{o} bend of 2 mm radius which removes the coupling and radiation loss. The final loss in the straight parts of the waveguide is deduced by subtracting bending losses. The propagation loss is plotted as a function of total length (straight) and the slope gives propagation loss in the waveguide, whereas the Y intercept gives value of transition losses. The loss measurement showed propagation loss of 0.62±0.03 dB/mm and transition loss of 3.8±0.5 dB/mm in our system. Bending loss is evaluated with a different mask having different radius ranging from 1.75-11.75 mm, each sandwiched between 2 mm of straight waveguides. The bend loss in the system is measured to 0.81 dB/90^{o} for the bend radius of 1.75 mm. The current system records high propagation losses compared to some of other state-of-the art LCW technologies i.e. 0.03 dB/mm for Teflon AF 2400 waveguides[2]. The losses in the current system can be reduced by reducing the surface roughness at the air-polymer interface after photo-oxidation. The current system uses a non-collimated light source and UV photo-oxidation method, both results in less defined boundaries for the hydrophilic microchannel. Additional surface scattering losses incur primarily due to the fabrication technique of the nanoporous polymer film in a glass petridish. The solvent casting in a petridish consists of an open surface i.e. facing air, which most probably has unevenness in the micron scale, causing scattering of the coupled light. The above mentioned factors causing higher propagation loss in the waveguides are addressed categorically in thiol-ene based surface modification approach (discussed in the succeeding chapters) for fabrication of SLCW devices.

5. Hydrophilization of 1,2-PB by thiol-ene click chemistry

5.1 Introduction

The concept of 'click' reactions for the preparation of functional macromolecules is introduced by Sharpless et al[83]. They defined click reaction as the reaction which is modular, gives quantitative yields, doesn't generate hazardous byproducts and final product can be extracted easily by non-chromatographic techniques. The reaction should be insensitive to water and oxygen and can be performed with readily available starting materials, with the ease of isolation of targeted product[84, 85]. Initially azide-alkyne cycloaddtion mechanism was mainly used in click reactions, which started sharing space with other click mechanisms like diel-alder, thiol-yne, thiol-ene and thiol-isocynate reactions. In the present case, use of azide-alkyne reaction is not considered due to strong coloring of the reactants. Strongly colored polymers are not suitable for the LCWs applications which require clear and uncolored polymeric devices. Secondly by choosing thiol-ene chemistry, we avoid an additional step of creating a triple bond in butadiene needed for azide-alkyne mechanism. With thiol-ene click reaction, we rely on the pendant double bonds available at the air-polymer interface of the nanoporous polybutadiene for performing thiol-ene chemistry.

Use of sulfur molecules in chemical reactions is around for over 100 years. Charles Goodyear first patented sulfur based natural rubber vulcanization in the mid-19th century. This initiated the trend of radical addition to a non-activated carbon-carbon double bond[85] and laid foundation to perform thiol based reactions in the synthetic chemistry. Today various other kinds of unsaturations like in acrylaytes, malemides or norbornens are also been utilized for carrying out thiol chemistry. Thiol-ene chemistry research is propelled with detailed understanding of its mechanism, kinetics, effect on reactivities of monomer units, and its effect on relaxation of polymer. The increasing interest in this field is due to some of the exceptional features of the reaction like orthogonality, tolerance to variety of solvent systems, high yield and efficient nature of reactions[12, 86-88]. These numerous advantages of thiol-ene reactions acquired a lot of importance in the world of macromolecular chemistry.

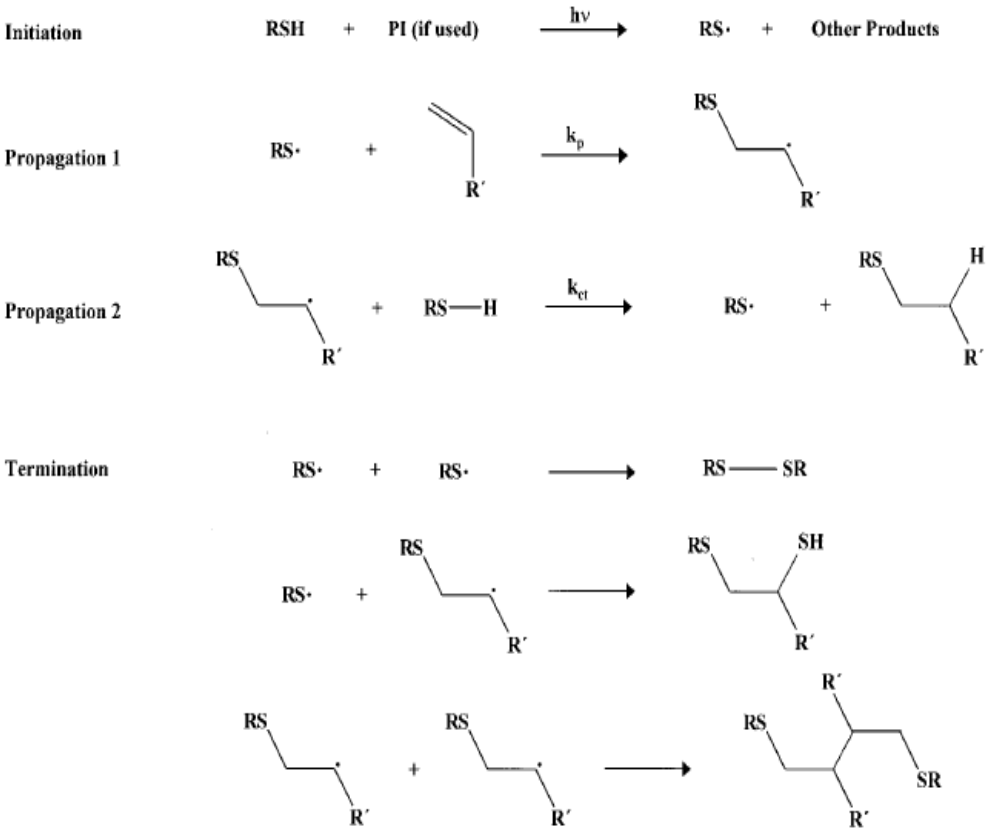

Scheme 5.1. Thiol-ene photo-polymerization scheme showing different stages of the reaction. The photo-initiator generates thiyl radicals under UV to initiate the reaction. The propagating reaction takes place by 2 possible routes. Finally 3 plausible mechanisms for the termination reaction are shown[12].

Thiol-ene reactions are carried out between a multifunctional thiol molecule and an ene (R-C=C-R_1) unsaturation in a step growth fashion, mainly with the radical addition. Radical centers are generated by thermal free radical initiators or photoinitiatiors as depicted in scheme 5.1. An initiator is excited by thermal excitation or UV irradiation which abstracts hydrogen from thiol monomer generating a thiyl radical. The thiyl radical can either terminate by recombination or propagate the reaction. The propagation mechanism is of two types: sequential propagation and chain transfer mechanism. It is generally assumed that at equal concentrations of thiol and ene functionalities, the rate consumption of reagents is identical[12, 89].The termination step is occurred by radical recombination step. Another plausible way of termination is recombination of growing radical with the initiating radical center. This is usually the case with benzophenone as photo-

initiator which result in a pinacol radical site (Ar_2C^*-OH), potentially incapable of initiation but can terminate a growing radical[90-93].

The conversion rate of thiol-ene chain reaction depends on electron density of the 'ene' functional group. The electron rich ene groups tend to react faster than the electron poor ones except for few conjugated dienes. Moreover the degree of substitution plays a role in reactivity of the ene functionality; higher the degree of substitution, lesser the reactivity of a chemical group[12]. Double bond position is also a key factor which determines rate of the thiol-ene reaction. If the double bond is in the main chain, it can result into reversible addition of the thiyl radical to a disubstituted ene function group (typical with *cis-ene* functionalities). This kind of dynamic equilibrium can be rate determining in the course of thiol-ene reactions. Thus steric hindrance is an important factor in a thiol-ene two step propagation mechanism. Faster reaction rates are expected with the terminal ene functionalities[94, 95]. The thiol structure also plays an important role in deciding the rate of the reaction. For instance, hydrogen bonding with thiol molecule can result in weakening of the sulfur-hydrogen bond consequences in faster reaction rates. Therefore thiols with ester carbonyl (propionate esters) have reported higher radical addition rate compared to simple thiol structures (without possibility of hydrogen bonding) like pentanethiol[12, 85].

One of the highlights of thiol-ene reactions is its ability to form uniform cross-links in a polymer matrix. This is due to the fact that gel point is achieved at very high degree of conversion. In a conventional free radical cross-linking reaction, viscosity begins to increase after 20-30 % of double bond conversion. Whereas, the thiol-ene reaction experiences this drastic change of viscosity after 60-70% of thiol functional groups conversion, contrary to the free radical gelation[96, 97]. The majority of the thiol conversion takes place while the reactants are in the liquid phase, allowing much lower stress built up in the polymer networks. This way it is possible to reduce the final shrinkage in the polymer.

Almost all thiol-ene combinations share insensitivity to the presence of oxygen. Molecular oxygen can attack a tertiary carbon forming peroxy radicals. This can abstract hydrogen from the thiol or another vinyl unsaturation which will form hydroperoxy group at allylic position. The hydrogen abstraction results in formation of a thiyl or vinyl radical, which ultimately resumes propagation by addition of resultant radical to vinyl unsaturation or a fresh thiol functional group[98]. Thiol-ene polymerized films are also reported to have high thermal and oxidative stability compared to the free radically polymerized films. High thermal stability is the consequence of narrow glass transition distribution of the polymer suitable for modulable optical components. The reduces internal stresses[99] which in turn, increases adhesion property of the polymer to different surfaces, desirable in case of acrylates. These polymers typically find applications in coating optical fibers and adhesives.

Why Thiol-ene chemistry with nanoporous polymer

High degree of flexibility and ease of carrying out thiol-ene reaction is utilized in the context of the current work for the fabrication of nanoporous polymer based solid-liquid-core waveguides. This needs tailoring of hydrophilicity in the desired nanoporous volume which is otherwise hydrophobic as discussed earlier. The polybutadiene matrix is offering 30- 40% of its original vinyl unsaturated reactive sites after thermal cross-linking step. Due to the vast internal surface area, about 12% of these double bonds are located at the polymer-air interface. Assuming uniform cross-linking taking place in the matrix and at the interface between PB and PDMS, we have about 5% of the total terminal double bonds available for further chemistry. Thus the motivation for using thiol-ene reaction can be summarized in salient points as follows:

- Abundant vinyl groups available for thiol-ene chemistry
- Vinyl unsaturation is in the pendant groups which favors faster reaction with thiols
- No stringent reaction requirements
- Very high rate of reaction- fast tuning of hydrophilicity in this case
- Quantitative yield of the reaction
- Insensitivity to oxygen and solvent presence
- Commercial availability of large number of hydrophilic thiols

After discussing the theoretical background and important features of thiol-ene chemistry for nanoporous polymer, we look at the conditions for the thiol-ene reaction in nanoporous 1,2- PB. Further analysis of the reaction using spectroscopy (FT-IR and UV-Vis), contact angle and nitrogen adsorption are discussed. Quantum yields for the step growth free radical reaction are also estimated to comment on the nature of the hydrophilization reaction. Kinetic study of hydrophilic films is also performed for dry mass uptake and water mass uptake after thiol grafting at different irradiation times.

5.2 Reaction conditions

A collimated He (Xe) 1000 W pressure lamp filtered at 365 nm is used for thiol grafting in the nanopores. 2,2-dimethoxy 2-phenyl acetophenone (DMPA) is used as a photoinitiator (10mM) with Mercaptosuccinic acid (MSA) and sodium 2-mercaptoethanesulfonate (MESNA) (500mM) are used as hydrophilic thiol molecues in ethanol and methanol-water (75/25, v/v) mixture respectively. The nanoporous polymer samples used for the reaction are weighing 8-20 mg (0.68-1.70 cm^2) with 195±5 μm thickness. Following section discusses the choice of particular reaction conditions for the greater understanding of the selection criteria.

Collimated UVsource: **A** collimated UV source results in better edge definition for the lithography process. The wavelength of 365 nm has higher penetration depth in the polymer ensuring uniform absorption of light for the entire thickness of the nanoporous film. Secondly 365 nm is widely used on the standard photolithography bench, making the process adaptable in the existing microfabrication set up.

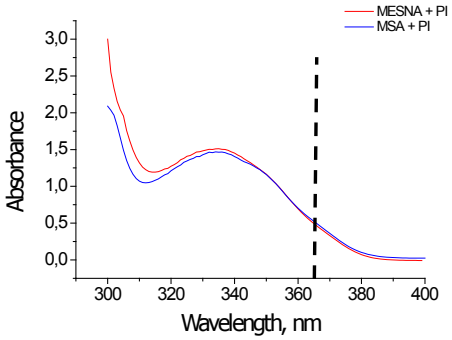

Figure 5.1. UV-Vis spectra of MESNA and MSA (500 mM) with photoinitiator (10 mM) in 75/25 (v/v) methanol to water and ethanol solution respectively.

Figure 5.1 shows UV-vis spectra for two thiols along with the photoinitiator in their respective solutions. The absorption maxima for both thiol systems are around 340 nm. The absorption reduces from there for higher wavelengths but shows sufficient absorption of light at 365 nm which can carry out thiol-ne reaction in the present system.

Photoinitiator: Due to its higher efficiency, DMPA is selected as a photoinitiator over other photoinitiators (diaryl ketones) for e.g. benzophenone. Benzophenone in the presence of UV irradiation can be excited to singlet state which further goes through an intersystem crossing to a triplet state. In this state, the triplet state benzophenone molecule cleaves a sulfur-hydrogen bond and abstracts hydrogen, generating a semipinacol radical (Ar_2C^*-OH). This semipinacol radical is incapable of reacting with the thiol group on its own and stays in the system as a photoreactive component. This leads to yellowing of the samples (absorption in blue region). On the other hand, DMPA is a cleavage type of photoinitiator which generates a methyl and benzoyl radical, both capable of initiating the reaction. This way DMPA is more efficient compared to benzophenone due to its high quantum yield[12].

Photoinitiator to thiol ratio is maintained 1:50 in this case. Different molar ratios of photoinitiator to thiol are not tried in the current work but it is expected that the ratio lower than 1:50 can result in lower overall reaction rates. On the other hand, too high photoinitiator to thiol ratio can result in

excessive reactive radical sites in the thiol system, which may result in unwanted termination reactions with propagating thiyl or vinyl radical.

Thiol functionality: MSA and MESNA are chosen for the thiol-ene photografting reaction. Figure 5.2 depicts the chemical formula for MSA and MESNA. MSA is a dicarboxylic acid molecule where as MESNA has a sodium sulfonate (salt) functional end group. Both the functionalities are expected to have high affinity towards aqueous solutions and thus can render hydrophilicity on to the polymer-air interface upon photo-grafting reaction.

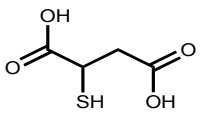

Mercaptosuccinic acid (MSA)

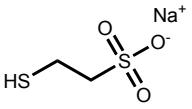

Sodium mercaptoethanesulfonate (MESNA)

Figure 5.2. Chemical formula of hydrophilic thiol molecules.

The double concentration at the air-polymer interface after cross-linking is about 500 mM/L. Thus, the current thiol-ene reaction is carried out at 1:1 molar concentration of thiol to ene functionalities at the nanoporous interface.

Solvent system: MSA with photoinitiator uses ethanol as solvent whereas MESNA with photoinitiator used 25/75 (v/v) of water to methanol mixture. Choice of solvent is based on its capability of completely dissolving both thiol and photoinitiator in above mentioned concentrations with relative ease. Secondly, both solvent systems are capable of filling nanoporous, with little penetration into the cross-linked matrix. Thus the chosen solvent system is expected to address all the interfacial double bonds with thiol and photoinitiator solution.

In the next section, we discuss thiol-ene click reaction at the above mentioned reaction conditions. We present an anticipated reaction scheme along with some important experimental findings using different analytical techniques.

5.3 Results and Discussions

The anticipated thiol-ene reaction between hydrophilic thiol molecule and a terminal vinyl unsaturation at the polymer-air interface is presented in scheme 5.2. Under UV irradiation, DMPA radical triggers the initiation which generates thiyl radicals. During the propagation reaction, covalent bonding of thiol with an allylic carbon in the pendant vinyl unsaturation takes place. The hydrophilization reaction of the nanoporous polymer is first confirmed by static contact angle measurement. The unmodified polymer records a contact angle of 101 ± 3^{o}, which is drastically

reduced to 35±2° and 24±2° in case of MSA and MESNA respectively. The water droplet pulled into the nanopores by micro-capillary forces due to its reduced contact angle (hydrophilic polymer-air interface) within the span of 25 s. Similar behavior on the back side (rear side) of the sample suggests homogeneous degree of modification reaction in the entire sample thickness.

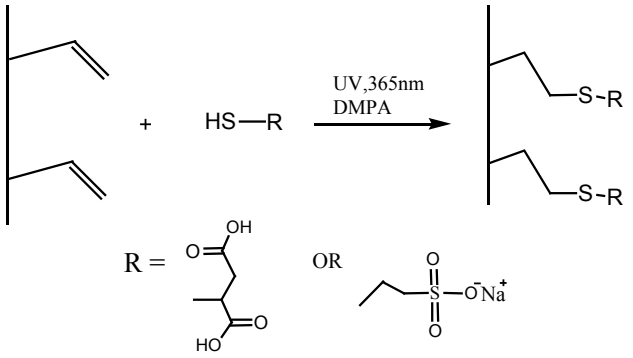

Scheme 5.2. Reaction scheme of thiol-ene photo-grafting reaction at the polymer-air interface in nanoporous polymer.

5.3.1 Spectroscopic analysis

ATR FT-IR analysis of the thiol modified nanoporous polymer shows newly evolved characteristic peaks for carboxylic acid and S=O groups. The peak for the pendant vinyl unsaturation is also reduced in both-MSA and MESNA modified samples compared to the unmodified nanoporous polymer sample. This shows covalent bonding of thiol on the nanoporous interface. Figure 5.3 shows a series of ATR FT-IR spectra, recorded at different depths on the MSA modified sample by polishing it thinner. Polishing facilitates recording of infrared spectra at different depths for studying the degree of homogeneity of the reaction similar to photo-oxidation case. At each depth, three FT-IR measurements are done at different spots. Due to similarity of the entire process, repetition of the experiment with MESNA sample is not performed. The X-axis in figure 5.3 represents depth in the nanoporous polymer sample and the Y-axis depicts absorbance peak for carboxylic acid normalized by the C-H sp^3 hybridized stretch.

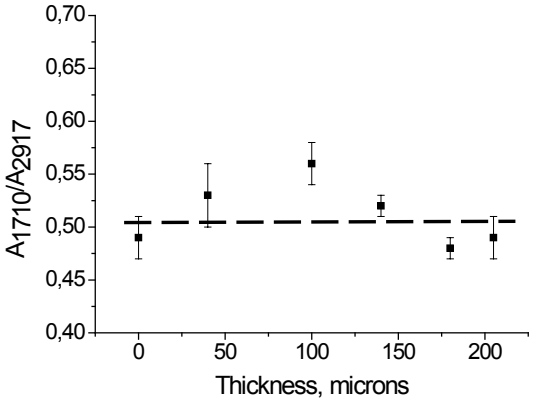

Figure 5.3. Depth profile of carboxylic groups mapped with ATR FT-IR in MSA modified nanoporous polymer sample. FT-IR absorption peak intensity at various depths is recorded indicating relatively homogeneous surface density of carboxylic groups. The point at 100 μm showing highest intensity for COOH groups is unclear and can be non-generic.

The Y-axis represents local population of carboxylic groups within the sample depth of 3.5-5 μm covalently attached to the nanoporous walls. The graphical trend suggests that the surface density of carboxylic groups is relatively uniform throughout the sample thickness unlike UV photo-oxidation case in previous chapter. The uniform distribution of thiol groups for the entire thickness can be beneficial for low propagation losses in a solid-liquid core waveguide. The sample is showing a maxima at 100 μm which is unexplainable and can be considered as not generic trend with the existing process.

UV-Vis spectroscopy results of nanoporous polymer samples before and after thiol-ene treatment are shown in figure 5.4. The measurement is performed on dry nanoporous films in a quartz cuvette. The absorbance for MSA treated sample below 350 nm shows slight increase in absorbance value compared to the reference (untreated) nanoporous polymer sample. The MESNA sample shows more absorption below 350 nm wavelength range than the MSA sample. In both the cases, the absorption behavior after 60 min of reaction time is considerably small compared to UV photo-oxidation samples (spectra not shown here). In other words, the samples do not absorb light in the blue region resulting in transparent samples which allows guiding in blue and green light. This imparts greater degree of flexibility for SLCW applications since surface modification is no longer a bottleneck for deciding wavelength of the guiding light. This allows possible usage of thiol modified devices with different kinds of liquid cores which require guiding of shorter wavelengths of light.

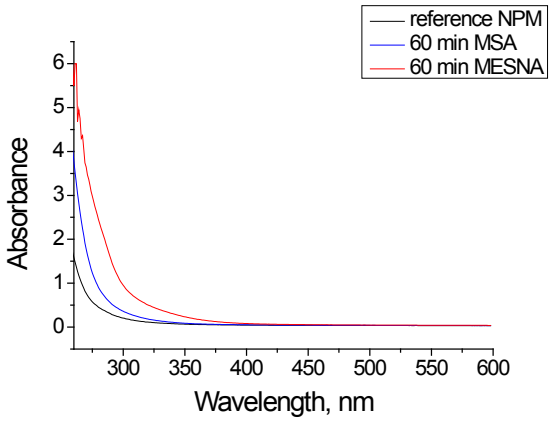

Figure 5.4. It shows UV-Vis spectroscopy results of the nanoporous polymer before and after thiol-ene treatment for 60 min. MSA and MESNA shows slight increase in the absorption at $\lambda < 350$ nm. The low absorption of thiol modified devices allows light guiding at shorter wavelengths in the visible spectrum.

5.3.2 Quantum Yield of Photo-reaction

The knowledge of quantum yield (QY) is important for understanding the nature of a photo-chemical reaction. It is important to note that QY calculation is done considering the initial reaction rate. The initial rate of photo-reaction is when the reagent concentrations are expected to be maximum; therefore it is the ideal stage for calculation of QY. The QY calculated for grafting reaction is 21±3 and 76±6 for the MSA and MESNA system respectively. The high numbers (QY >1) show chain reaction between thiols and vinyl unsaturation in PB. The higher QY for MESNA compared to MSA can be a function of steric hindrance as discussed earlier in this chapter. The Thiol molecule in case of MESNA is primary whereas, the MSA thiol molecule is secondary in nature. The primary thiol may experience less steric hindrance compared to the secondary thiol resulting in a higher overall quantum yield of reaction. It is important to note that the high quantum yield numbers for thiol-ene compared to photo-oxidation reaction (QY= 0.24±0.03)[6] explains why reaction times for the thiol-ene click reactions are significantly lower than the photo-oxidative modification.

5.3.3 Gravimetric analysis

Simple gravimetry can be used to deduce vital information regarding the kinetics of the reaction in the nanoporous polymer. In the present case, mass uptake due to thiol photo-grafting is recorded as a function of time for both the systems. The kinetic trend of the click reaction in both MSA and MESNA can be roughly divided into 3 distinct zones as shown in figure5.5.

Zone a- The initial rate of thiol grafting on to pendant vinyl unsaturation located at the nanoporous interface is highest. The steep slope of the curve in this zone is indicating the rapid rate of thiol-ene click reaction. About 80-85 % of the total mass increase due to thiol grafting takes place in initial phase of the reaction for both the reactions. The difference in the time scale in MSA and MESNA (being faster) can be attributed to the fact that MESNA has greater chances of forming hydrogen bonds (intermolecular and intramolecular) resulting in more labile hydrogen atom which is easy to abstract[12]. Secondly this can be a consequence of steric hindrance in case of MSA resulting in slower rate of thiol grafting reaction.

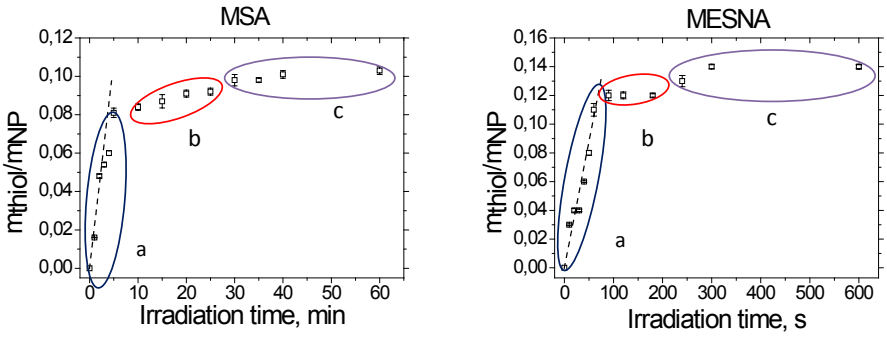

Figure 5.5. Mass uptake profile of photo-grafted thiols onto the polymer-air interface in the nanoporous polymer. Mass uptake rate of thiol for both the systems is rapid in the initial phase of UV irradiation. Upon consumption of *ene* functionalities and photoinitiator, the mass uptake rate reduces. At higher irradiation times, slight increase in the reaction rate is experienced which can be attributed to the reaction of 1,4-PB *ene* units.

Zone b- The mass uptake profile for both the thiol systems hits a plateau where the reaction rate slows down. This can be due to depletion of the ene functionality after a quick consumption in the initial run of thiol-ene photo-fixation. It also hints towards the possible depletion of photoinitiator concentration in the solution.

Zone c- The last part of the mass uptake curve experiences a slight increase in the rate of reaction possibly due to the reaction of 1,4-mainchain unsaturated double bonds in PB at the polymer-air interface.

Gravimetry facilitates the calculation of the moles of thiol molecules grafted per g of nanoporous polymer. This is translated into the number of groups per nm^2 as previously done in the photo-oxidation case. The distribution of groups per area is plotted against the water mass uptake per nanoporous polymer (original) mass. From the analysis, a hydrophilic jump from very little to considerable water uptake is observed within 1 min in case of MSA and 30 s in the case of

MESNA. This is an indication of homogeneous hydrophilization process of photo-grafting resulting in a spontaneous increase in the water uptake. It supports the argument earlier made with FT-IR analysis for the homogeneity of the reaction. The critical surface density of hydrophilic groups required to fill 50% nanoporous volume with water in case of MSA (0.95 groups/nm^2) is more than in the case of MESNA (0.53 groups/nm^2). This can be due to the presence of terminal sodium sulfonate group which is more hydrophilic in nature than the carboxylic acid groups. The maximum number of groups per nm^2 formed in case of MESNA is equal to the initial available pendant vinyl groups which are calculated theoretically. In case of MSA about 83% of the initial pendant vinyl groups are consumed. These observations reiterate the quantitative nature of the thiol-ene click reactions. Finally the maximum water uptake is in agreement with the calculated volume porosity for the nanoporous polymer system within the range of experimental accuracy.

5.3.4 Nitrogen adsorption test and SEM

Nitrogen adsorption test is done to calculate the internal surface area of a porous sample. It is performed on to the unmodified nanoporous polymer and thiol modified (both MSA and MESNA) samples to verify the changes in the total internal surface area after the click reaction. This is also useful in predicting possible structural changes which may have taken place, changing morphological characteristics of the nanoporous polymer. Nitrogen adsorption test reported internal surface area of 283±14 m^2g^{-1} for the nanoporous polymer sample before the click reaction. After thiol photo-grafting, in case of MSA it is reported to be 282±14 m^2/g and for MESNA it is 276±14 m^2/g. This shows that the photo-grafting of thiol is marginally reducing the pore diameter which will reduce the final surface area. Within the experimental limits of nitrogen adsorption test, it is difficult to comment on the absolute value of the reduced surface area after thiol-ene reaction. It still proves that the polymer retains nanoporosity after thiol-ene reaction which exhibits a large internal surface area.

To sum up the story, thiol-ene reaction in nanoporous polymer results in a fast, specific, quantitative, homogeneous and rather easy way of modifying large internal surface with no demanding reaction conditions. The following chapters discuss its implementation in the fabricating of SLCW and further usage in biochemical sensing applications.

6. Solid-liquid-core waveguide fabrication by thiol-ene photochemistry

6.1 Background

In the previous chapter, we discussed thiol-ene photo-grafting reaction on the nanoporous interface extensively. It mainly covered the various chemical aspects associated with the thiol photo-modification of the nanoporous polymer. In the current chapter, the focus is more on applicability of the reaction for opto-fluidics applications i.e. fabrication of SLCW. The understanding of fabricating nanoporous polymer films, knowhow of liquid-core waveguides and the understanding of thiol-ene click chemistry is combined together to deliver much efficient SLCWs.

The current work utilizes UV lithography for the fabrication of hydrophilic microchannels in the nanoporous polymer. In a standard UV lithography process, a substrate is coated with a photoresist and an appropriate mask is used for making microstructures. In the present case, the photoresist is replaced with a thiol solution which is loaded into the nanoporous polymer. UV I-line (λ = 365 nm) is used for the excitation of thiol solution loaded nanoporous polymer sample; aligned with an appropriate UV mask. After adequate exposure time, the excess of thiol solution is washed out from the nanoporous polymer film, similar to a development step in UV photolithography. The grafted thiol molecule containing hydrophilic groups are clicked on to the nanoporous polymer in desired volume. The hydrophilic modified volume is filled with water to form a solid-liquid core surrounded by air-filled nanoporous polymer volume which acts as a clad. The process of SLCW fabrication is easy, clean and efficient. It is also compatible with existing cleanroom processes and can be readily adopted on the standard micro and nano lithography bench. The process is not selective towards the type of thiol system and the polymer in use, thus it can be used for different thiol-substrate combinations.

6.2 Waveguide Fabrication

The SLCW device Fabrication is done in 3 major steps: 1) Fabrication of nanoporous polymer film

2) Thiol-ene photochemical reaction

3) Post reaction washing and drying step

6.2.1 Fabrication of nanoporous polymer film

The nanoporous 1,2-PB film fabrication procedure is discussed in details previously (section 2.4). The method of fabrication remains unchanged but it is fine tuned to fulfill the requirements of the current process. The precursor *PB-b-PDMS* block copolymer solution is prepared in THF with

1mol% dicumyl peroxide used as a thermal cross-linker. The solvent casting is done on a flat 0.5 mm thick silicon substrate coated with a low surface energy fluorinated organosilane layer. The solution in this case is kept slightly more viscous to prevent the run away from the substrate during the solvent casting. After evaporation of the solvent from the wafer, another low surface energy silicon wafer is placed on top of it with aluminum spacers of desired thickness which is 200 μm in this case. The silicon wafer sandwich is pressed into a specially built pneumatic press shown in figure 6.1a. The press consists of a gas inlet and a vacuum port. Firstly nitrogen is circulated in the chamber, followed by a vacuum step. This cycle of nitrogen purging followed by vacuum is repeated 3 times to ensure absence oxygen during the compression step is being carried out. In a vacuum state, the silicon wafer sandwich is pressed at 4 bars. After 30 min of pressing the sandwich, it is placed in a cross-linking chamber (figure 6.1b) which is filled with nitrogen to rule out any trace of oxygen during the thermal cross-linking step. Thermal cross-linking is done at 140^{o} C for 100 min instead of 120 min (as described in section 2.4) to ensure sufficient amount of pendant double bonds available for the thiol-ene chemistry. The cross-linked polymer film is removed from the silicon wafer with relative ease due to its low surface energy coating. This film is chemically etched in TBAF for 5 h and washed in THF followed by methanol wash to completely remove etched PDMS, unreacted dicumyl peroxide and it's by products.

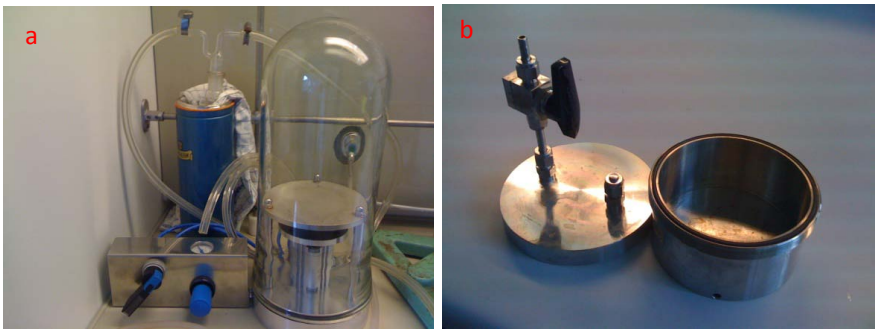

Figure 6.1. Cross-linking setup for 1,2-PB. a) Pneumatic press for the preparation of thin film, b) air tight cross-linking cylinder for carrying out thermal cross-linking at 140^{o} C in the nitrogen atmosphere.

6.2.2 Thiol-ene photochemical reaction

As discussed in the earlier chapter, MSA and MESNA (500 mM) are selected thiol molecules for photo grafting reaction. The thiol solution loading into the nanoporous polymer is done in yellow light (λ > 500 nm) or in the dark room. This is to prevent an uncontrolled reaction of thiol molecules with the 1,2-PB pendant double bonds as shown in figure 6.2. It depicts FT-IR spectra of an modified nanoporous polymer and MSA loaded nanoporous sample. The loading in done in normal light (no dark room or yellow light) and the sample is washed without actual UV exposure.

After washing in ethanol as per the standard protocol and drying step, FT-IR spectra are recorded. The spectra shows an evolved carbonyl stretch at 1720 cm^{-1} and disappearance of vinyl unsaturation peak at 904 cm^{-1} confirming the uncontrolled reaction of thiol with the PB pendant double bonds. Thiol solution is also prepared freshly for each exposure cycle as the thiol solution has a limited shelf life[12]. The stored thiol solution has not been as effective as the freshly prepared solution.

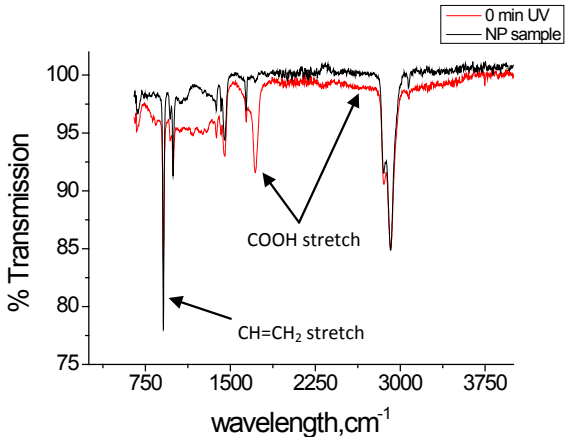

Figure 6.2. FT-IR spectra of an unmodified and MSA loaded nanoporous polymer is compared. The nanoporous polymer sample loaded with thiol in normal light (without UV exposure) is washed as per the standard protocol. The sample shows newly developed carboxylic acid peak at 1710 cm^{-1} and reduction of vinyl unsaturation at 904 cm^{-1} indicating uncontrolled modification of the nanoporous polymer interface.

Thiol solution loaded nanoporous polymer films are aligned with the photolithographic mask and placed on an oxidized aluminum chuck. Figure 6.3a shows the aluminum chuck with a black (anti-reflecting) surface beneath the polymer. It is essential for preventing an over exposure of the polymer from beneath. The UV light passing through polymer film reflects back from the surface beneath and enters back into the thiol solution loaded polymer. This triggers the uncontrolled hydrophilization in the areas covered under mask as shown in figure 6.3b. The translucent parts of the sample represent partial water filling in the nanopores as a result of over exposure in the region ideally covered under the mask.

The nanoporous polymer sample aligned with photo lithographic mask is placed on the aluminum chuck with excess of thiol solution around the polymer, under the mask. This way crystallization of powdered thiol and photoinitiator in the nanopores is avoided. For the thiol photoreaction to

occur it is essential to have mobility of the thiol and photoinitiator molecules. The reaction in liquid phase facilitates effective diffusion of thiols and it also avoids possible light scattering due to crystallized thiol and photoinitiator in the nanopores. In case of MESNA no excess of solution is needed due to very short exposure times. The chuck in placed in a closed polycarbonate chamber and placed under the UV lens. The chamber facilitates easy handling of the chuck between different work stations containing odorous thiol solution inside. Reaction is carried out at 22±1^{o} C in air for 30 min in case of MSA and 4 min in case of MESNA.

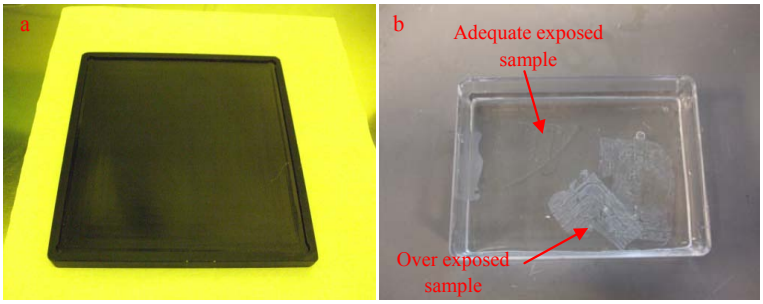

Figure 6.3. a) Oxidized aluminum chuck housing UV mask and polymer sample (not shown). The oxidized black surface avoids over exposure of the sample resulted from back scattering, b) over exposed and adequately exposed SLCW devices in water.

6.2.3 Post reaction washing and drying step

Post UV irradiation, modified samples are ultrasonicated for 1 h in their respective solvents, followed by 30 min washing in THF. The washing step is also performed in the yellow or dark room since there is still a possibility of the uncontrolled reaction in the region covered under mask. After adequate washing, the samples are vacuum dried for further waveguiding experiment.

6.3 Contrast curve for MSA and MESNA

Contrast curve for a photoresist is generated to study evolvement of the height of structures with respect to its UV irradiation time. In our case, the thiol-ene reaction results in hydrophilization of the nanoporous interface. The study of hydrophilization with respect to time will provide important data on how quick is the transition from no water uptake (hydrophobic) to considerable water uptake (hydrophilic) which is similar to a contrast curve. This way we can predict the suitability of thiol-ene based reactions for photolithographic patterning. Hydrophilization process for contrast curve experiment is same as the above mentioned procedure, only difference being usage of a transparent mask instead of a mask with microchannels. Resulting Water uptake by nanoporous polymer is plotted against the UV exposure time.

The result shows no significant water uptake for MSA system from 0-4 min. It registers a water mass uptake of 82 % of available theoretical porosity between 4 to 5 min. The hydrophilic jump occurs in the span of 1 min indicating a sharp nature of the contrast curve. The water uptake further increases and reaches up to the value of 100 % after 30 min and flattens out from there until 60 min of UV irradiation within the experimental accuracy. In the case of MESNA, the hydrophilic transition takes place from 0-91 % within 60 s of UV irradiation. It reports 100 % water uptake in 4 min and further flattening of the contrast curve, similar to MSA system. In both MSA and MESNA, the saturation water uptake value is in agreement with the theoretically calculated porosity for the polymer, indicating complete hydrophilization of the nanopores. MESNA system reaches the saturation water uptake much faster (by almost 6 times faster) than MSA system. This could be a result of steric hindrance of the thiol molecules as discussed in the section 5.3.2. The steric hindrance also results in formation of high overall number of thiol groups per nm^2 for MESNA (1.8) than the MSA (1.4) system.

6.4 Optical characterization

The current section summarizes propagation loss results on the thiol-ene modified SLCW devices. The experimental work is conducted in collaboration with Nimi Gopalakrishnan and Mads B. Christiansen from DTU Nanotech. The propagation loss is characterized using cutback technique, similar to the case of UV photo-oxidation. Cross section of the waveguides is $100\ \mu m \times 100\ \mu m$ and the total length of different waveguides, each having 90^o bend is between 4 to 32 mm. The set-up used in case of thiol-ene for loss measurement is modified compared to UV photo-oxidation setup. The SLCW device is placed between two 100 μm low refractive index (1.38) fluorinated ethylene propylene sheets which work as a clad and support for the devices. This sandwich is placed between 5 mm thick polycarbonate sheets. Upon clamping this assembly, it serves ease of handling and aligning of the device with input and output fiber. It also reduces the rate of water evaporation from the waveguides. The fluorinated ethylene propylene sheets reduce liquid core-clad mismatch, which improves guiding characteristic of the device. A He-Ne laser beam (632.8 nm) is coupled into the waveguides via multimode optical fiber and on the output port, a photodiode is connected by similar multimode optical fiber for recording the amount of light being guided. Propagation loss (in dB) in the straight portions of the waveguide is reported to be 0.26±0.01 dB/mm with coupling loss of 2.5±0.2 for MSA system and propagation loss of 0.54±0.03 dB/mm with coupling loss of 2.5±0.5 for MESNA system. Recent work carried out by our project students[100] further investigated the optimization of UV irradiation time for fabricating low propagation loss waveguides. They measured propagation loss of different SLCW devices as a function of UV irradiation time. The lowest propagation loss of 0.14±0.03 dB/mm is reported at

the exposure time of 40 min for MSA system. Lower loss value can be due to the better control over thiol-ene reaction which produces sharper waveguide boundaries, reducing overall surface scattering contribution.

6.5 Discussion

The results show that the thiol-ene approach is easy, efficient, more controlled, cleanroom compatible and it can be adopted with different thiol systems depending upon the requirements. The method cuts down the processing time for hydrophilization from 24 h (for photo-oxidation) to 5-40 min with the current thiol systems. The huge surface area facilitates up to 13 wt% thiol binding on polymer-air interface, which indicates a very high degree of surface modification. The sharp transition (high contrast) for both thiol systems allows better edge definition of lithographic structures. The process of hydrophilization is happening homogeneously across the entire cross section. These observations are reflected in the results when propagation loss values are measured. The hypothesis for obtaining better light guiding characteristics compared to photo-oxidation approach is as follows:

- UV source- collimated source can obtain better edge definition
- Well defined cross section of the waveguides for the entire depth of polymer film- consequence of high wavelength of light (365 nm) and thinner polymer films than in the case of photo-oxidation
- Shorter reaction times result in better defined edges/boundaries of waveguides instead of in diffused boundaries typical of very long reaction times
- Selectivity of thiol grafting and right choice of solvent result in effective modification strictly of the polymer-air interface resulting in better edge definition
- Better setup of SLCW devices between fluorinated ethylene propylene sheets reducing index mismatch also enhances light guiding ability of the devices

Photo-oxidation reaction results in uncontrolled side reactions producing many photo-products which tend to absorb in the blue region of visible light spectrum. This puts limitations on the selection of wavelength for guiding the light. The above mentioned advantages of thiol-ene approach result in fabrication of the devices which are capable of guiding light in entire spectrum of visible light. This imparts greater degree of flexibility for testing different aqueous systems or core component. Thiol-ene also has an added advantage that it can have a desirable functional group projecting out in the nanopore which can serve as a favorable starting point of further chemistry beneficial for sensing applications. The applicability of thiol-ene modified SLCW devices into biochemical sensing applications is treated separately in Annex I.

7. Conclusion and Outlook

7.1 Conclusion

The main objective of the current PhD was to fabricate a new class of solid-liquid core waveguide based on nanoporous polymers. Polybutadiene-*b*-polydimethylsiloxane (PB-*b*-PDMS) block copolymer was used as a precursor for making ordered nanoporous scaffolds. The volume porosity generated in the polybutadiene polymer was about 44%. This lowered the effective refractive index of the nanoporous polymer to 1.26, compared to the higher refractive index of 1.46 of the original block copolymer. For solid-liquid core waveguide application, the polymer needed to be hydrophilic in certain volume regions of the polymer. The nanoporous polymer was intrinsically hydrophobic in nature, which required surface modification of the polymer-air interface to induce the needed hydrophilicity. This was carried out with 2 different approaches: photo-oxidation of 1,2-polybutadiene and thiol-ene photochemistry. Both the approaches used UV irradiation in the presence of photolithographic masks to realize a patterned hydrophilization of nanoporous polymer. The water filled volume of the polymer constituted as a liquid (water)-solid (porous polymer) core surrounded by hydrophobic clad (air filled nanoporous volume) to facilitate light guiding, at the conditions of total internal reflection. The polymer-air surface functionalization was an important step in fabricating solid-liquid core waveguides. The major scientific contribution of the current work has come from these surface functionalization techniques i.e. photo-oxidation and thiol-ene click chemistry.

Photo-oxidation of nanoporous 1,2-polybutadiene was carried out by irradiating the sample with UV at 300- 400 nm wavelength in the presence of air for 24 h. UV irradiation of the sample was done from one side. The original polymer had limited absorption above 350 nm. At the same time, the permittivity of oxygen in the nanopores was very high. Both these facts resulted in the formation of oxygen containing photo products along the whole depth of the sample. The photo-oxidation process was characterized by gravimetry, titrimetry, FT-IR, solid-state NMR and energy dispersive X-ray (EDX) in SEM. Gravimetry was used to study the amount total oxygen fixed and the overall distribution of hydrophilic groups in the sample. Titrimetry also gave an independent way of finding out the overall distribution of the hydrophilic groups in the sample. It also helped to explain the distribution of photo-products relative to the air-polymer interface in the polymer matrix. FT-IR and solid-state NMR were used to analyze the chemical nature of the photo-products formed after reaction. The solid-state NMR revealed quantitative aspects of oxygen distribution amongst various photo-products. Finally EDX in SEM was used to study the degree of heterogeneity of the photo-oxidation reaction along the thickness of the sample.

^{13}C solid-state NMR showed the presence of 43 % carboxylic groups, 24% hydroxyl groups, 23% ether groups and 10% of saturated ketones in the photo-oxidized sample. The analysis showed absence of aldehydes and unsaturated ketone groups in photo products. Gravimetric analysis showed that 57% of the total oxygen was present in the form of carboxylic groups. This was in agreement with the % of oxygen in the form of carboxylic groups estimated by ^{13}C solid-state NMR. The average concentration of carboxylic groups by gravimetry and titrimetry was estimated to 5.4±0.7 and 5.5±0.9 groups per nm^2 respectively. The majority of carboxylic groups (93%) were located at the air-polymer interface (within 0.5 nm thickness) with 7% of the groups away from the interface into PB matrix. The degree of homogeneity of photo-oxidation reaction along the sample thickness was mapped by EDX in SEM and FTIR measurements done at multiple places on the same cross-section. For a 500 microns sample, it showed higher concentration of carboxylic groups in the first 100 microns of the sample which was droped by a factor of 4 and remains unchanged for the remaining 400 microns of the thickness. The nanoporous nature of the polymer allowed us to predict some of the vital information related to surface chemistry like nature, distribution and abundance of various photo products by combination of straightforward analysis techniques like FTIR, gravimetry, and titrimetry. Solid-liquid core waveguides were fabricated by photo-oxidation of nanoporous polymer using appropriate UV lithography masks. We reported a propagation loss of 0.62±0.03 dB/mm and a bend loss of 0.81 dB/90^o bend at 632.8 nm for the waveguides fabricated by this approach.

The second approach of polymer-air interface functionalization was by UV assisted thiol-ene click reaction. Thiol-ene click reactions were popular in the field of synthetic chemistry due to high efficiency, quantitative nature and not stringent reaction conditions. There was a variety of commercially available thiol molecules containing hydrophilic functional groups. In the current work, mercaptosuccinic acid (MSA) and sodium mercaptoethanesulfonate (MESNA) were the two hydrophilic molecules used for surface modification along with 2,2-dimethoxy 2-phenyl acetophenone (DMPA) used as a photoinitiator. MSA and MESNA with two carboxylic acid groups and a sodium sulfonate salt group respectively were the hydrophilic groups in the chosen thiol molecules. The thiol solution was loaded in the nanopores of a polymer and the reaction was carried out at 365 nm in excess of the thiol solution to prevent crystallization of thiol or photo-initiator during the reaction. The hydrophilic modification of the polymer was confirmed using FTIR and static contact angle measurements. The quantum yield for MSA and MESNA system was calculated to 21 and 76 respectively. The relatively high quantum yield numbers for both the reactions indicate the chain-like nature of the thiol-ene reaction. The higher quantum yield of MESNA system was due to the less steric hindrance around a primary thiol molecule against the

secondary thiol molecule in case of MSA. The FTIR data at different depths showed homogeneous surface modification for the entire thickness of 200 μm. This observation was in agreement with the conclusion derived from the water uptake curves. UV-Vis spectroscopy indicated no absorption of light above 350 nm wavelength range after photo-modification which was very important for the opto-fluidic applications. This allowed the light guiding in blue and green region which was not possible for the waveguides prepared with the photo-oxidation.

The knowledge of thiol-ene based hydrophilization was utilized for the fabrication of solid-liquid core waveguides. High surface area of the polymer allowed photo-grafting of thiol molecules up to 13 wt%. The overall surface density of the thiol groups was 1.4-1.8 groups per nm^2. The reaction time for complete hydrophilization was found to be 5-30 min. This was considerably improved compared to the previous approach of surface modification based on photo-oxidation, where the reaction time was 24 h. The contrast curve showed sharp transition, from almost no water uptake to uptakes of 80 & 90% of the available porosity for MSA and MESNA system respectively. This behavior was in agreement with simultaneous surface modification throughout the sample thickness. Optical characterization of the well defined patterns showed propagation loss values of 0.24±0.01 dB/mm for MSA system and 0.54±0.03 dB/mm for MESNA system, which were lower than in the case of photo-oxidation (0.62±.03 dB/mm). The MSA system was studied for further optimization and a propagation loss of 0.14±0.01 dB/mm was reported after 40 min of UV irradiation. The reduced propagation loss values for the optimized MSA system could be a result of more controlled chemical reaction resulting in sharp waveguide boundaries. MESNA system optimization for reduced losses was not performed in the present work.

In the current work, we have also made exploratory experiments with biosensing in a solid-liquid core waveguide. This type of biosensing is interesting especially for turbid analytes such as blood, milk etc, due to its filtering ability. The transparent serum part filters into the nanopores where an antibody fragment can form a conjugate with antigen contend from the serum. This capturing event can be monitored by a light guiding experiment. An anti-fluorescein/Oregon Green, rabbit IgG fraction, R-phycoerythrin Conjugate of 2μg/100μL was prepared in MilliQ water. The Fab fragment infiltration into the nanopores was verified by confocal microscopy. The Fab fragments adhered to the carboxylated waveguide channel walls due to adsorption caused by unspecific interactions. Further, capturing event in cuvette was demonstrated between the Fab fragments and its specific counterpart. However an actual implementation of capturing event in the waveguide showed marginal quenching of fluorescent signal from the fluorescein molecule. This could be due to the unspecific binding of fluorescein dye onto the nanoporous wall. An antifouling nanoporous

surface could avoid such unspecific binding of fluorescein molecule onto the nanoporous surface. The system is under optimization for better performance.

In conclusion, solid-liquid core waveguide was an innovative application of nanoporous polymers, which acts as a bridge between the area of polymer chemistry, microfabrication and optofluidics. The nanoporous interface functionalization with thiol-ene click reactions was an important step in producing solid-liquid core waveguides. The click reaction produced efficient and more controlled liquid core waveguide devices with very low propagation loss values. The nanoporous liquid core waveguide also showed great potential in the field of on chip chemical analysis, along with the possibilities of filtering and biosensing.

7.2. Future Work

The future work can be carried out in improving the existing material and extending existing materials applicability for different applications. The material improvement can be addressed by finding out alternate routes for synthesizing nanoporous polymers. The diblock copolymer system used in the current work was synthesized using anionic polymerization technique in our lab. Despite the high degree of control over polydispersity and molecular weight provided by this technique, it is a challenging route of polymer synthesis. It demands stringent reaction conditions and upscaling of polymer production can be very expensive. An alternative route for block copolymer synthesis can be using thiol-ene click chemistry. A multifunctional thiol with two or more thiol functionalities can be used with commercially available polymers, which acts as two different blocks to perform thiol-ene click reaction. Upon quantitative degradation of one of the polymer chain, nanoporosity can be induced in matrix polymer. This kind of induced nanoporosity is not expected to have a high structural regularity but it can retain percolation, lower index of refraction, and optical transparency needed for solid-liquid core waveguiding. Thus, it can be a much simplified approach of generating nanoporous polymers with less demanding reaction conditions.

Another improvement in the existing block copolymer system can be brought by reducing its brittleness. This can be done by performing hydrogenation of 1,4-PB. Hydrogenation reaction saturates the double bonds in the main chain which imparts more flexibility to the polymer chains. This phenomenon can be useful in saturating main chain unsaturated sites in 1,4-PB in the presence of suitable catalyst after desired degree of cross-linking. In this way we can impart more flexibility to the cross-linked polymer network, improving its loss mechanism.

The applicability of the current polymer system can be further extended in biosensing applications. It is clear from the exploratory experiments that, the nanoporous polymer needs an antifouling air-

polymer surface after binding the FAB molecules. This issue can be addressed by immobilizing short polyethylene glycol chains in the nanopores, which can reduce the unspecific binding of antigen molecules on the nanoporous wall. This way we can improve the signal to noise ratio from the capturing event between FAB and the antigen molecule.

Annex I: Biosensing in solid-liquid-core waveguides

1. Background

Tethering of biomolecules on the substrates is a popular practice in many applications of tissue engineering and biosensing. This is primarily due to the increasing need of developing point of care devices[101, 102]. For point of care, miniaturized lab-on-a-chip technology combines several aspects of the sensing and detection on the chip[103]. It requires immobilization of protein molecules on the biomaterial surface for cellular attachments. The biosensor technologies rely on capturing surface attached ligands for e.g. antibody-antigen interactions[104]. This is due to the fact that antibodies provide probes which are extremely specific towards binding of compatible antigen molecule[105]. The surface binding of sensing moieties is done by several routes such as photolithography, ion adhesion and chemical conjugation[106]. In general the surfaces are functionalized in order to attach biomolecules which will remain active by maintaining reorganization capability for targeted antigen.

Why nanoporous solid- liquid-core waveguide as a biosensor?

In the recent times, electronic and optical methods are used to sense the direct interaction between an antibody and antigen[107]. An example is a two dimensional patterned proteins attached to the biomaterial surface by nonspecific interactions i.e. adsorption or by covalent attachment to the surface. Also there are chemically modified antibodies with polymer chains, which are anchored to the polymeric surface[105, 106]. If we think about using a nanoporous polymer, it provides a huge internal surface available for binding of biomolecules. The high number of available binding sites per unit area can be translated into better signal strength of capturing event (antigen-antibody) by optical means. In other words, the sensitivity of the detection system can be improved.

Secondly, liquid-core waveguiding in a biosensor will ensure better light guiding to the detector. State-of-the art biosensor uses optical sensing techniques i.e. UV-Vis, NIR, which records capturing event and sends the optical signal to the decoding units. In the present case, the microchannel can used for hosting capturing event and later guiding the signal to the decoding unit with very minimal losses. An added advantage of this system is an inbuilt filtering ability of the polymer[68]. Due to its nanoporous nature, particles above 20 nm cannot infiltrate in the liquid core volume. This way we can use turbid analytes like blood or milk directly for sensing avoiding an intermediate step of centrifugation.

2. Fragment antigen-binding

Schematic diagram of an IgG antibody is shown in figure 1. The antibody is a large Y-shaped protein molecule and it is divided into 2 parts: upper part is called fragment antigen-binding (Fab fragment) while the bottom part is Fc region. The Fab fragment is a probe of an antibody which binds to the antigen. In the Fab region, free end of the chains carries an antigen binding site known as paratop. The other end of the chains is connected to Fc region with a hinge. This hinge can be cleaved by papain enzymatic reaction to obtain Fab fragment through different extraction mechanisms. The nanoporous polymer does not allow the diffusion of an entire antibody into the nanopores due to size constraints. Therefore, it is a requirement for the current system to make use

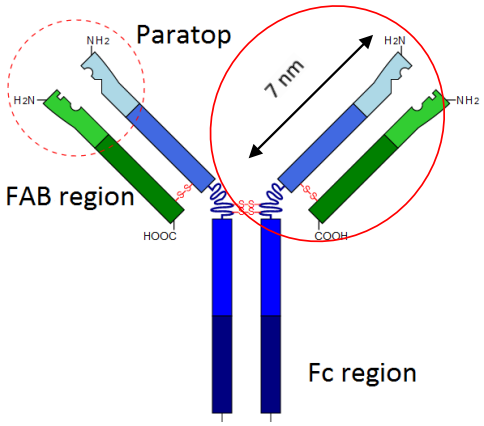

Figure 1. Schematic illustration of an antibody showing Fc and Fab fragments along with a paratope responsible for specific binding of an antigen to the antibody.

of the Fab fragments. Literature value reported length of a typical Fab fragment of about 7 nm with paratop size of about 2.5 nm[108]. In the present work we use anti-fluorescein⁄Oregon Green, rabbit IgG fraction, R-phycoerythrin Conjugate (labeled with fluorescent dye) and anti-fluorescein⁄Oregon Green, rabbit IgG Fab fragment. Both Fab fragments are specific to oregon green or fluorescein dye molecule and upon capturing event, they extinguish the fluorescence effect of the dye.

3. Concept of biosensing in SLCW

Schematic diagram of biosensing in SLCW is shown in figure 2. It represents a nanopore cross-section. The nanopore wall is functionalized with thiol molecules to render hydrophilicity in the polymer. In the process, it forms high surface density of thiol groups which can be equated to a thin layer of MSA being formed on the interfacial surface. This provides carboxylic acid groups

directed towards incoming Fab fragments immobilized in the nanopores. Due to adsorption driven by nonspecific binding between Fab and COOH groups, Fab fragments are expected to adhere on the nanoporous wall. This can provide ample of Fab sensing sites antigen containing analyte filled inside the nanopores. Upon capturing event (Fab-antigen), the aqueous core will be used as a waveguide for the detection of complex formation by absorption measurement.

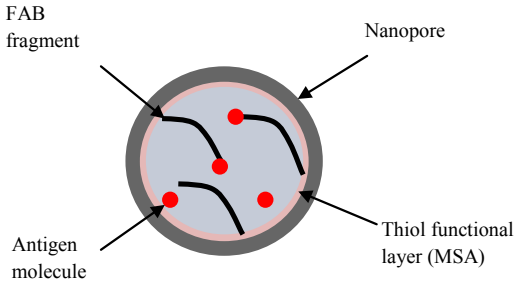

Figure 2.Schematic drawing of concept of biosensing in a SLCW. The thiol modified nanopores interface hosts functional groups which attaches to Fab fragments by unspecific binding. Antigen containing analyte can attach specifically to the Fab fragment and capturing event can be characterized by absorbance measurement by light guiding.

4. Results and discussions

It is important to demonstrate the following events in order to prove the biosensing in SLCW: 1) Fab presence in the nanopores, 2) demonstration of capturing event (Fab-antigen complex), and 3) demonstration of the capturing event in the SLCW. This work is performed in collaboration with the project partners, Peter Thomsen and Mads Christiansen.

Solution of anti-fluorescein/Oregon Green rabbit IgG fraction, R-phycoerythrin Conjugate of concentration of 2µg/100µL is prepared in MilliQ water. This solution is immobilized into the hydrophilic region of the nanoporous polymer. The solution droplet is placed on one end of the waveguide and filled in the microchannel by micro-capillary forces. Upon drying, the device is characterized by fluorescent confocal microscopy. Figure3 exemplifies MSA modified hydrophilic microchannel (100 µm wide) fabricated with the procedure described in chapter 6. Figure 3a shows results of fluorescent microscopy images (images at different levels are superimposed to obtain a single image) of hydrophilic channel in nanoporous polymer without Fab fragments. The measurement is done to verify the absence of auto-fluorescent signal from the functionalized surface nanoporous surface. Figure 3b illustrates cross-section of the carboxylated microchannel with strong fluorescent signal from phycoerythin labeled Fab fragment. The Fab fragments tend to adsorb on the carboxylated nanoporous wall, giving a strong signal from the microchannels

boundaries. It is also evident that excess of Fab fragments are collected in the center of the channel, possibly due to the evaporation of water from the edges.

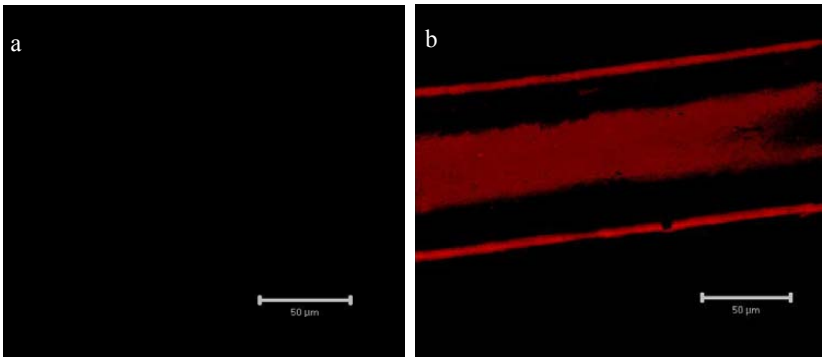

Figure 3. Fluorescent microscopic images of a) hydrophilic microchannel without Fab fragments, showing absence of auto-fluorescence, b) microchannel with the presence of Fab fragments. The Fab fragments adsorbs on the microchannel wall and excess of Fab fragments tend to gather in the center of the channel possibly due to evaporation of water from the edges.

Figure 4 shows a 3D profile obtained by confocal microscopy of the same microchannel, which is exposed to fluorescent tagged Fab fragment. X and Y axis numbers are representing pixels and should not be confused with actual length scale units. Vertical axis represents the intensity of the signal coming from the Fab fragment. The results clearly prove the presence of the adsorbed Fab fragments in the microchannel.

After successful demonstration of Fabs presence in the nanopores, the next step is to demonstrate the capturing event between Fab fragments and fluorescein dye. This experiment is performed in a quartz cuvette to realize the required concentrations of Fabs to fluorescein. The fluorescein excitation curve shows broad distribution starting from 400 nm to 525 nm, with maxima at 494 nm. The emission spectrum ranges between 475-650 nm with maxima at 521 nm. The excitation of fluorescein is performed with a blue laser at 448 nm and the resultant emission is recorded in the green region at 550 nm. The results are shown in figure 5.

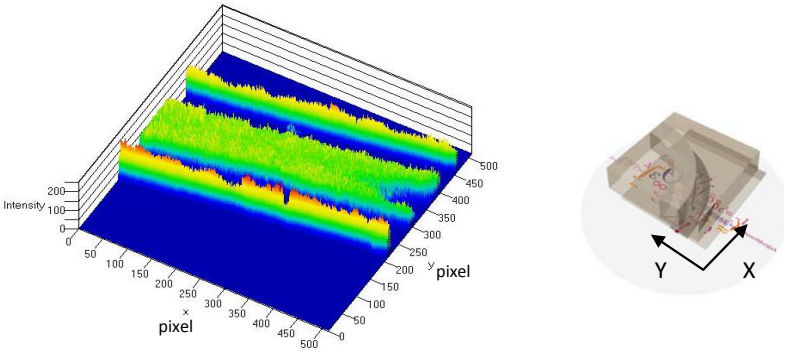

Figure 4.Confocal microscopic analysis of hydrophilic microchannel showing the presence of phycoerythrine labeled Fabs. The units shown on both axis represents pixels. Relation between these pixels and actual length units is not defined here.

Initially a fluorescein emission spectrum in the cuvette is recorded by a spectrometer probe placed at 90^{o} to the laser light. The Fab solution is added drop wise into the fluorescein solution and upon proper mixing, laser is coupled into the cuvette and fluorescence signal is collected as shown in figure 5.

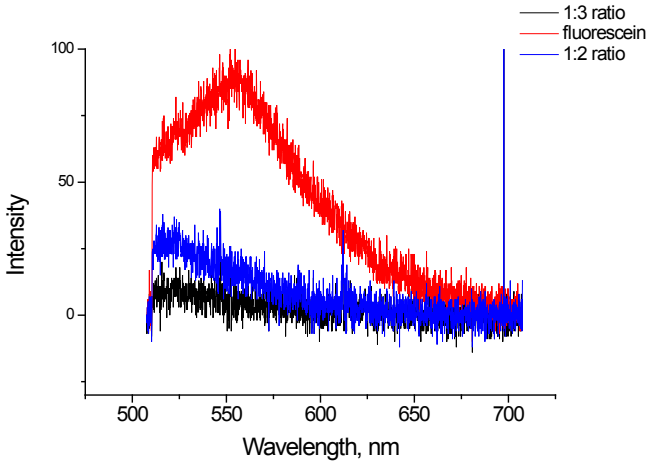

Figure 5. Cuvette measurement of capturing event between Fab and fluorescein dye molecule. The figure illustrates fluorescein emission signal being quenched upon addition of Fab aqueous solution. At 1:3 proportion of fluorescein to Fab by mass results in extinction of fluorescein emission signal.

The red line in figure 5 represents a fluorescent spectrum of 1 µg/100 µl fluorescein in MilliQ water. This intensity is reduced by adding Fab solution of 2 µg/100 µl in MilliQ water and at 3

µg/100 µl of Fab concentration, the fluorescence is found to be almost quenched. The scattering of the 448 nm light is avoided due to the relatively low concentration of the Fab solution and the size of the Fab molecules. This is later confirmed by conducting a UV-vis spectroscopy measurement of the Fab solution. The reduced fluorescence signal can be due to the capturing event in the cuvette.

After illustrating capturing step in a cuvette, the final step is to demonstrate the same results in a SLCW. A non-skin layered nanoporous polymer is used for fabricating SLCW which facilitates the diffusion of aqueous solutions from top. Much reduced diffusion path length of 200 µm (the sample thickness) is conducive for filling of entire microchannel with fab and dye solutions. The nanoporous device is clamped in a holder from 1 end in such a way that, the entire waveguide is projecting outside of the holder. Fluorescein dye solution in above mentioned concentration is added in drops on the waveguide from top which will instantly fill the waveguide region and thus guide the blue light. After careful alignment of the device, fluorescent intensity of the dye within the waveguide is recorded by a spectrometer as shown in figure 6. In the next step, the device is completely dried, at the same position, without disturbing the alignment. Upon drying, the channel stopped light guiding. That is when the Fab solution is added drop wise on the same waveguide. This results in wetting of the microchannel and guiding of the light once again. The fluorescent spectra is recorded again and compared to the previously obtained spectra. This type of experimental setup allows us for a direct comparison of the data obtained. Figure 6 shows the addition of the Fab solution, there is no considerable quenching of the original fluorescent signal. This can be primarily due to the unspecific adsorption of dye molecules on the nanoporous interface. In order to obtain an improved performance, an anti-fouling nanoporous interface is required which will prevent such antigen or fluorescein dye unspecific binding events into the nanopores.

The exploratory experiment on the biosensing in SLCW shows promising trend. It still demands considerable work to create anti-fouling nanoporous interface for obtaining improved sensing ability of the system. Thus, the proposed application opens up exciting applications for the nanoporous polymers.

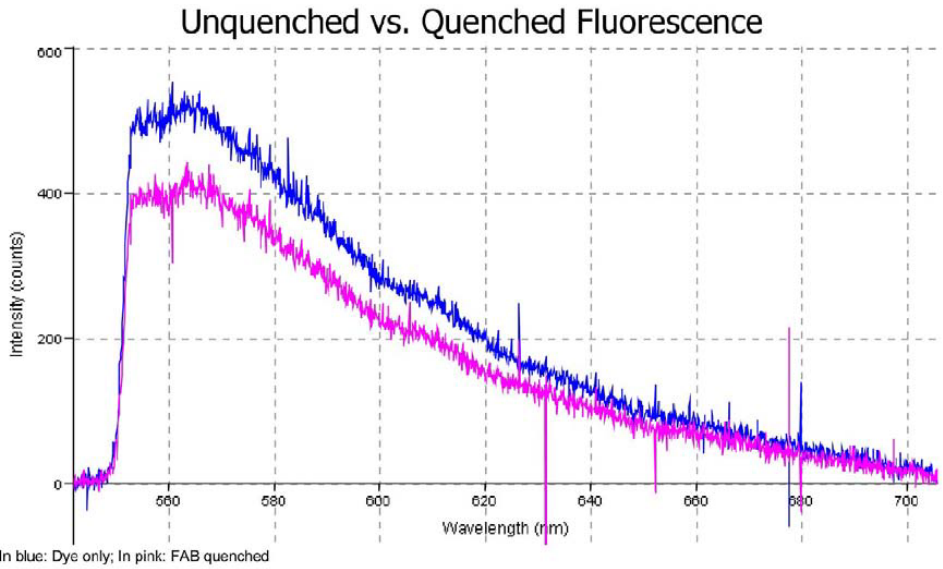

Figure 6.Capturing event of fluorescein in a SLCW showing partial quenching of the dye signal.

References

1. Schmidt, H.; Hawkins, A. R., *Microfluidics and Nanofluidics* **2008,** *4* (1-2), 3-16.

2. Manor, R.; Datta, A.; Ahmad, I.; Holtz, M.; Gangopadhyay, S.; Dallas, T., *Ieee Sensors Journal* **2003,** *3* (6), 687-692.

3. Li, J. Z.; Dasgupta, P. K.; Genfa, Z., *Talanta* **1999,** *50* (3), 617-623.

4. Dress, P.; Belz, M.; Klein, K. F.; Grattan, K. T. V.; Franke, H., *Sensors and Actuators B-Chemical* **1998,** *51* (1-3), 278-284.

5. Dijkstra, R. J.; Slooten, G. J.; Stortelder, A.; Buijs, J. B.; Ariese, F.; Brinkman, U. A. T.; Gooijer, G., *Journal of Chromatography A* **2001,** *918* (1), 25-36.

6. Ndoni, S.; Li, L.; Schulte, L.; Szewezykowski, P. P.; Hansen, T. W.; Guo, F. X.; Berg, R. H.; Vigild, M. E., *Macromolecules* **2009,** *42* (12), 3877-3880.

7. Li, L.; Schulte, L.; Clausen, L. D.; Hansen, K. M.; Jonsson, G. E.; Ndoni, S., *Acs Nano* **2011,** *5* (10), 7754-7766.

8. Keshtov, M. L.; Said-Galiev, E. E.; Abramchuk, S. S.; Khokhlov, A. R., *Doklady Physical Chemistry* **2011,** *437*, 68-71.

9. Yu, H. C.; Kumar, S. V.; Song, Y. K.; Choi, J.; Kudo, K.; Kim, J. G.; Oh, S. Y.; Chung, C. M., *Macromolecular Research* **2011,** *19* (12), 1272-1277.

10. Chen, L.; Yang, Y.; Guo, Z. Q.; Jiang, D. L., *Advanced Materials* **2011,** *23* (28), 3149-+.

11. Rabek, J., *Polymer photodegradation: mechanisms and experimental methods*. Chapman and Hall: London, 1995.

12. Hoyle, C. E.; Lee, T. Y.; Roper, T., *Journal of Polymer Science Part a-Polymer Chemistry* **2004,** *42* (21), 5301-5338.

13. Dress, P.; Franke, H., *Applied Physics B-Lasers and Optics* **1996,** *63* (1), 12-19.

14. Altkorn, R.; Koev, I.; VanDuyne, R. P.; Litorja, M., *Applied Optics* **1997,** *36* (34), 8992-8998.

15. Dasgupta, P. K.; Genfa, Z.; Poruthoor, S. K.; Caldwell, S.; Dong, S.; Liu, S. Y., *Analytical Chemistry* **1998,** *70* (22), 4661-4669.

16. Strobl, G., *The Physics of Polymers: Concepts for Understanding Their Structures and Behavior, chapter 3*. Springer: **1996**.

17. Fried, J., *Polymer science and technology*. Prentice Hall of India Private Limited: New delhi, **2000**.

18. Bates, F. S.; Fredrickson, G. H., *Annual Review of Physical Chemistry* **1990,** *41*, 525-557.

19. Bates, F. S.; Schulz, M. F.; Khandpur, A. K.; Forster, S.; Rosedale, J. H.; Almdal, K.; Mortensen, K., *Faraday Discussions* **1994,** *98*, 7-18.

20. Aero, E. L.; Vakulenko, S. A.; Vilesov, A. D., *Journal De Physique* **1990,** *51* (19), 2205-2226.

21. Lee, J. H.; Balsara, N. P.; Chakraborty, A. K.; Krishnamoorti, R.; Hammouda, B., *Macromolecules* **2002,** *35* (20), 7748-7757.

22. Castelletto, V.; Hamley, I. W., *Current Opinion in Solid State & Materials Science* **2004,** *8* (6), 426-438.

23. Bates, F., Polymer-Polymer Phase behavior. **1991**; Vol. 251, pp 898-905.

24. Thomas, E., Lescanec, L., *Phase morphology in block copolymer systems* Lond. A, 1994; Vol. 348, pp 149-166.

25. Matsen, M. W.; Bates, F. S., *Macromolecules* **1996,** *29* (23), 7641-7644.

26. Matsen, M. W.; Bates, F. S., *Macromolecules* **1996,** *29* (4), 1091-1098.

27. Vigild, M., Almdal, K., MOretensen, K., Ed. Macromolecules, **1998**; Vol. 31, pp 5702-5716.

28. Hajduk, D. A.; Harper, P. E.; Gruner, S. M.; Honeker, C. C.; Kim, G.; Thomas, E. L.; Fetters, L. J., *Macromolecules* **1994,** *27* (15), 4063-4075.

29. Forster, S.; Khandpur, A. K.; Zhao, J.; Bates, F. S.; Hamley, I. W.; Ryan, A. J.; Bras, W., *Macromolecules* **1994,** *27* (23), 6922-6935.

30. Stevens, M., *Polymer Chemistry: An Introduction*. Oxford university Press

31. Gomez, E. D.; Das, J.; Chakraborty, A. K.; Pople, J. A.; Balsara, N. P., *Macromolecules* **2006,** *39* (14), 4848-4859.

32. Schulte, L.; Grydgaard, A.; Jakobsen, M. R.; Szewczykowski, P. P.; Guo, F. X.; Vigild, M. E.; Berg, R. H.; Ndoni, S., *Polymer* **2011,** *52* (2), 422-429.

33. Szewczykowski, P. P.; Andersen, K.; Schulte, L.; Mortensen, K.; Vigild, M. E.; Ndoni, S., *Macromolecules* **2009,** *42* (15), 5636-5641.

34. Wu, K. W.; Hou, H. Y.; Shu, C. M., *Journal of Thermal Analysis and Calorimetry* **2006,** *83* (1), 41-44.

35. Masaki, K.; Ohkawara, S. I.; Hirano, T.; Seno, M.; Sato, T., *Journal of Polymer Science Part a-Polymer Chemistry* **2004,** *42* (17), 4437-4447.

36. Guo, F. X.; Andreasen, J. W.; Vigild, M. E.; Ndoni, S., *Macromolecules* **2007,** *40* (10), 3669-3675.

37. Ndoni, S.; Vigild, M. E.; Berg, R. H., *Journal of the American Chemical Society* **2003,** *125* (44), 13366-13367.

38. Hansen, M. S.; Vigild, M. E.; Berg, R. H.; Ndoni, S., *Polymer Bulletin* **2004,** *51* (5-6), 403-409.

39. Ndoni, S.; Jannasch, P.; Larsen, N. B.; Almdal, K., *Langmuir* **1999,** *15* (11), 3859-3865.

40. Halasa, A. Hydrogenated block copolymers of butadiene containing a block of 1,4 and a block of 1,2-microstructure. **1980**.

41. Pryke, A.; Blackwell, R. J.; McLeish, T. C. B.; Young, R. N., *Macromolecules* **2002,** *35* (2), 467-472.

42. Santin, C. K.; Jacobi, M. M.; Schuster, R. H.; Santoso, M., *Journal of Thermal Analysis and Calorimetry* **2010,** *101* (1), 273-279.

43. Monat, C.; Domachuk, P.; Eggleton, B. J., *Nature Photonics* **2007,** *1* (2), 106-114.

44. Okada, T., *Electrophoresis* **2007,** *28* (19), 3414-3419.

45. Dallas, T.; Dasgupta, P. K., *Trac-Trends in Analytical Chemistry* **2004,** *23* (5), 385-392.

46. Schueller, O. J. A.; Zhao, X. M.; Whitesides, G. M.; Smith, S. P.; Prentiss, M., *Advanced Materials* **1999,** *11* (1), 37-41.

47. Altkorn, R.; Koev, I.; Gottlieb, A., *Applied Spectroscopy* **1997,** *51* (10), 1554-1558.

48. Dress, P.; Franke, H., *Review of Scientific Instruments* **1997,** *68* (5), 2167-2171.

49. Dress, P.; Franke, H., An optical fiber with a liquid H2O core. *Integrated Optics and Microstructures Iii*, TabibAzar, M., Ed. **1996**; Vol. 2686, pp 157-163.

50. Stone, J., *Applied Physics Letters* **1972,** *20* (7), 239-&.

51. Schmidt, H., *Optical Guided-Wave Chemical and Biosensors II* **2010,** *8* (3), 195-219.

52. Risk, W., Kim, H., Miller, R., Temkin, H., Gangopadhyay, S., *Optics Express* **2004,** *12*, 6446-6455.

53. Wolfe, D. B.; Conroy, R. S.; Garstecki, P.; Mayers, B. T.; Vesenov, D. V.; Fischbach, M. A.; Paul, K. E.; Prentiss, M.; Whitesides, G. M.; Ieee, *Dynamic control of liquid-core/liquid-cladding optical waveguides*. **2005**; p 1680-1682.

54. Almeida, V. R.; Xu, Q. F.; Barrios, C. A.; Lipson, M., *Optics Letters* **2004,** *29* (11), 1209-1211.

55. Schwab, S. D.; McCreery, R. L., *Applied Spectroscopy* **1987,** *41* (1), 126-130.

56. Tsunoda, K.; Nomura, A.; Yamada, J.; Nishi, S., *Applied Spectroscopy* **1990,** *44* (1), 163-165.

57. Gilby, A.; Carson, W. Photometric apparatus with a flow cell coated with an amorphous fluoropolymer. **1993**.

58. Fujiwara, K.; Simeonsson, J. B.; Smith, B. W.; Winefordner, J. D., *Analytical Chemistry* **1988,** *60* (10), 1065-1068.

59. Hong, K.; Burgess, L. W. In *Liquid-Core Waveguides for Chemical Sensing*, Chemical, Biochemical, and Environmental Fiber Sensors VI Conference, San Diego, Ca, Jul 26-27; San Diego, Ca, **1994**; pp 71-79.

60. Korampally, V.; Mukherjee, S.; Hossain, M.; Manor, R.; Yun, M. S.; Gangopadhyay, K.; Polo-Parada, L.; Gangopadhyay, S., *Ieee Sensors Journal* **2009,** *9* (12), 1711-1718.

61. Wolf, K., Krotzsch, G., Ed. European Journal of Physics: **1995**; Vol. 16.

62. Snyder, A., *Optical Waveguide Theory*. 1st ed.; Chapman and Hall Ltd: London, **1983**.

63. Bundgaard, F. Prototyping of microfluidic systems with integrated waveguides in cyclic olefin copolymer (COC). Technical University of Denmark, Denmark, **2006**.

64. Smith, C. J. M.; Benisty, H.; Olivier, S.; Rattier, M.; Weisbuch, C.; Krauss, T. F.; De La Rue, R. M.; Houdre, R.; Oesterle, U., *Applied Physics Letters* **2000,** *77* (18), 2813-2815.

65. Sugimoto, Y., *Optics Express* **2004,** *12*, 1090-1096.

66. Yin, D., *Optics Express* **2005,** *13* (23), 9331-9336.

67. Gopalakrishnan, N., Sagar, K., Christiansen, M., Vigild, M., Ndoni, S., Kristensen, A., *Optics Express* **2010,** *18* (12), 12903-12908.

68. Gopalakrishnan, N., Christiansen, M., Kristensen, A., *submitted to Optics Express* **2011**.

69. Wiles, D. M.; Carlsson, D. J., *Polymer Degradation and Stability* **1980,** *3* (1), 61-72.

70. Adam, C.; Lacoste, J.; Lemaire, J., *Polymer Degradation and Stability* **1989,** *24* (3), 185-200.

71. Pecsok, R. L.; Shelton, J. R.; Koenig, J. L., *Polymer Degradation and Stability* **1981,** *3* (3), 161-176.

72. Piton, M.; Rivaton, A., *Polymer Degradation and Stability* **1996,** *53* (3), 343-359.

73. Adam, C.; Lacoste, J.; Lemaire, J., *Polymer Degradation and Stability* **1990,** *29* (3), 305-320.

74. Beavan, S., Phillips, D., *European Polymer Journal* **1974,** *10*, 593-603.

75. Rabek, J. F.; Lucki, J.; Ranby, B., *European Polymer Journal* **1979,** *15* (12), 1089-1100.

76. Depaoli, M. A., *European Polymer Journal* **1983,** *19* (9), 761-768.

77. Kagiya, V. T.; Takemoto, K., *Journal of Macromolecular Science-Chemistry* **1976,** *A 10* (5), 795-810.

78. Lucki, J., ranby, B., Rabek, J., *European Polymer Journal* **1979,** *15*, 1101-1110.

79. Dianbao, C., Guang, X., Xueming, T., *Chinese journal of polymer science* **1987,** *5* (1), 45-52.

80. Pavia, D., Lampman, G., Kriz, G., *Introduction to Spectroscopy*. Brooks/cole: Belmont, Ca.. **2009**; Vol. 4th edition.

81. Blanchard, D.; Shi, Q.; Boothroyd, C. B.; Vegge, T., *Journal of Physical Chemistry C* **2009,** *113* (31), 14059-14066.

82. Weber, H. P.; Dunn, F. A.; Leibolt, W. N., *Applied Optics* **1973,** *12* (4), 755-757.

83. Kolb, H. C.; Finn, M. G.; Sharpless, K. B., *Angewandte Chemie-International Edition* **2001,** *40* (11), 2004-+.

84. Lowe, A. B., *Polymer Chemistry* **2010,** *1* (1), 17-36.

85. Kade, M. J.; Burke, D. J.; Hawker, C. J., *Journal of Polymer Science Part a-Polymer Chemistry* **2010,** *48* (4), 743-750.

86. Kwisnek, L.; Nazarenko, S.; Hoyle, C. E., *Macromolecules* **2009,** *42* (18), 7031-7041.

87. Killops, K. L.; Campos, L. M.; Hawker, C. J., *Journal of the American Chemical Society* **2008,** *130* (15), 5062-5067.

88. Chan, J. W.; Hoyle, C. E.; Lowe, A. B.; Bowman, M., *Macromolecules* **2010,** *43* (15), 6381-6388.

89. Hoyle, C. E.; Bowman, C. N., *Angewandte Chemie-International Edition* **2010,** *49* (9), 1540-1573.

90. Cramer, N., Bowman, C., *Journal of Polymer Science: Part A: Polymer Chemistry* **2001,** *39*, 3311-3319.

91. Cramer, N. B.; Reddy, S. K.; O'Brien, A. K.; Bowman, C. N., *Macromolecules* **2003,** *36* (21), 7964-7969.

92. Reddy, S. K.; Cramer, N. B.; Bowman, C. N., *Macromolecules* **2006,** *39* (10), 3673-3680.

93. Cramer, N. B.; Davies, T.; O'Brien, A. K.; Bowman, C. N., *Macromolecules* **2003,** *36* (12), 4631-4636.

94. Roper, T., Kwee, T., Lee, T., Hoyle, C., *Polymer* **2004,** *45* (9), 2921-2929.

95. Pojman, J., Varisli, B., Perryman, A., Edwards, C., Hoyle, C., *Macromolecules* **2004,** *37*, 691-693.

96. Chiou, B. S.; English, R. J.; Khan, S. A., *Macromolecules* **1996,** *29* (16), 5368-5374.

97. Chiou, B. S.; Khan, S. A., *Macromolecules* **1997,** *30* (23), 7322-7328.

98. Chiou, B. S.; Raghavan, S. R.; Khan, S. K., *Macromolecules* **2001,** *34* (13), 4526-4533.

99. Bowman, c., Anseth, K., *Macromol symp* **1995,** *93*, 269-277.

100. Lorentzen, S., Frederiksen, G. *Liquid core waveguides*; Technical University of Denmark: DTU Nanotech, **2011**.

101. Sebra, R. P.; Masters, K. S.; Bowman, C. N.; Anseth, K. S., *Langmuir* **2005,** *21* (24), 10907-10911.

102. Blawas, A. S.; Reichert, W. M., *Biomaterials* **1998,** *19* (7-9), 595-609.

103. Stern, E.; Vacic, A.; Rajan, N. K.; Criscione, J. M.; Park, J.; Ilic, B. R.; Mooney, D. J.; Reed, M. A.; Fahmy, T. M., *Nature Nanotechnology* **2010,** *5* (2), 138-142.

104. Mooney, J. F.; Hunt, A. J.; McIntosh, J. R.; Liberko, C. A.; Walba, D. M.; Rogers, C. T., *Proceedings of the National Academy of Sciences of the United States of America* **1996,** *93* (22), 12287-12291.

105. Lowe, C., *Trends in biotechnology* **1984,** *2* (3), 59-65.

106. Higgins, I. J.; Lowe, C. R., *Philosophical Transactions of the Royal Society of London Series B-Biological Sciences* **1987,** *316* (1176), 3-11.

107. Berney, H.; Roseingrave, P.; Alderman, J.; Lane, W.; Collins, J. K., *Sensors and Actuators B-Chemical* **1997,** *44* (1-3), 341-349.

108. Werner, C., Bunting, J., Cathou, R., *Proc. Nat. Acad. Sci. USA* **1972,** *69* (4), 795-799.

Appendix A

Kaushal S. Sagar , Mads B. Christiansen, Sokol Ndoni, Type and Distribution of Chemical Groups from Controlled Photo-Oxidation of Gyroid Nanoporous 1,2-Polybutadiene, *Polymer Degradation and stability* **2011**, *96,* 1866-1873

Polymer Degradation and Stability 96 (2011) 1866–1873

Contents lists available at ScienceDirect

Polymer Degradation and Stability

journal homepage: www.elsevier.com/locate/polydegstab

Type and distribution of chemical groups from controlled photo-oxidation of gyroid nanoporous 1,2-polybutadiene

Kaushal S. Sagar [a], Mads B. Christiansen [b], Sokol Ndoni [b,*]

[a] Department of Chemical and Biochemical Engineering, Technical University of Denmark, DK-2800 Kgs. Lyngby, Denmark
[b] Department of Micro and Nanotechnology, Technical University of Denmark, DK-2800 Kgs. Lyngby, Denmark

ARTICLE INFO

Article history:
Received 13 April 2011
Received in revised form
17 June 2011
Accepted 8 July 2011
Available online 2 August 2011

Keywords:
Nanoporous
1,2-Polybutadiene
Photo-oxidation
Energy dispersive X-ray spectroscopy

ABSTRACT

Photo-oxidation of nanoporous polymers is little studied. The high UV penetration depth and high surface concentration in these materials give unprecedented possibilities both in fundamental work on surface photochemistry and in nanotechnological applications related for example to patterned hydrophilicity or refractive index. This is a quantitative study of the photo-oxidation products of nanoporous gyroid 1,2-polybutadiene in air. Irradiation of the porous sample with UV in the wavelength range of 300–400 nm enables tuning of the hydrophilicity of the nanoporous polymer through formation of hydrophilic chemical groups, carboxyl and hydroxyls, mainly onto the large air–polymer interface. The nature and abundance of the chemical groups induced by photo-oxidation is identified by solid-state ^{13}C-NMR and FTIR spectroscopy. The distribution of photo-oxidation groups, both relative to the nanometre-scale polymer–air interface, and as a function of irradiation depth in the sample, is studied by gravimetry, titrimetry, ATR-FTIR and energy dispersive X-ray spectroscopy in scanning electron microscopy.

1. Introduction

Polybutadienes are susceptible to photo-oxidation as a result of unsaturations present in the main chain or in the pendant groups of the polymer. In unsaturated and unconjugated organic compounds, lowest energy excited state transition (π, π^*) occurs at wavelengths λ below 300 nm [1]. However, polybutadiene and other synthetic materials undergo photo-oxidation by UV in the range 300 nm $< \lambda <$ 400 nm [1,2]. The present understanding of the reaction mechanism for the photo-oxidation of polydienes is based on the following reaction steps [3–10]:

- Different impurity chromophores in the matrix absorb light, forming excited states i.e. singlets, and from them triplets, which are longer living and with increased probability of reaction.
- Triplet state molecules cleave polymer chains by attacking tertiary or allylic hydrogen forming polymeric radicals which add molecular oxygen, generating peroxy radicals, thus initiating auto-catalytic propagation step by abstracting another tertiary proton and forming hydroperoxides.
- Hydroperoxide groups are highly photo-labile and thus get excited upon absorption of UV light or by energy transfer resulting in breakage of the O–O weak bond and formation of peroxy and hydroxy radicals. Further, accelerated oxidation occurs via chain scission, hydrogen abstraction etc.
- Alkoxy radicals may subtract an allylic proton resulting in an alcohol and another polymeric radical. Hydroxy radicals may also react with protons forming water molecules.
- Cross-linking is also observed during photo-oxidation due to reaction of alkoxy radicals with the unsaturations in the main chain or pendant groups, typically forming ether linkages.
- Carbonyl compounds are major photo products which are finally observed in the photo-oxidized polymer. The formation of carbonyl groups is often coupled with main polymer chain scission.
- Norrish type I and II reactions further may yield carboxylic acid groups [6–8].

The formation of hydroxyl (–OH), ether (R–O–R′), carbonyl (R–CO–R′) and carboxyl (R–CO–OH) groups (conjugated or not), is anticipated from the above short presentation of the photo-oxidation reaction.

* Corresponding author. Department of Micro and Nanotechnology, Technical University of Denmark, DTU-Nanotech, Build. 423, DK-2800 Kgs. Lyngby, Denmark. Tel.: +45 4525 8146; fax: +45 4588 7762.
E-mail address: sond@nanotech.dtu.dk (S. Ndoni).

0141-3910/$ – see front matter © 2011 Elsevier Ltd. All rights reserved.
doi:10.1016/j.polymdegradstab.2011.07.009

In the present work we study in detail the photo-oxidation of 500 μm thick samples of gyroid nanoporous cross-linked 1,2-polybutadiene. The surface modification throughout the sample is primarily taking place due to availability of oxygen in the nanopores and the large penetration depth of reactive photons. The formation of hydrophilic groups, like hydroxyl and carboxyl groups modifies the affinity of polymer towards aqueous solutions [11,12]. The nature and overall concentration of oxygen-containing groups is assessed by combining ^{13}C NMR, FTIR and gravimetry. We specifically investigate the distribution of carboxylic groups, both relative to the air–polymer interface and to the thickness of the sample. Routine laboratory techniques like gravimetry, titrimetry and FTIR provide a wealth of information about the photo-oxidation products and their distribution at the polymer–air interface. The high surface concentration in nanoporous polymers makes this possible. For the sake of illustration, the surface area enclosed within 1 μm depth of our mesoporous polymer is roughly 200 times larger than the outer surface. An approximate gain factor of 200 is expected for the ATR-FTIR signal (typical probing depth of 1 μm) from the nanoporous polymer relative to a non-porous polymer with same surface density of functional groups.

2. Experimental

2.1. Materials

The block copolymer was synthesized by following an already reported procedure [13–15]. Tetrahydrofuran (THF) (purity ≥ 99.9%, GC grade), methanol (purity ≥ 99.9%, HPLC grade) and TBAF (1.0 M in THF) were purchased from Sigma–Aldrich. Dicumyl peroxide was bought from Fluka (purity ≥ 97.0%, TLC grade). All other chemicals mentioned were used as received.

The preparation procedure for the nanoporous films can be found elsewhere [14,15]. In brief, nanoporous 1,2-polybutadiene with gyroid morphology was prepared from a 1,2-polybutadiene-*b*-polydimethylsiloxane (1,2-PB-*b*-PDMS) diblock copolymer precursor after cross-linking of the butadiene block and quantitative removal of the PDMS block. The number average molar mass of the block copolymer was 14,200 g mol^{-1}, of which 59% by mass was 1,2-PB. The polydispersity index as estimated by SEC and ^{1}H NMR was 1.04. The nanoporous sample was of gyroid morphology [2] with pore diameter of 14 ± 1 nm and surface area of 280 ± 40 m^2 g^{-1} as estimated by nitrogen adsorption. The films were made by solvent casting THF solutions of the block copolymer mixed with 1 mol % of the cross-linker dicumyl peroxide relative to the number of double bonds of the PB component. After THF evaporation under nitrogen, the films were cross-linked at 140 °C in nitrogen atmosphere for 2 h. The etching of the PDMS minority block was done by using 3:1 molar excess of tetrabutylammonium fluoride (TBAF) relative to Si–O bonds in PDMS. The etching step lasted for 36 h and was followed by cleaning in THF and methanol for a total of 16 h.

The photo-oxidation of nanoporous polymer was done in a 'photo-reactor' consisting of a set of Philips Cleo 25W RS UV lamps, for 24 h under continuous venting with air and maintained at 38 °C. The UV irradiation 'hits' the samples from the top side. The emission spectrum is in the wavelength range of 300–400 nm and is shown elsewhere [2].

2.2. Characterization techniques

IR spectra were recorded with a PerkinElmer Spectrum One ™ FTIR Spectrometer using an Attenuated Total Reflectance (ATR) measuring head with a resolution of 4 cm^{-1} and summation of 32 scans. ^{13}C NMR measurements were done on a 300 MHz, Varian Unity INOVA Solid-state NMR instrument at Roskilde University. A delay time of 15 s was used, to allow hydrogen deficient carbon signals like carboxylic acids, ketones etc to relax.

UV photo-oxidized samples were treated with NaOH dissolved in different solvents. NaOH treatment (staining) was used for mapping the distribution of carboxylic groups in the polymer as described in the 'Results and Discussion' section. The staining of samples was done by first preparing a 0.250 M solution of NaOH in MilliQ water, which was then diluted five times by volume in solvents like water, methanol and THF. The final mixture was used to probe the concentration of carboxylic groups in the photo-oxidized polymer at different depths relative to the air–polymer interface. Titration experiments were done using 0.100 M potassium hydrogen phthalate (PHP) in MilliQ water and NaOH solution in water and methanol. NaOH stained samples were removed after 8 h and washed in consecutive solvents on a shaker for 2 h and this solvent was added to the original solvent, which was then titrated with PHP.

Small-angle X-ray scattering (SAXS) data were acquired at Risø National Laboratory (Risø – DTU) using Cu Kα X-rays with a wavelength of 1.542 Å from a Rigaku rotating anode with the sample at a distance of 1435 mm from the 2-D position-sensitive wire detector. 1-D scattering plots of intensity versus length of scattering vector $q = 4\pi\lambda^{-1}\sin(\theta/2)$ were obtained by azimuthal integration of the 2-D data, where λ and θ are the X-ray wavelength and scattering angle, respectively. The SAXS patterns of both the pristine nanoporous samples and of the photo-oxidized samples were identical and consistent with the gyroid morphology [2].

Energy Dispersion X-ray spectroscopy (EDX) with Scanning Electron Microscopy (SEM) was performed on an Inspect S microscope from FEI at the Centre for Electron Nanoscopy, DTU-CEN. The EDX detector in SEM detects X-ray radiation generated by the microscope's electron gun, which was used for elemental analysis of the sample. The analysis was carried out under vacuum using an electron accelerating voltage of 5 kV.

3. Results and discussion

The UV–vis absorption spectrum of nanoporous 1,2-polybutadiene is shown by the dashed line in Fig. 1a. The penetration depth is the depth in the material at which intensity is reduced by a factor of *e* (Euler's number) relative to the intensity hitting the upper sample surface [16]; it's inversely proportional to the absorbance and is shown by the solid line in Fig. 1a. In the effective irradiation range of 300–400 nm, absorption markedly decreases, while penetration depth increases at increasing wavelength. Photoactive UV quanta penetrate deep into the polymer, which sets the platform for effective photo fixation of oxygen in the entire thickness of the sample. However the increasing penetration depth with decreasing photon energy is one of the causes of heterogeneous sample modification at different depths, as will be shown at the end of this section. It is important to note that the significant absorbance at $\lambda > 300$ nm cannot be explained by the expected material composition. A possible chemical composition, concentration and source for the alleged chromophore impurities mentioned in the introduction, with such a significant effect in the absorption spectrum is difficult to accept. The free radical cross-linking initiator dicumyl peroxide (DCP) could be the source of some kind of aromatic chromophore impurity. However substituting DCP with aliphatic initiators like diamyl peroxide or di *tert*-butyl peroxide did not produce any noticeable change in the UV–vis spectra [2]. The major contribution to the 'absorbance' is most probably scattering; preliminary results show that non-porous networks prepared by cross-linking 1,2-PB homopolymer by the same procedure as described above show very similar absorbance spectra. Such an observation hints at the 1,2-PB cross-linked network density fluctuations as the main source of scattering. Further investigation is

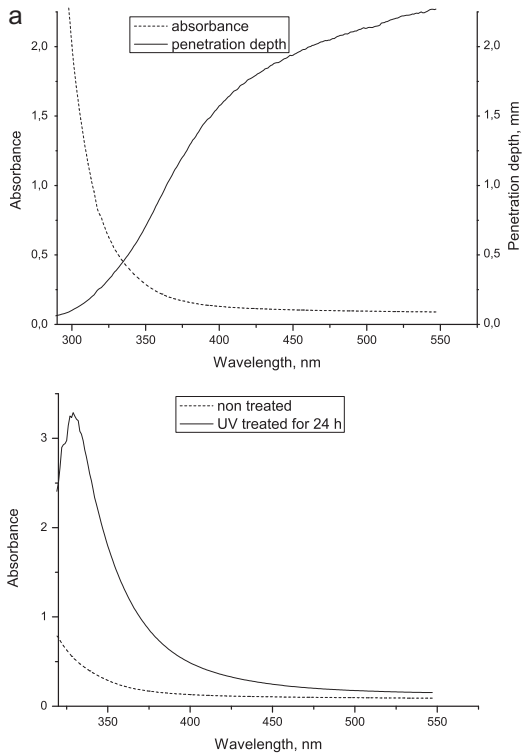

Fig. 1. UV–vis absorption spectra for nanoporous cross-linked 1,2-PB before and after photo-oxidation. (a) Absorption and penetration depth of UV radiation for a 500 μm thick sample. (b) Absorption of non-treated and 24 h UV treated sample.

currently being carried out and results will be reported elsewhere. After 24 h of exposure to UV the sample shows an increased absorption in the visible, mostly in the blue region, as clearly seen in Fig. 1b, which imparts to photo-oxidized samples a yellowish colour. The absorbance in the visible may be due to the formation of few highly conjugated carbonyl compounds with high extinction coefficient in the blue [4]. At the level of accuracy of the analyses presented here we have not been able to detect such groups. In the rest of the manuscript we discuss procedures and results of identification of the major photo-oxidation groups and their distribution, based on a variety of experimental techniques: FTIR, gravimetry, ^{13}C NMR, titrimetry and EDX-SEM.

3.1. Identification and quantification of oxygen-containing groups by FTIR, gravimetry and ^{13}C NMR

3.1.1. FTIR

Irradiation of nanoporous films under polychromatic UV for 24 h in presence of air leads to changes in IR spectra compared to the non-irradiated samples. New absorption bands develop in the range of 3100–3670 cm^{-1}, around 1710 cm^{-1} and a series of overlapping peaks in the region from 1500 to 650 cm^{-1}, as shown in Fig. 2. The peaks at 1200 cm^{-1} and 1100 cm^{-1} can be due to C–O bonds in aliphatic and vinyl ethers or alcohols. The broad peak centring at 3400 cm^{-1} can be attributed to alcoholic OH groups and the overlapping broad absorption extending down to 2500 cm^{-1} can be

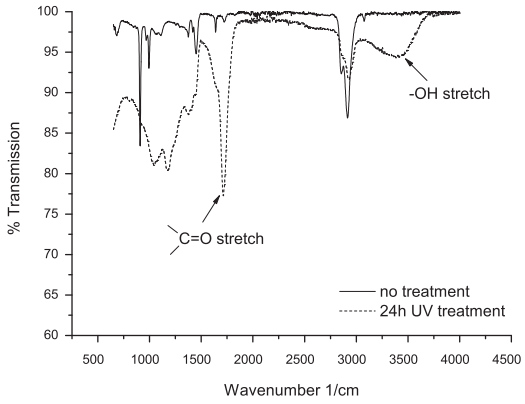

Fig. 2. FTIR spectra of non-irradiated and UV irradiated nanoporous polymer.

attributed to OH groups in carboxylic acids. The peak in the carbonyl region (1500–1710 cm^{-1}) can either be due to the presence of ketones, aldehydes or carboxylic acid compounds [4,5,17,18].

NaOH staining was done in order to discriminate carboxylic acids from the carbonyl compounds formed after photo-oxidation. It was also used for mapping the distribution of carboxylic groups relative to the pore surface and to the irradiation depth, as discussed in the following Sections 3.2 and 3.3. Fig. 3 shows IR spectra of a UV modified sample before and after treatment (staining) with NaOH. It is notable that most of the peak centring at 1720 cm^{-1} has been shifted to 1570 cm^{-1} (antisym. stretch) and 1380 cm^{-1} (sym. stretch) after the basic treatment. This peak shift is due to the conversion of carboxylic groups to sodium carboxylate salt. This in turn confirms that the majority of the carbonyl groups are actually carboxylic groups. In the following we consider the formation by photo-oxidation of ester groups as an event of negligible probability. Such groups, if hydrolyzed under the NaOH treatment, could also be a source of sodium carboxylate. The residual peak at about 1710 cm^{-1} in the NaOH treated sample must originate from either ketones or aldehydes. As will be shown shortly, ^{13}C NMR analyses favours saturated ketones as the best choice for the residual carbonyls and it's estimated to represent ~ 20% of the total carbonyls.

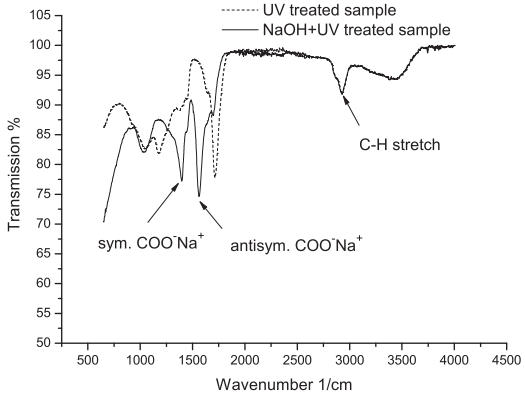

Fig. 3. FTIR spectra of UV irradiated and NaOH stained nanoporous polymer.

3.1.2. Gravimetry

Gravimetric analysis of samples before and after UV treatment and after NaOH staining give information on the total fixed oxygen and the fraction of oxygen fixed in the form of carboxylic groups. The sample mass increase after photo-oxidation provides the total amount of oxygen photochemically fixed in the polymer. Similarly, mass uptake from NaOH staining, after thorough removal of excess by rinsing and after drying gives the concentration of the counterion Na^+, which is equivalent to the moles of COOH groups in the polymer. The rest of oxygen might then appear in the form of other photo products like ethers, ketones, or alcohols. The fractional mass uptake relative to original nanoporous polymer after UV treatment and vacuum drying is in average 0.15, equivalent to 9.4 mmol of O, while the fractional mass uptake due to exchange of hydrogen with sodium is 0.055 (again relative to the original nanoporous polymer), equivalent to 2.5 mmol of COOH or 5.0 mmol of O. Therefore the fraction of oxygen in the form of carboxylic acid groups constitutes 53% of the total fixed oxygen. The NaOH staining here is done in water solution, which as explained later in the text addresses about 93% of the total COOH groups, the remaining 7% being 'buried' deeper inside the polymer matrix, at a concentration insufficient to allow water access (see discussion related to Table 2). This means that the actual amount of oxygen fixed in COOH groups might be 57% of the reacted oxygen, slightly higher than the figure mentioned above. In that case the remaining 43% of the total fixed oxygen would be part of other photochemical groups.

3.1.3. Solid-state ^{13}C NMR

Fig. 4 shows solid-state ^{13}C NMR spectra [17] of a nanoporous sample before and after UV irradiation, vertically shifted for the sake of clarity. The sample before photo-oxidation is essentially highly cross-linked 1,2-PB (with ~9% of monomers 1,4 connected). It shows two groups of peaks, the one centred at about 35 ppm assigned collectively to the saturated carbon atoms, and a group of peaks in the range 110–150 ppm assigned to the olefinic carbons. The number fraction of the two saturated and olefinic carbons are 0.86 and 0.14, as given in the first data row of Table 1. This is equivalent to 28% of the original double bonds in the precursor 1,2-PB-*b*-PDMS block copolymer surviving the cross-linking reaction, very well in line with the FTIR results (data not shown). Such a coincidence gives confidence that the recorded ^{13}C NMR spectra

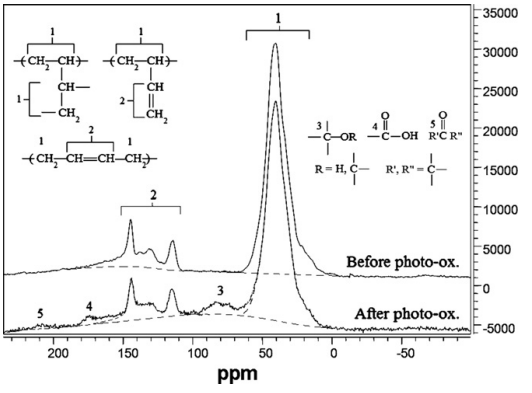

Fig. 4. Solid-state ^{13}C NMR spectra for unmodified and UV modified nanoporous polymer. The saturated carbons in the cross-linked 1,2-PB (containing ~9% 1,4-PB) are collectively labelled by 1, the olefinic C by 2, the C connected to oxygen by single bond (like in alcohols or ethers) by 3, the carboxylic C by 4 and the carbonyl C (in saturated ketones) by 5. The dashed lines show baselines and peak tailing settings that were used to estimate the concentrations (see Table 1).

Table 1
Fraction of carbons of different chemical bonding from ^{13}C NMR and oxygen partition among functional groups. The numbers in the first row are the labels of C groups given in Fig. 4.

Sample	C '1'	C '2'	C '3'	C '4'	C '5'
Before photo-ox.	0.86	0.14	0	0	0
After photo-ox.	0.76	0.13	0.062	0.038	0.010
'O' partition/%			33 (16 eth, 17 alc)	60	7

shown in Fig. 4 can provide quantitative information. In addition to the peaks observed for the original nanoporous sample, the oxidized sample shows a broad peak around 82 ppm assigned to carbon bound to oxygen by single bonds (ether or alcohol groups), another broad peak at 175 ppm, which we interpret as due to COOH groups and a weak peak at 210 ppm, most probably due to carbonyl carbon in saturated ketones. It is also evident that no peak can be discerned in the range of 185–200 ppm expected for aldehydes or α, β-unsaturated ketones. The mole fraction of the five groups of carbons as labelled in Fig. 4 that were found in the photo-oxidized sample are shown in the second data row of Table 1. The numbers were derived from the respective peak areas in Fig. 4. The data in Table 1 reveal a number of interesting features about the products of photo-oxidation:

- 89% of the Carbon atoms in the photo-oxidized sample remain aliphatic, while 11% bind to oxygen as ethers, alcohols, carboxylic acids and saturated ketones;
- The fraction of olefinic carbons '2' after photo-oxidation is only slightly lower than before (0.13 instead of 0.14), while the fraction of saturated carbons '1' falls to 0.76 from the original 0.86. With unchanged total number of carbon atoms in the two samples this indicates that most oxygen is fixed on originally saturated carbons, which indirectly supports the idea that tertiary or vinyl carbons are the most labile loci for photo-oxidation;
- 6% of the Carbons are bound to oxygen by single bonds like in ethers and alcohols (group '3'), and 5% as carbonyls (4% carboxylic groups, '4', and 1% saturated ketones, '5');
- The third data row in Table 1 lists an estimate of the partition of photo-fixed oxygen among the five possible chemical groups. 60% of the oxygen is in carboxylic acids, 33% in ethers or alcohols (at almost equal proportion), and 7% in saturated ketones. It is calculated from the number fraction of carbon in each group (2nd data row) recalling that the molar ratio of directly bond C:O is 2 for ethers, 1 for alcohols and ketones and 0.5 for carboxylic acids. An additional boundary condition is the already mentioned total amount of reacted oxygen per gram of nanoporous polymer (9.4 mmol g^{-1}).

In summary, solid-state ^{13}C NMR analysis provides qualitative and quantitative results about the nature and abundance of the chemical groups formed by photo-oxidation of the nanoporous cross-linked 1,2-PB. The hydrophilic groups formed by photo-oxidation are carboxylic acids (43% of the oxygen-containing groups binding 60% of the fixed oxygen), and alcohols (24% of the groups, 17% of the oxygen). Ethers count for 23% (16%) and saturated ketones for 10% (7%) of the groups (fixed oxygen). We believe that the abundance of molecular oxygen in the nanopores during UV irradiation can favour the formation of oxygen radicals, conducive for the formation of carboxylic acid groups, as illustrated in Scheme 1. Aldehydes and unsaturated ketones are not observed as final photo products. The 60% of oxygen contained in COOH groups is close to the value of 57% estimated by gravimetry as already discussed in the previous paragraph.

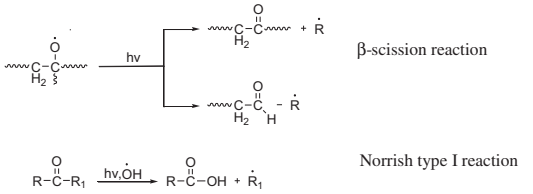

Scheme 1. Photo-oxidation reactions of 1,2-PB after the formation of alkoxy free radicals (see Introduction) forming first carbonyl and afterwards carboxyl groups.

3.2. Distribution of carboxylic group relative to air–polymer interface

In the following we present a method that allows studying the distribution of carboxylic groups relative to the air–polymer interface. It is based on FTIR and gravimetric analysis of oxidized samples treated by NaOH basic solutions with different hydrophilicity, which probe different portions of the polymer wall around nanopores.

Table 2 shows result for 3 different solvent systems used to carry out an acid-base reaction between carboxylic groups formed after photo-oxidation and NaOH. Three different solvents are chosen to address the concentration of carboxylic groups within different volumes in the nanoporous system. 0.250 M NaOH solution in MilliQ water is diluted in the respective solvents to prepare final solutions used for the experiment. Samples' initial mass and dry mass after treatment is recorded. The purely aqueous NaOH solution is expected to probe the nanopores and the most hydrophilic part of the modified polymer, whereas methanolic NaOH can penetrate further into the bulk of PB, away from the air–polymer interface. Finally, the THF basic solution can probe both the nanopores as well as cross-linked polymer matrix. The THF-containing solvent system registers high volume uptake value as THF can both fill the pore volume and swell the cross-linked polybutadiene matrix. The most important information obtained by Table 2 is that the concentration of carboxylic groups measured by FTIR, as illustrated in Fig. 5, is the same for both the methanol and the THF basic solutions, while the concentration probed by the basic water solution is 7% lower on the front side and 9% on the back side of the sample. These findings are consistent with a scenario where methanol probes all the carboxylic groups (no additional groups probed by THF), while water probes the polymer–air interface where it is most hydrophilic, missing a small fraction of the carboxylic groups found at low concentration deeper in the polymer matrix. In the following paragraph we try to understand the quantities of water and methanol uptake given in Table 2 as related to available sample porosity and assuming volume additivity. This

Table 2
Three solvent systems probing carboxylic groups in UV modified nanoporous polymer.

Solvent	Volume uptake (%)[a]	Peak ratio front side[b]	Peak ratio back side[c]
$NaOH + H_2O$	63.5 ± 0.2	2.40 ± 0.3	0.53 ± 0.05
$NaOH + H_2O$ + methanol	80.00 ± 0.5	2.57 ± 0.3	0.57 ± 0.05
$NaOH + H_2O$ + THF	108.7 ± 0.5	2.54 ± 0.7	0.58 ± 0.05

[a] Volume uptake (%) $= 100 \times \Delta m/(\rho \times m)$, where m is the dry mass of the oxidized sample and Δm the mass uptake of solution with density ρ.
[b] Peak ratio on the side facing UV for the FTIR absorbance peaks at 1568 cm^{-1} (carboxylate ion peak) and at 2917 cm^{-1} (C–H sp^3 peak), see Figs. 5 and 6.
[c] Peak ratio calculated as in table footnote b, but on the back side of the sample, see Fig. 6.

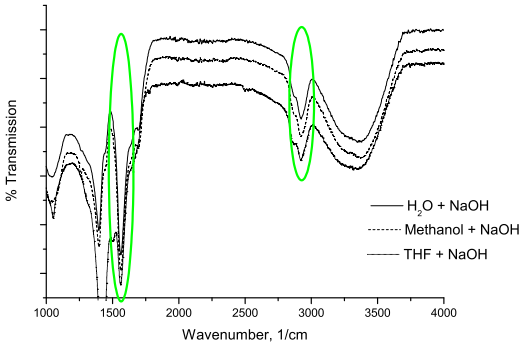

Fig. 5. FTIR transmission spectra of photo-oxidized samples treated with: water + NaOH, methanol + water + NaOH and THF + water + NaOH, normalized relative to the hydrocarbon peak at 2917 cm^{-1}. The spectra are vertically offset for the sake of clarity. The height ratios between the two groups of highlighted peaks are listed in the 2nd data column of Table 2.

will allow to obtain an approximate picture of the spatial distribution of COOH groups relative to the pore walls.

First, the specific porosity of the original nanoporous sample can be calculated as $m_{PDMS}/m_{PB}/\rho_{PDMS} = 0.41/(0.59 \times 0.97\ g\ cm^{-3}) = 0.72\ cm^3\ g^{-1}$. The total specific volume of polymer and pores is $1.72\ cm^3\ g^{-1}$, the density of the cross-linked matrix being $1.00\ g\ cm^{-3}$ [15]. The fractional mass uptake of oxygen after UV radiation is 0.15 relative to the original nanoporous polymer. SAXS measurements of the photo-oxidized samples in water and in methanol are consistent with volumetric swelling factors of 1.00 (no swelling) and 1.09, respectively, relative to the original nanoporous sample [19]. The absence of swelling in water is consistent with the simple situation of water exclusively filling the porous volume of the photo-oxidized polymer. Sample swelling driven by the diminished surface energy of the water wet sample relative to the dry sample is evidently insignificant, most probably due to the high cross-linking degree of the polymer matrix. If all the oxygen were fixed in a 0.5–0.6 nm thick polymer layer around the pores (see Scheme 2), an average density of 1.4–1.3 $g\ cm^{-3}$ for this layer in the dry state would leave enough pore volume for the observed water uptake given in Table 1. Now, densities in the range 1.3–1.4 $g\ cm^{-3}$ are quite realistic for oxygen-rich polymers, even in the absence of cross-linking; for example bulk density values for poly(acrylic acid)s are in excess of $1.5\ g\ cm^{-3}$, while $1.3\ g\ cm^{-3}$ is the reported value for polyvinyl alcohol [20,21]. Methanol swells the oxidized polymer by about 9% (v/v). It's possible that in addition to the pore volume, methanol also partially penetrates the cross-linked matrix, which causes sample swelling. A 9% swelling increases the initial $1.72\ cm^3$ (per gram of unmodified polymer) into $1.87\ cm^3$, of which $1.09\ cm^3$ is photo-oxidized polymer. The rest $0.78\ cm^3$ is available to methanol, which is close to the observed $0.80\ cm^3$ listed in Table 1. Assuming affine swelling, the pore volume increases from $0.64\ cm^3$ (from water uptake) to $0.70\ cm^3$. The remaining $0.10\ cm^3$ of the total gained methanol is then entering the matrix. It's not possible to decide the distribution of methanol within the polymer matrix. The typical uncertainty of the data mentioned in this discussion is of the order of few percent. The observation that water probes about 93% of the carboxylic groups combined with exclusive water confinement within the pores demonstrates that the big majority of carboxylic groups are distributed within a very narrow layer at the polymer–air interface. As mentioned above a layer thickness of the order of 0.5 nm, comparable to one monomer extension, is plausible; this is shown by a step function distribution in Scheme 2,

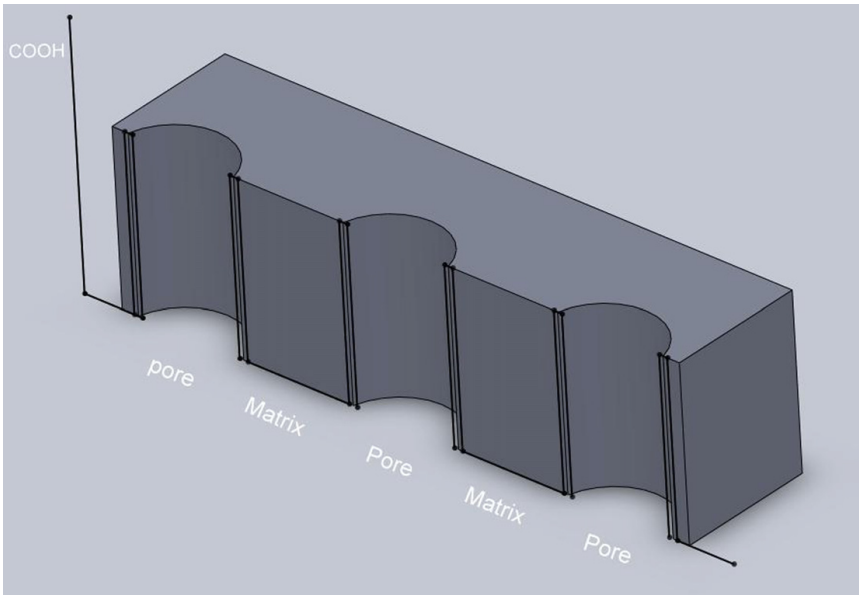

Scheme 2. Carboxylic group distribution in nanoporous polymer system, schematically represented by a step function of width 0.5 nm at the pore wall.

while a more realistic distribution would have been exponential concentration decay from the polymer–air interface into the polymer matrix. The narrow oxidation skin can be a consequence of the high degree of cross-linking of the 1,2-PB matrix [14]; the resulting poor permeability of oxygen into the cross-linked matrix virtually limits its modification to the very interface region after UV exposure.

3.2.1. Average surface density of carboxylic groups by gravimetry and titrimetry

As already mentioned the mass increases by $5.5 \pm 0.1\%$ relative to the native nanoporous polymer (or $4.7 \pm 0.1\%$ relative to the oxidized sample), when hydrogen is exchanged by sodium in the photo-oxidized nanoporous polymer. The mass increase can be expressed as an average surface density of $5.4 \pm 0.7\ nm^{-2}$ carboxylic groups in the polymer, by evenly 'distributing' the groups onto the $280 \pm 40\ m^2$ of surface area in 1 g of native nanoporous polymer. Alternatively, the surface density of carboxylic acid groups is determined by titrimetry. It was carried out by first neutralizing all the COOH groups formed due to photo-oxidation by a base (NaOH) in excess and then titrating the base excess by potassium hydrogen phthalate (PHP). The solid form of PHP facilitates accurate preparation of fixed molar concentration solutions, which is essential while performing sensitive titration reactions. MilliQ water is used as a solvent. The surface density of carboxylic groups calculated by titrimetry on 5 samples was $5.5 \pm 0.9\ nm^{-2}$, which is in very good agreement with the gravimetric result ($5.4 \pm 0.7\ nm^{-2}$).

3.3. Distribution of oxygen and carboxylic groups relative to sample depth by EDX-SEM and FTIR

^{13}C NMR, gravimetric and titration analyses provide average concentrations of photo-oxidation groups in UV treated nanoporous samples. The actual concentration of reacted oxygen is heterogeneous across the sample thickness [3], decreasing from the side which faces the UV source to the back side of the sample. Therefore, the rest of the manuscript addresses the concentration distribution of oxygen in general and carboxylic groups in particular across the thickness of the nanoporous sample. This was carried out using Energy Dispersive X-ray Spectroscopy (EDX) [22] in SEM and by ATR-FTIR. EDX uses a Si chip detector to measure the incoming X-ray generated by an electron gun. The detector measures photon energy and photon count and performs quantitative analysis of elements in the sample along with its normal SEM imaging. The scanning is carried out across the thickness with 10 equally spaced points and the elements C, O, Na are mapped. The *absolute* values obtained by EDX for the three elements are not expected to reflect the actual abundance, as the technique is not quantitative for the light elements. However, in the following we assume that the atomic abundance of O *relative* to Na reflects the real ratio of these two elements. The assumption allows us to estimate the fraction of oxygen fixed in the form of carboxylic groups during photo-oxidation as a function of sample depth relative to the surface facing UV. Fig. 6a and b compares the results on the atomic % of oxygen (left axis in 6a) and sodium (right axis in 6b) obtained by EDX with the concentration of carboxylic groups determined by ATR-FTIR, both as plotted against the sample depth. 0 microns corresponds to the side facing UV irradiation. The right (left) vertical axis in Fig. 6a (b) shows the ratio between intensities of carboxylic acid peak and C–H sp^3 hybridized stretch peak; this last is used as an internal reference. Even though the C–H peak is changing as the nanoporous surface gets modified, as discussed earlier the modification is restricted mainly to the polymer–air interface. Statistically, the majority of C–H peak contribution is coming from the unmodified bulk polybutadiene, which justifies its use as an approximate internal reference in FTIR.

Both EDX and FTIR show a significant decay in oxygen concentration as a function of sample depth away from the UV source. In the case of the EDX, the oxygen concentration falls by a factor of 4 within the first 100 μm of the cross-section. Both analyses indicate

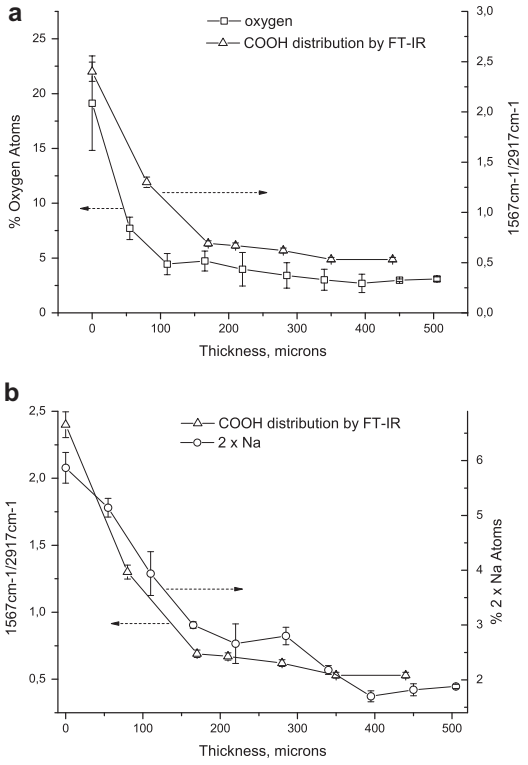

Fig. 6. Distribution of total oxygen and COOH groups across the thickness of photo-oxidized nanoporous polymer mapped by EDX-SEM and ATR-FTIR.

that oxygen is highly concentrated at the top layer, few tens of microns thick, which is directly exposed to the UV source. The oxygen concentration reduces to a much lower and rather homogeneous value across the rest of the sample thickness. From the very start of photo-oxidation the most energetic photons show a much shorter penetration depth in the material, as already observed from the UV–vis absorption data in Fig. 1. Therefore the flux of reactive photons is expected to fall significantly with the depth. It is only the photons at longer wavelengths that can effectively react deeper in the polymer. The FTIR analysis on both sides of the samples treated with NaOH gives rise to very similar spectra (not shown), just the intensity of the bands related to photo-oxidation is significantly reduced on the back side of the sample. Therefore the chemistry throughout the sample seems to be the same, with the caveat of reduced concentration of photo-oxidation groups away from the front surface.

The similar trends in Fig. 6a for total oxygen monitored by EDX and carboxylic groups monitored by FTIR show that the fraction of COOH relative to the total fixed oxygen are roughly constant throughout the sample cross-section. Similar trends are also observed for the monitoring of carboxylic groups by EDX (double concentration of sodium) and FTIR, as illustrated in Fig. 6b. Again, the quantitative determination by EDX of the light elements C, O and Na is difficult, however the similarity in the trends of concentration of carboxylic groups measured by the two methods shown in Fig. 6b allows some confidence that the concentration profiles of O and Na measured by EDX can be useful in a relative scale, at least for semi-quantitative analyses. The relative areas under the concentration profiles of O and 2 × Na give an independent estimate of the average fraction of oxygen in the form of COOH relative to the total oxygen in the sample. The value found is 0.61, which is very similar to the value 0.60 obtained by ^{13}C NMR and comparable to the estimation of 0.57 given earlier in the paper on the basis of NaOH staining and gravimetric. The depth profile of photo-oxidation shown in Fig. 6a and b very clearly illustrates the heterogeneity of the oxidative modification across the sample thickness. The photo-oxidation degree on a 0.5 mm thick nanoporous sample realized by the UV source of the present study diminishes by a factor of 3.3 from the surface facing the UV source to the back surface, as estimated from the variation of Sodium concentration in Fig. 6b. As the sample is hydrophilic throughout the whole thickness, this means that the density of hydrophilic groups close to the frontal outer surface is at least 3.3 times larger than needed for spontaneous water acceptance into the nanopores. The critical pore surface density of carboxylic groups for spontaneous water uptake can be estimated to be 3 nm^{-2} from time-dependent photo-oxidation experiments (data not shown). The excessive photo-oxidation on the most exposed side of the sample can compromise the mechanical stability of the sample due to chain scission accompanying the formation of *e.g.*, carboxylic groups. This is relevant for certain possible applications of the present materials and can be reduced, as discussed below.

Before concluding, we briefly consider the application potential of the photo-oxidized nanoporous polymers presented here. In two separate reports [2,23] we have already demonstrated hydrophilic patterning and wave guiding by UV irradiation applied in the presence of a UV mask. Such samples take up water exclusively in the patterned volume of nanopores exposed to UV, this creating the refractive index contrast that allows wave guiding. We have also demonstrated that a 'hydrophilized' sample behaves exactly in the same way after 6 months of dry storage under Argon [2], showing no sign of (irreversible) hydrophobic recovery, as is typical for many hydrophilically modified polymers [24]. The mechanical stability of the material has not been an issue in the above mentioned applications. However we have observed noticeable material embrittlement for irradiation times exceeding 30 h, even though the gyroid structure apparently remains intact for radiation times of up to 40 h [2]. From preliminary results, mechanical weakening can be minimized by diminishing the heterogeneity of photo-oxidation observed in Fig. 6a and b by: (1) changing the UV source to *e.g.*, a monochromatic source with a wavelength of long penetration depth relative to sample thickness (such as the 365 nm *I*-line of Mercury); (2) reducing the sample thickness (for most applications thicknesses below 50 μm are sufficient); (3) if possible, irradiating the sample symmetrically from both sides. Such measures are necessary, especially for applications requiring materials with good mechanical stability, such as membranes for ultrafiltration. Another strategy that fully conserves the mechanical properties of the nanoporous samples is to use much more efficient reactions than the photo-oxidation reaction of the present study, *e.g.*, thiol-ene photochemistry [25].

4. Conclusions

Photo-oxidation of gyroid nanoporous 1,2-polybutadiene has been performed in the presence of oxygen by exposure to UV of wavelength in the range 300–400 nm. Limited absorption of at least the photons of wavelength exceeding 350 nm combined with a relatively high permeability of oxygen through the nanopores create good conditions for photo fixation of oxygen throughout 500 μm thick films of nanoporous polymer. The most detailed information on the nature and overall concentration of the photo-

oxidation groups is obtained by solid-state ^{13}C NMR. It reveals that about 11% of the carbon atoms are directly bond to oxygen, 43% of the oxygen-containing groups are carboxyls, 24% hydroxyls, 23% ethers and 10% saturated ketones. About 60% of the bound oxygen is found as carboxylic groups. Within the sensitivity of the analyses aldehydes and α, β-unsaturated ketones are absent. The localization study of carboxylic groups reveals that virtually all hydrophilic groups are found within 0.5–0.6 nm at the matrix–air interface of the pore walls. The overall concentration of carboxylic groups obtained by ^{13}C NMR is very well in line with the results from gravimetry, NaOH staining and titrimetry. An average carboxyl surface concentration of $5.5 \pm 0.9\ nm^{-2}$ is estimated by these techniques. It is also shown by EDX-SEM and FTIR on spots uniformly distributed along the cross-section of the oxidized samples that the photo-oxidation process is highly non uniform. A high concentration of carboxylic groups is formed in the first few tens of micrometres from the polymer surface facing UV. The concentration drops by a factor of 4 within the first 100 μm from the surface and then shows little change for the remaining 400 μm of sample thickness. A consistent picture of the type, abundance and distribution of photo-oxidation products of nanoporous 1,2-PB was presented, by combining a number of experimental techniques. Some 'routine' techniques used, like gravimetry, FTIR and titrimetry, provided essential and independent information on surface chemistry, which is only possible due to the 'unusually' high concentration of surface in nanoporous materials. Controlled photo-oxidation of hydrophobic nanoporous polymers is a straightforward route for rendering the porous volume readily accessible to water; patterned hydrophilicity can be realized by use of appropriate masks. Such materials hold great application promise as ultrafiltration membranes, as hydrophilicity contrasted materials for many biological applications or as refractive index contrasted materials for diagnostics, microfluidics and sensors.

Acknowledgements

Kaushal Sagar acknowledges financial support of the LicorT project by Danish Council For Strategic Research (grant no. 09-063776/DSF) and Department of Chemical and Biochemical Engineering for the financial support. M. B. Christiansen acknowledges financial support from the Danish Research Council for Technology and Production Sciences (grant no.: 274-09-0105). We thank Lars Schulte at DTU-Nanotech for the EDX-SEM, Fengxiao Guo now at IRD Fuel Cells A/S in Svendborg, Denmark for the SAXS and Annette Christensen at the Dept. of Science, Systems and Models at Roskilde University for the solid-state ^{13}C NMR measurements.

References

[1] De Paoli MA. Eur Polym J 1983;l9:761.
[2] Ndoni S, Li L, Schulte L, Szewczykowski P, Hansen WT, Guo F, et al. Macromolecules 2009;42:3877.
[3] Adam C, Lacoste J, Lemaire J. Polym Degrad Stab 1989;24:185.
[4] Rabek JF, Lucki J, Ranby B. Eur Polym J 1979;15:1089.
[5] Kagiya VT, Takemoto KJ. Macromol Sci Chem 1976;A10(5):795.
[6] Beavan SW, Phillips D. Eur Polym J 1974;10:593.
[7] Lucki J, Ranby B, Rabek JF. Polym Degrad Stab 1979;15:1101.
[8] Piton M, Rivaton A. Polym Degrad Stab 1996;53:343.
[9] Ranby B. J Anal Appl Pyrol 1989;15:237.
[10] Ivanov VB, Kuznetsova L, Angert LG, Shlyapintokh VY. Polym Sci USSR 1978; 20:526.
[11] Rabek JF, Ranby B. J Appl Polym Sci 1979;23:2481.
[12] Fraisse F, Kumar A, Commereuc S, Verney V. J Appl Polym Sci 2006;99: 2238.
[13] Ndoni S, Vigild ME, Berg RH. J Am Chem Soc 2003;125:13366.
[14] Guo F, Andreasen JW, Vigild ME, Ndoni S. Macromolecules 2007;40:3669.
[15] Schulte L, Grydgaard A, Jakobsen MR, Szewczykowski PP, Guo F, Vigild ME, et al. Polymer 2011;52:422.
[16] Penetration depth of UV light into the polymer is shown in Fig. 1a. It is calculated in the following way: $I/I_0 = 10^{-A}$ (Lambert–Beer's law) and knowing $I/I_0 = e^{-l/\delta}$ (definition of δ) where, I_0 and I are intensity of incident and transmitted light, A is the absorbance, l is the path length which is sample thickness in this case and δ is the penetration depth. From the above we can derive: $\delta = l/(A \cdot \ln 10)$.
[17] Pavia DL, Lampman GM, Kriz GS. Introduction to spectroscopy. 3rd ed. Saunders College Publ; 2001.
[18] Wiles DM, Carlsson DJ. Polym Degrad Stab 1980;3:61.
[19] Li L. Photooxidation of nanoporous cross-linked 1,2-polybutadiene. M.Sc. thesis, Dept Chem Eng and Risø National Lab, Technical University of Denmark; 2007.
[20] Brandrup J, Immergut EH, Grulke EA. Polymer handbook. 4th ed,, vol. 1. New York: John Wiley; 1999.
[21] Hiraoka K, Hidetoshi S, Yokoyamahi T. Polym Bull 1982;8:303.
[22] Blanchard D, Shi Q, Boothyard CB, Vegge T. J Phys Chem C 2009;113:14059.
[23] Gopalakrishnan N, Sagar KS, Christiansen MB, Vigild ME, Ndoni S, Kristensen A. Opt Express 2010;18:12903.
[24] Larsson A, Dérand H. J Colloid Interface Sci 2002;246:214.
[25] Berthold A, Sagar K, Ndoni S. Macromol Rapid Commun; 2011. doi:10.1002/marc.201100243.

Appendix B

Nimi Gopalakrishnan, Kaushal. S. Sagar, Mads Brøkner Christiansen, Martin E. Vigild, Sokol Ndoni, and Anders Kristensen, UV patterned nanoporous solid-liquid-core waveguides, *Optics Express* **2010**, *18,* 12903-12908

UV patterned nanoporous solid-liquid core waveguides

Nimi Gopalakrishnan,[1] Kaushal. S. Sagar,[2] Mads Brøkner Christiansen,[1,*] Martin E. Vigild,[2] Sokol Ndoni,[1] and Anders Kristensen[1]

[1]*Department of Micro and Nanotechnology, Technical University of Denmark, DTU Nanotech, Building 345 East, DK-2800 Kongens Lyngby, Denmark.*
[2]*Department of Chemical and Biochemical Engineering, Technical University of Denmark, DTU Chemical Engineering, Building 423, DK-2800 Kongens Lyngby, Denmark*
**mads.christiansen@nanotech.dtu.dk*

Abstract Nanoporous Solid-Liquid core waveguides were prepared by UV induced surface modification of hydrophobic nanoporous polymers. With this method, the index contrast (δn = 0.20) is a result of selective water infiltration. The waveguide core is defined by UV light, rendering the exposed part of a nanoporous polymer block hydrophilic. A propagation loss of 0.62 dB/mm and a bend loss of 0.81 dB/90° for bend radius as low as 1.75 mm was obtained in these multimode waveguides.

OCIS codes (160.5470) Polymer; (230.7370) Waveguides.

References and links

1. D. Psaltis, S. R. Quake, and C. Yang, "Developing optofluidic technology through the fusion of microfluidics and optics," Nature **442**(7101), 381–386 (2006).
2. M. P. Duggan, T. McCreedy, and J. W. Aylott, "A non-invasive analysis method for on-chip spectrophotometric detection using liquid-core waveguiding within a 3D architecture," Analyst (Lond.) **128**(11), 1336–1340 (2003).
3. M. Holtz, P. Dasgupta, and G. Zhang, "Small-volume raman spectroscopy with a liquid core waveguide," Anal. Chem. **71**(14), 2934–2938 (1999).
4. H. Schmidt, and A. R. Hawkins, "Optofluidic waveguides I. Concepts and implementations," Microfluidics and Nanofluidics **4**(1–2), 3–16 (2008).
5. A. R. Hawkins, and H. Schmidt, "Optofluidic waveguides II. Fabrication and structures," Microfluidics and Nanofluidics **4**(1–2), 17–32 (2008).
6. A. W. Snyder and J. D. Love, "Total Internal Reflection (TIR)," in *Optical Waveguide theory*, (Chapman and Hall, London, 1983)
7. H. Takiguchi, A. Tsubata, M. Miyata, T. Odake, H. Hotta, T. Umemura, and K. Tsunoda, "Liquid core waveguide spectrophotometry for the sensitive determination of nitrite in river water samples," Anal. Sci. **22**(7), 1017–1019 (2006).
8. P. Measor, L. Seballos, D. Yin, J. Z. Zhang, E. J. Lunt, A. R. Hawkins, and H. Schmidt, "On-chip surface-enhanced Raman scattering detection using integrated liquid-core waveguides," Appl. Phys. Lett. **90**(21), 211107 (2007).
9. V. Korampally, S. Mukherjee, M. Hossain, R. Manor, M. Yun, K. Gangopadhyay, L. Polo-Parada, and S. Gangopadhyay, "Development of a Miniaturized Liquid Core Waveguide System With Nanoporous Dielectric Cladding-A Potential Biosensing Platform," IEEE Sens. J. **9**(12), 1711–1718 (2009).
10. W. Risk, H. Kim, R. Miller, H. Temkin, and S. Gangopadhyay, "Optical waveguides with an aqueous core and a low-index nanoporous cladding," Opt. Express **12**(26), 6446–6455 (2004), http://www.opticsinfobase.org/oe/abstract.cfm?URI=oe-12-26-6446.
11. S. Ndoni, M. E. Vigild, and R. H. Berg, "Nanoporous materials with spherical and gyroid cavities created by quantitative etching of polydimethylsiloxane in polystyrene-polydimethylsiloxane block copolymers," J. Am. Chem. Soc. **125**(44), 13366–13367 (2003).
12. M. Hansen, M. Vigild, R. Berg, and S. Ndoni, "Nanoporous crosslinked polyisoprene from polyisoprene - Polydimethylsiloxane block copolymer," Polym. Bull. **51**(5–6), 403–409 (2004).
13. F. Guo, J. W. Andreasen, M. E. Vigild, and S. Ndoni, "Influence of 1, 2-PB matrix cross-linking on structure and properties of selectively etched 1, 2-PB-b-PDMS block copolymers," Macromolecules **40**(10), 3669–3675 (2007).
14. S. Ndoni, C. M. Papadakis, F. S. Bates, and K. Almdal, "Laboratory-scale setup for anionic-polymerization under inert atmosphere," Rev. Sci. Instrum. **66**(2), 1090–1095 (1995).
15. S. Ndoni, L. Li, L. Schulte, P. P. Szewczykowski, T. W. Hansen, F. Guo, R. H. Berg, and M. E. Vigild, "Controlled Photooxidation of Nanoporous Polymers," Macromolecules **42**(12), 3877–3880 (2009).
16. J. E .Mark, in *Polymer data handbook*, (Oxford University Press, New York, 1999)

#127743 - $15.00 USD Received 3 May 2010; revised 27 May 2010; accepted 28 May 2010; published 1 Jun 2010

17. C. Adam, J. Lacoste, and J. Lemaire, "Photo-oxidation of elastomeric materials Part IV–Photo-oxidation of 1,2-polybutadiene," Polym. Degrad. Stabil. **29**(3), 305–320 (1990).
18. I. Papakonstantinou, K. Wang, D. R. Selviah, and F. A. Fernández, "Transition, radiation and propagation loss in polymer multimode waveguide bends," Opt. Express **15**(2), 669–679 (2007), http://www.opticsinfobase.org/oe/abstract.cfm?URI=oe-15-2-669.
19. S. Musa, A. Borreman, A. A. M. Kok, M. B. J. Diemeer, and A. Driessen, "Experimental study of bent multimode optical waveguides," Appl. Opt. **43**(30), 5705–5707 (2004).
20. P. Steinvurzel, B. Kuhlmey, T. White, M. Steel, C. de Sterke, and B. Eggleton, "Long wavelength anti-resonant guidance in high index inclusion microstructured fibers," Opt. Express **12**(22), 5424–5433 (2004), http://www.opticsinfobase.org/oe/abstract.cfm?URI=oe-12-22-5424.
21. A. E. Vasdekis, G. E. Town, G. A. Turnbull, and I. D. W. Samuel, "Fluidic fibre dye lasers," Opt. Express **15**(7), 3962–3967 (2007), http://www.opticsinfobase.org/oe/abstract.cfm?URI=oe-15-7-3962.
22. R. Manor, A. Datta, I. Ahmad, M. Holtz, S. Gangopadhyay, and T. Dallas, "Microfabrication and characterization of liquid core waveguide glass channels coated with Teflon AF," IEEE Sens. J. **3**(6), 687–692 (2003).
23. C. L. Bliss, J. N. McMullin, and C. J. Backhouse, "Integrated wavelength-selective optical waveguides for microfluidic-based laser-induced fluorescence detection," Lab Chip **8**(1), 143–151 (2007).
24. D. Yin, H. Schmidt, J. P. Barber, E. J. Lunt, and A. R. Hawkins, "Optical characterization of arch-shaped ARROW waveguides with liquid cores," Opt. Express **13**(26), 10564–10570 (2005), http://www.opticsinfobase.org/oe/abstract.cfm?URI=oe-13-26-10564.
25. D. Qi, and A. J. Berger, "Chemical concentration measurement in blood serum and urine samples using liquid-core optical fiber Raman spectroscopy," Appl. Opt. **46**(10), 1726–1734 (2007).

1. Introduction

Optofluidics combine optics and fluidics, opening new frontiers in developing optical systems that exploit fluidic properties [1] and analyse the properties of fluids [2,3]. Integration of liquid and optical elements on the same platform is essential for a more compact and robust optofluidic device [4,5]. Liquid-Core waveguides (LCW) confine light and liquid in the same volume providing large interaction length and reduced sample volume. Highly sensitive optofluidics devices can be designed using LCWs. Total internal reflection (TIR) [6] techniques are usually employed to guide light in the LCWs. As water or aqueous solutions ($n \approx 1.33$) forms the core of LCW, the major challenge is in finding a suitable solid cladding material with refractive index below 1.33. Most applied technologies in this field include Teflon AF cladded LCWs [7], Anti Resonant Reflecting Optical Waveguides (ARROWs) [8] and nanoporous clad LCWs [9,10]. Although Teflon AF is widely used, low surface energy and inertness to chemical functionalization present challenges to use this material in planar chip fabrication.

This work presents nanoporous waveguides, consisting of a clad of hydrophobic nanoporous polymer (NP) and a core of hydrophilic NP infiltrated by liquid. The typical pore size (14 nm) and spacing of the nanoporous polymer is significantly smaller than the wavelength of guided light. Therefore, the core of our waveguides is a solid-liquid 'alloy', hence an appropriate acronym for these waveguides would be Solid-Liquid Core Waveguides (SLCW). We also report losses (propagation, bending and coupling loss) observed in these waveguides studied with cutback techniques.

2. Device fabrication

An attractive way to obtain NP polymers is by total or partial removal of one block from self-assembled block copolymers. The morphology of the self-assembled material is determined by the block's volume fraction in block copolymers and by thermodynamical variables [11–13]. In our work, the starting material is a self-assembled diblock copolymer of Polybutadiene and Polydimethylsiloxane (PB-PDMS) [Fig. 1(a)]. PB-PDMS was synthesized by anionic polymerization [14]. The schematic illustration of the working principle of SLCW in 1,2 Polybutadine (PB) nanoporous polymers is shown in Fig. 1. NP polymers were prepared initially by solvent casting the PB-PDMS block copolymer in tetrahydrofuran (THF) with 1 mol % of the cross-linker dicumyl peroxide with respect to the number of double bonds of the PB component. The morphology of the self assembly determines the distribution of pores in the polymer matrix. The material was further cross-linked at 140°C in an argon/nitrogen atmosphere for 2 hours in order to provide mechanical stability to the PB

#127743 - $15.00 USD Received 3 May 2010; revised 27 May 2010; accepted 28 May 2010; published 1 Jun 2010

matrix. A volume fraction of 0.60 for the PB block in the original block polymer was controlled by the polymer synthesis and the obtained self-assembled morphology was of the cubic symmetry $Ia\bar{3}d$, known also as gyroid morphology [11,15]. This morphology provides bicontinuous porosity and high transparency, which are important for the liquid transport and for waveguiding characteristics of the obtained device. The cross-linked PB-PDMS block copolymer was rendered nanoporous by selectively etching the PDMS minority block from the bulk system, using tetrabutyl ammonium fluoride (TBAF) at three times molar excess, relative to the repeating unit of PDMS. Etching took 36 h and was followed by cleaning of the PB matrix in THF and methanol for a total of 16 h. A porosity of 0.44 [Fig. 1(b)] was determined by methanol uptake [13] from the obtained material. The volume fraction of cross-linked PB (0.56) is lower than that of the uncrosslinked PB (0.60) due to increase of density induced by cross-linking.

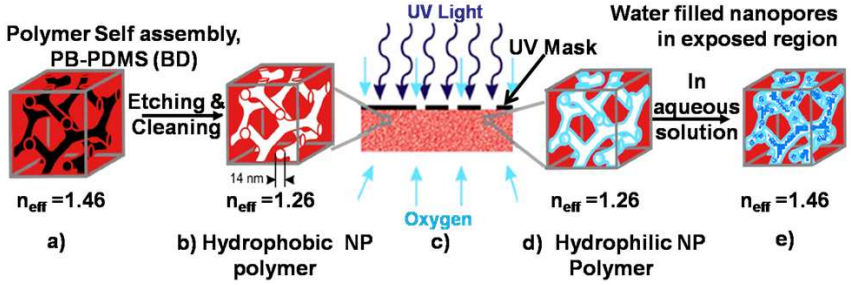

Fig. 1. Schematic illustration of working principle of Liquid Core waveguiding n 1,2-PB nanoporous polymers (a) Polymer self assembly of PB-PDMS, (b) Minority block etched hydrophobic NP polymer, (c) Selectivity UV exposure using a UV mask in presence of oxygen, (d) Hydrophillic NP polymer formed at exposed regions, (e) Exposed region infiltrated with water have changed effective refractive index.

The self-assembled block copolymer and the nanoporous polymer obtained from it can be considered as binary alloys with heterogeneity length scale much lower than the wavelength of visible light. An effective refractive index n_{eff} of the block copolymer or NP can be calculated by the Lorentz-Lorenz relation

$$\frac{n_{eff}^2 - n_1^2}{n_{eff}^2 + 2} = V_2 \frac{n_2^2 - n_1^2}{n_2^2 + 2}, \qquad (1)$$

where n_1, n_2 are the refractive indices of the matrix and the minory component respectively, and V_2 is the volume fraction of the minority component (PDMS or air). In the NP polymer, PDMS minority block (n_2 = 1.40) [16] is replaced with air (n_2 = 1). Thus a 44% porosity (V_2 = 0.44) induces an n_{eff} change from 1.46 for the block copolymer to 1.26 for the NP [Fig. 1(b)]. Photo oxidation [17] in the presence of UV light (300-350 nm) changes the surface wetting property of the naturally hydrophobic 1,2-PB NP polymer [13]. The resultant hydroxyl and carboxyl groups on the matrix air interface, render the exposed region hydrophilic [Fig. 1(c), 1(d)]. On immersion in aqueous solution, water infiltrates the pores in the exposed regions, increasing its effective refractive index (δn_{eff} = 0.20). The index mismatch obtained was exploited to confine light within the solid-liquid core [Fig. 1(e)]. Water evaporation does happen from the surface of the porous waveguide on a timescale of 10-15 minutes. This does not affect our experiments, which are done much faster, and in the future, when we expect to add a cladding, this should further minimize evaporation. When the waveguides dry they seize to guide light. To verify water infiltration we used an organic fluorescent dye (Rhodamine 6G), in aqueous solution. These molecules are smaller than the pores, and thus they infiltrate the exposed regions. As the index mismatch induced is governed by the liquid infiltration of

#127743 - $15.00 USD Received 3 May 2010; revised 27 May 2010; accepted 28 May 2010; published 1 Jun 2010

nanopores, the liquid core will always confine light in these systems. For instance, even if the initial NP polymer (owing to less porosity) had a n_{eff} >1.33, the liquid filled NP region (solid-liquid core) will always have an effective index of refraction higher than the cladding material. We call this type of waveguide a nanoporous solid-liquid core waveguide, shortly NP SLCW or simply SLCW.

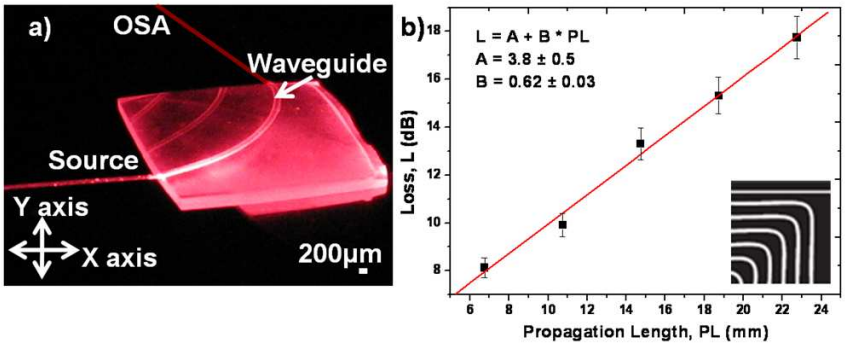

Fig. 2. (a) Experimental setup for measuring propagation and bend loss in the NP LCW, (b) Loss (L) in waveguides with different lengths as a function of propagation length (PL). The solid curve is a linear fit to the measured data. (Inset) 1.5 × 1.5 cm UV mask designed for measuring propagation loss in NP polymer LCW.

3. Results and discussions

The SLCWs were characterized by measuring the losses in the waveguide. Four types of losses occur in rectangular waveguides with bends: input and output coupling, transition, radiation and propagation loss [18,19]. Since the shape of the waveguide is not optimized we have chosen not to focus on transition and coupling losses. Transition losses depend on the waveguide design, e.g. when changing from a curved to a straight section. This can be minimized in the design phase, but cannot be avoided completely in any integrated system. Coupling losses from outside the chip might be an issue, especially if water evaporates from the ends [20,21]. We have not experienced water evaporation causing bubbles, perhaps due to the nanoporous nature of our cladding. Evaporation from the ends is not more pronounced than from the sides in our case.

In this work, propagation loss in 1,2-PB SLCW was studied using the cutback technique. Waveguides of cross section 200 × 200µm were defined with UV patterning using lithography masks as shown in Fig. 2(b). A He-Ne laser (632.8nm) was butt coupled into the SLCW using a 62.5/125µm multimode (MM) fiber. The output from the waveguide was collected with similar MM fibers into an Optical Spectrum Analyser (OSA) (Ando AQ-6315A). The experimental setup is shown in Fig. 2(a). Each waveguide was designed with a 90° bend of radius R = 2mm sandwiched between straight waveguides of varying length. The loss in straight waveguide was obtained by subtracting the loss from 90° bend waveguide of radius, R = 2mm. This removes the coupling and radiation losses. The propagation loss was evaluated by plotting straight waveguide loss as a function of propagation length [Fig. 2(b)]. A linear fit [straight line in Fig. 2(b)] to the data, gives the propagation losses in these waveguides. The constant A [Fig. 2(b)] represents the transition losses when light propagates through different types of waveguides (straight and bend). A transition loss of 3.8 ± 0.5dB and a propagation loss of 0.62 ± 0.03 dB/mm were obtained in the NP SLCWs.

Bending loss evaluation was carried out on waveguides with 90° bend of different bend radius ranging from 1.75 to 11.75 mm. Each of the bend waveguides were sandwiched between 2mm long straight waveguides. The total loss in the bend region was plotted as a function of bend radii in Fig. 3. The loss is obtained by removing coupling and propagation

#127743 - $15.00 USD Received 3 May 2010; revised 27 May 2010; accepted 28 May 2010; published 1 Jun 2010

losses from the straight waveguide section in the design. Transition loss, propagation loss and radiation loss in the bend waveguides were interpreted by fitting a polynomial to the data. The intercept A1 partially indicates transition losses in the waveguide while the linear coefficient B1 contributes to propagation and radiation losses. Each bend waveguide has a propagation length of $(\pi/2) \times R$, (bend radius). Thus the B1 coefficient in Fig. 3 would be expected to be $\pi/2$ times larger than the B coefficient from Fig. 2. That it is somewhat larger in this case is attributed to fabrication differences. With increasing bend radius, a bend waveguide has longer propagation length and lesser degree of bend. This reduces the radiation loss in the waveguide, giving more prominence to propagation losses. The magnitude of the total loss for large bend waveguides is in good agreement with losses from straight waveguides of similar length. |B2| corresponds to the radiation losses in these waveguides.

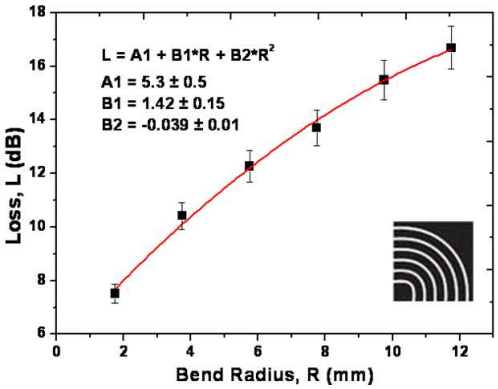

Fig. 3. Total loss (L) is plotted as a function of bend radius (R) for 90° bend waveguides. The solid curve is a polynomial fit to the measured data. (Inset) 1.5 × 1.5 cm UV mask designed with 90° bend waveguides with different bend radii ranging from 1.75 to 11.75 mm.

Since |B2| is very small, propagation loss dominates in our device designs. In NP LCW devices, bend loss of 0.81 dB/90° bend for a small bend radius of 1.75 mm was observed. In the current work, the optimum coupling and transition loss is not discussed. Even with present loss values compared with Teflon AF 2400 waveguides (loss = 0.03 dB/mm) [22], UV modified NP materials could be an alternative for LCW. As typical lengths of optofluidic devices in detection systems are of order of centimeters, high surface area for functionalization and high numerical aperture (NA = 0.74) make UV modified NP a very viable material. In comparison with other types of LCWs [23,24], NP SLCW currently have slightly higher losses. We anticipate that with improved lithography techniques and optimization the losses in these waveguides can be reduced due to smoother surfaces. Optimized lithography should also make it possible to define single mode waveguides. It is also noted that our fabrication technique enables tuning of the index contrast, which can be minimized to lower the number of supported modes.

4. Conclusion

We have illustrated the working principle behind NP SLCWs, where the waveguide core is defined by UV induced hydrophilization of a nanoporous polymer matrix. A quantitative analysis of losses observed in these devices has also been performed. With SLCWs, the major challenges faced in liquid core waveguiding technology can be addressed, in particular simple fabrication and the possibility of having an effective core index above that of the analyte. In addition to the refractive index tuning flexibility, these systems have very high surface area. If the surface is chemically functionalized the interaction between optical field and analyte bound to the surface is vastly enhanced compared to a conventional liquid core waveguide.

#127743 - $15.00 USD Received 3 May 2010; revised 27 May 2010; accepted 28 May 2010; published 1 Jun 2010

Light and water confinement in the same microchannel as well as nanoporosity makes NP SLCWs very promising devices for new applications in optofluidics [25].

Acknowledgments

The financial support of the LiCorT Project by the Danish Council for Strategic Research (grant no. 09-063776/DSF) is gratefully acknowledged. Mads Brøkner Christiansen is financially supported by the Danish Research Council for Technology and Production Sciences (grant no. 274-09-0105)

#127743 - $15.00 USD Received 3 May 2010; revised 27 May 2010; accepted 28 May 2010; published 1 Jun 2010

Appendix C

Anton Berthold, Kaushal Sagar, Sokol Ndoni, Patterned Hydrophilization of Nanoporous1,2-PB by Thiol-ene Photochemistry, *Macromolecular Rapidcommunications* **2011**, *32,* 1259-1263

Macromolecular Journals

Macromolecular Rapid Communications

Patterned Hydrophilization of Nanoporous 1,2-PB by Thiol-ene Photochemistry

Anton Berthold,[a] Kaushal Sagar,[a] Sokol Ndoni*

We present an efficient method for functionalizing the large polymer–air interface of a gyroid nanoporous polymer. The hydrophilicity of nanoporous cross-linked 1,2-polybutadiene is tuned by thiol-ene photo-grafting of mercaptosuccinic acid or sodium 2-mercaptoethanesulfonate. The reaction is monitored by FT-IR, UV–Vis, contact angle, and gravimetry. Overall quantum yields are calculated for the two thiol-ene "click" reactions in nano-confinement, neatly revealing their chain-like nature. Top–down photolithographic patterning is demonstrated, realizing hydrophilic nanoporous "corridors" exclusively hosting water. The presented approach can be relevant for many applications where, e.g., high control and contrast in hydrophilicity, chemical functionality or refractive index are needed.

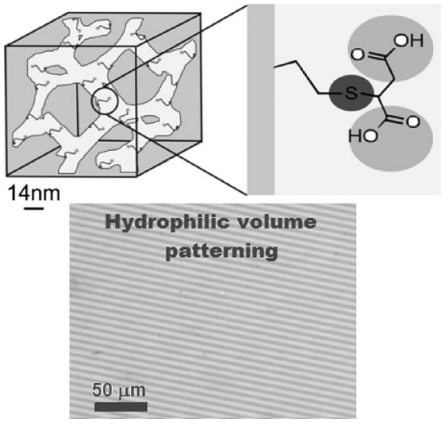

Introduction

Block copolymers are known to form different ordered morphologies depending upon the composition and thermodynamic conditions.[1] Nanoporous polymers (NP) derived from such self assembled block copolymer precursors are materials with large internal surface area (50–500 $m^2 \cdot g^{-1}$) and high level of structural order.[2,3] NP exhibit crystal-like symmetry elements of characteristic length scale in the range of 15–200 nm and pore diameters in the range of 5–50 nm. NPs hold great potential in areas such as catalysis, sensing, and membrane technology.[4,5] The length scale of the structural order also allows to use NP for optical applications.[6] The vast internal surface area of the NP can be modified by different functionalities covalently attached[7,8] or physisorbed[9] to the air–polymer interface. Hydrophilicity of the polymer–air interface in the nanopores can be selectively tuned to suit for opto-fluidic applications, i.e., liquid-core waveguides.[6,10] In our group we have previously reported on the successful hydrophilization of nanoporous 1,2-polybutadiene (1,2-PB) by photo oxidation.[8] In this communication a new, much more efficient, specific, and versatile hydrophilization method is reported using thiol-ene chemistry to modify the polymer–air interface with thiols having terminal hydrophilic groups. The highly efficient reaction of thiols with carbon–carbon double bonds is reported for the first time in 1905.[11] In 2001, Sharpless and coworkers[12] introduced the concept of "click" reactions. It encompasses reactions with high yield that, among others, are regio- and stereo specific, insensitive to oxygen or water and amenable with many different starting compounds.[13–15] The copper (I) catalyzed 1,3-dipolar cycloaddition of azides and alkynes is

S. Ndoni, A. Berthold
Department of Micro and Nanotechnology, Technical University of Denmark, Produktionstorvet 423, 2800 Kgs. Lyngby, Denmark
E-mail: sond@nanotech.dtu.dk
K. Sagar
Department of Chemical and Biochemical Engineering, Technical University of Denmark, Søltofts Plads 227, 2800 Kgs. Lyngby, Denmark

[a] Anton Berthold and Kaushal Sagar have contributed equally in the current work.

DOI: 10.1002/marc.201100243

the most known example,[16] but thiol-ene chemistry also meets the criteria. In polymer science, thiol-ene chemistry is applied both in photo[17] and thermo[18,19] initiated polymerization, and as a tool for surface modification[20–21] and polymer crosslinking.[22–24] The chemistry involves a step-growth addition mechanism where the initiated thiyl radicals (by a thermal or photochemical initiator) adds to *ene* functionalities and the generated carbon centered radicals abstract hydrogen from free thiols creating new thiyl radicals. In-chain C—C double bonds react at least one order of magnitude slower than pendant vinyls.[25,26]

In the present work we modified by thiol-ene photochemistry, nanoporous 1,2-PB derived from an anionically synthesized 1,2-PB-*b*-PDMS di-block copolymer precursor. The NP was obtained by firstly cross-linking at a high degree the 1,2-PB block and subsequently removing the PDMS block, as described elsewhere.[27] The morphology of the block copolymer at the cross-linking temperature (140 °C) is gyroid; PDMS is the minority block with a 0.40 volume fraction. After the selective and quantitative removal of PDMS, gyroid porosity is generated in the space previously occupied by PDMS. The internal surface area of the NP is estimated to $283 \pm 14\,m^2 \cdot g^{-1}$ by isothermal nitrogen adsorption.[27] 30–50% of the original double bonds in 1,2-PB typically survive the cross-linking reaction[2] and are preferred loci for coupling of thiols by thiol-ene chemistry. Mercaptosuccinic acid (MSA) and sodium 2-mercaptoethanesulfonate (MESNA) (Scheme 1) are grafted onto the pendant vinyl groups of nanoporous 1,2-PB by the following procedure. Films with $195 \pm 5\,\mu m$ thickness and without skin layer are first prepared according to a method earlier reported by our group.[28] Solutions of 500 mM thiol (MSA or MESNA) and 10 mM of the photo initiator (2,2-dimethoxy-2-phenylacetophenone, DMPA) are prepared. For the MSA system ethanol is used as solvent and for the MESNA system the solvent is a 25/75 v/v mixture of water and methanol. Nanoporous samples (8–20 mg and 0.68–1.70 cm^2) are immersed in the solutions for 2–3 h. The samples are placed on filter papers (3×3 cm) soaked with the same solution and covered with a borosilicate glass wafer (diameter 10 cm, thickness 500 μm). This method allows homogenous wetting of the samples while preventing them from drying out during the photoreaction. All preparations are performed in the dark or in yellow light ($\lambda > 500$ nm) in the cleanroom. The irradiation source is a collimated 1 000 W high Hg (Xe) pressure lamp (Newport) filtered at 367 ± 20 nm wavelength with an irradiation intensity at the sample position of $7.65 \pm 0.05\,mW \cdot cm^{-2}$. The absorption at 367 ± 20 nm by the NP loaded with the reactive solution is used to calculate the absorbed moles of photons (in *Einsteins E*) per g of NP. It is measured by using as reference a similar piece of NP immersed in the solvent alone. After exposure all samples are ultrasonicated in the respective solvents three times to remove non-reacted compounds and dried for 8 h under vacuum. Mass uptake in the dry state is measured on a precision balance (±0.01 mg) and calculated as groups per nm^2.

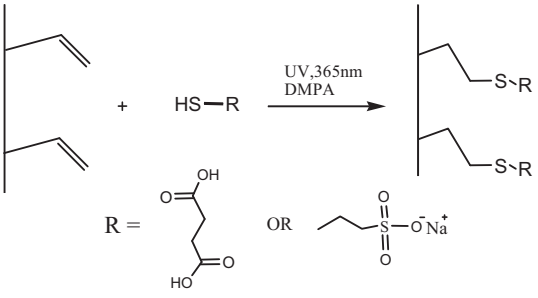

Scheme 1. Reaction scheme for thiol click reaction with the pendant unsaturation of nanoporous 1,2-PB.

Results and Discussion

Scheme 1 illustrates the overall reaction of the thiols by photo grafting onto the pendant unsaturated groups in the nanopores. The photoinitiator DMPA triggers the initiation of radical formation upon UV excitation. It generates thiyl radicals by hydrogen abstraction.[21] The propagation reaction begins where the thiyl radical attacks pendant double bonds and generates a vinyl radical which abstracts hydrogen from a new thiol molecule, and so on.[21] ATR FT-IR spectra of the NP before and after the thiol-ene reactions are shown in the left panel of Figure 1. The modified polymer shows newly developed absorption peaks at 1 710 cm^{-1} due to carbonyl groups in the case of MSA and 1 050 and 1 220 cm^{-1} due to S=O (symmetric and antisymmetric) stretching, respectively, in the case of MESNA. The reduction of C=C absorption peak at 904 cm^{-1} in the case of MSA and MESNA modified samples compared to untreated NP also confirms the consumption of the unsaturations. The right panel of Figure 1 shows static contact angle (CA) images for unmodified hydrophobic polymer and thiol treated (MSA and MESNA) samples. The images show a water droplet on flat outer surfaces of the NP samples. Images are recorded within 10 s from the deposition of a 1 μl de-ionized water droplet onto the surface. The average values over a span of 3 samples (on both sides of each sample) are reported. The average CA values both for MSA ($35 \pm 2°$) and MESNA ($24 \pm 2°$) are considerably lower than for the unmodified NP polymer ($101 \pm 3°$). Within 25 s the water droplet is absorbed by capillary suction from the surface into the hydrophilic nanopores of the modified systems. In the case of

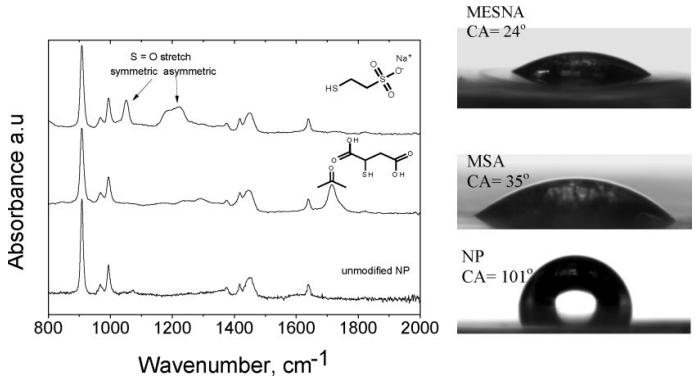

Figure 1. FT-IR spectra and static CAs of water on NP before modification (NP), and after modification with MSA or MESNA.

unmodified sample, it takes more than 1 min for the water droplet to evaporate without being able to wet the pores.

Some insight on the nature of the photo-reaction is gained by the calculation of the reaction's quantum yield. The initial overall quantum yield $\overline{Q}^0_{\text{thiol}}$ is the average number of thiol molecules clicked onto the pore walls per photon absorbed by the NP film loaded with thiol solution at the initial stage of reaction.[8,29] It can be calculated by the ratio between the initial rate of grafted mass uptake of NP expressed as "moles of grafted thiol per second per g of NP," and the initial rate of photon absorbed, expressed as "moles of absorbed photons (Einsteins) per second per g of NP." In more formal notation $\overline{Q}^0_{\text{thiol}}$ can be expressed as:

$$\overline{Q}^0_{\text{thiol}} = \left[\frac{(dn_{\text{thiol}}/dt)}{(dn_{\text{photon}}/dt)}\right]_{t=0} ; \qquad \lambda = 367 \pm 20 \text{ nm} \qquad (1)$$

The numerator and the denominator are the rates of grafted thiol and of photons absorbed, respectively, both expressed in $\text{mol} \cdot \text{s}^{-1} \cdot \text{g}^{-1}$. The rate of photon absorption is calculated by first converting the UV photon count data at the sample position from arbitrary units into absolute incident photon mole intensity (n_0 (λ) in Einsteins). This is done by converting the measured incident power ($7.65 \pm 0.05 \text{ mW} \cdot \text{cm}^{-2}$) into moles of photons for each wavelength in the range 367 ± 20 nm, with the single photon energy given by the product of the Planck's constant h with the speed of light c and the inverse of wavelength in vacuum: $h \times c \times \lambda^{-1}$. The specific surface area defining the flux of incident photons is $85.5 \pm 2 \text{ cm}^2 \cdot \text{g}^{-1}$ for a 195 ± 5 μm thick NP film. Secondly, the rate of absorbed photons n_{photons} is calculated by the numeric sum of n_0 (λ) weighed by the fraction of absorbed irradiation at that wavelength, as measured by UV spectroscopy:

$$n_{\text{photons}} = \sum\nolimits_{\lambda} [1 - T(\lambda)] n_0(\lambda) \qquad (2)$$

T (λ) is the transmission at a particular wavelength and the summation is carried over the discrete wavelength values provided by the photon count and the UV–Vis transmission data in the range of $\lambda = 367 \pm 20$ nm (see Figure 2). The calculated rates of photon absorption are 1.06×10^{-7} and 1.35×10^{-7} Einsteins $\cdot \text{g}^{-1} \cdot \text{s}^{-1}$, respectively, for the MSA and MESNA systems (see Figure 2).

The numerator in Equation (1) can be estimated from the initial slope of the mass uptake data in Figure 3a and b. The values for the initial grafting rates of MSA and MESNA are 2.17×10^{-6} and 1.02×10^{-5} $\text{mol} \cdot \text{g}^{-1} \cdot \text{s}^{-1}$, respectively. Thus by combining Equations (1) and (2) the quantum yield obtained for MSA is 21 ± 3 and 76 ± 6 for MESNA. The high quantum yield ($\overline{Q}^0_{\text{thiol}} > 1$) reflects the nature of the photo-grafting as a chain reaction of the thiols with the pendant vinyl groups of 1,2PB. It is possible that the increase of mass uptake, after 20 min for MSA and after 200 s for MESNA, is due to slower reaction with the 10% of double bonds in the form of 1,4-unsaturations in PB.[25,26]

The difference in the grafting kinetics observed by inspection of the panels (a) and (b) of Figure 3 for the two thiols is most probably related to steric effects, MESNA

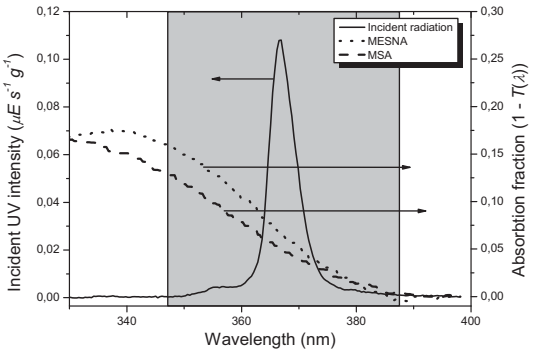

Figure 2. Incident radiation intensity onto the NP film and absorbed fraction of radiation for the two thiol systems as a function of wavelength. The incident intensity is expressed in μEinstein per second per gram of NP film (1 g of 195 μm thick NP film exposes to UV an area of 85.5 cm^2). The absorbed fraction of incident photons (right axes) is derived from UV–Vis spectroscopy. $T(\lambda)$ is the transmittance at λ nm. The integration wavelength region used for the calculation of the overall quantum yield (Equation 1) is marked by the gray background.

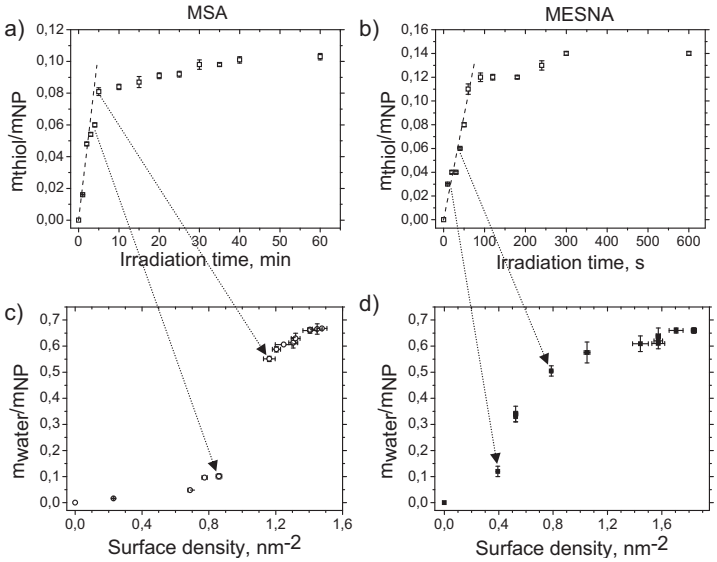

Figure 3. Dry mass uptake (upper row) and equilibrium water mass uptake (bottom row) for the NPs modified by (a, c) MSA and (b, d) MESNA. The *x*-axes are either irradiation time or surface density of grafted thiols onto the nanopore walls. The arrow couples connecting corresponding data points highlight the dramatic increase in water uptake, from 15 to 80% of porosity, at narrow irradiation time intervals; from 4 to 5 min in the case of MSA and from 10 to 40 s in the case of MESNA.

being a primary and MSA a secondary thiol. For the sake of comparison, a much lower initial quantum yield of 0.24 ± 0.03 was estimated for the reaction of oxygen photo-fixation onto the nanopore walls of a similar NP.[8] The typical reaction time was in that case 20–30 h and the modification was very heterogeneous, with a high photo-oxidation degree close to the surface facing the UV source and a significant decrease at depths beyond some 30–40 μm in the sample.[8] A number of different and uncontrolled functional groups were created in that case. All these disadvantages have disappeared by applying the thiol-ene modification procedure of the same NPs. The reactions here are fast, specific, quantitative, and homogeneous; also there is no sample coloration occurring. In the following two paragraphs we substantiate the important issues of homogeneity and quantitative reaction of the double bonds at the pore surface by thiol-ene photo-grafting.

Figure 3c and d illustrate water mass uptake of modified NP plotted against the surface density of grafted thiol groups in the nanopores. The equilibrium water uptake is calculated with reference to the mass of the pristine nanoporous sample. The surface density is calculated as:

$$\rho_{\text{thiolgroups}} = \frac{n_{\text{thiol}}}{S_{\text{NP}}} \times 6.022 \times 10^{23} \quad (3)$$

where, $\rho_{\text{thiol groups}}$ is the surface density of thiol groups per nm^2, n_{thiol} is the moles of thiol groups grafted per g of NP, and S_{NP} is the specific internal surface area of the NP, which is $283 \pm 14\ \text{m}^2 \cdot \text{g}^{-1}$. The hydrophilicity transition, i.e., the transition from minor water uptake to virtually full water uptake is rather sharp for both thiols (Figure 3c and d). This suggests that the photo grafting process is quite homogeneous throughout the sample thickness of 195 ± 5 μm. In the case of MSA the water uptake changes abruptly from less than 15% of the porosity after 4 min of photo-grafting to more than 82% of the pore volume after 5 min of photo-grafting. In the case of MESNA the hydrophilic "jump" happens between 10 and 40 s of irradiation. Approximate critical surface densities for hydrophilic conversion of 0.95 and $0.53\ \text{nm}^{-2}$ can be estimated for MSA and MESNA, respectively, as the interpolated value for 50% filling of pore volume with water. MESNA needed lower degree of surface grafting compared to MSA, probably due to the more hydrophilic nature of the terminal sodium sulfonate group in MESNA than the carboxylic groups in MSA. The uniformity of modification of the final dry samples is independently supported by virtually identical ATR-FTIR spectra recorded at different points across the cross section of the modified samples (data not shown). The internal surface areas of grafted samples as measured by nitrogen adsorption are practically unchanged relative to the surface area of the unmodified sample: $282 \pm 14\ \text{m}^2 \cdot \text{g}^{-1}$ for the MSA-modified and $276 \pm 14\ \text{m}^2 \cdot \text{g}^{-1}$ for the MESNA modified samples, as compared to $283 \pm 14\ \text{m}^2 \cdot \text{g}^{-1}$ for the unmodified sample.

The initial density of pendant vinyl groups on the polymer–air interface is $1.80\ \text{nm}^{-2}$, as calculated from the amount of double bonds disappeared during cross-linking and the initial amount of double bonds.[2] Thus in the case of MESNA virtually all interface double bonds are consumed after 10 min of photo-grafting. In the case of MSA, the surface density recorded after 60 min of reaction is $1.5\ \text{nm}^{-2}$, corresponding to 83% of the available surface double bonds. These results demonstrate the quantitative or nearly quantitative nature of the thiol-ene reaction,[18] this time in nanopore-confined conditions. The maximum volume occupied by water after hydrophilization is $0.65\ \text{cm}^3 \cdot \text{g}^{-1}$, which constitutes 91% of the porosity of the unmodified NP. The remaining 9% are occupied by the photo-grafted thiols, ignoring some possible slight sample swelling.

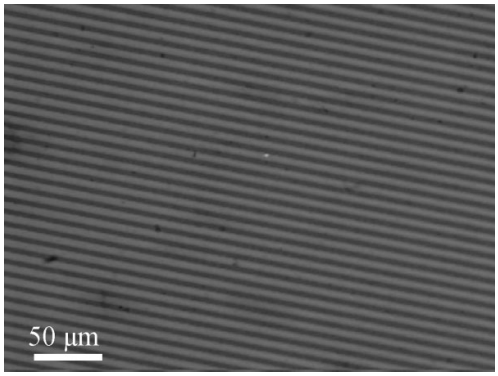

Figure 4. Alternating hydrophilic–hydrophobic pattern realized by photo-grafting of MSA in the presence of a photolithographic mask. Each stripe is 5 μm wide. Water exclusively enters the nanoporous "corridors" exposed to the UV radiation found within the dark stripes.

Finally Figure 4 shows a hydrophilically patterned NP fabricated by using a photolithographic mask in the course of thiol-ene photoreaction. An alternating pattern of hydrophilic and hydrophobic "corridors" (each 5 μm wide) is formed with the help of MSA thiol photo grafting in the nanopores. Water is self-confined in the hydrophilized fraction of pores. This can be interesting for several applications in biological or diagnostics areas involving for example cell culturing.

Conclusion

We have presented UV assisted thiol-ene chemistry using MSA and MESNA for rapid hydrophilization of 1,2-PB. The thiol-ene approach for hydrophilization is efficient, easy, does not require special reaction conditions, homogeneous, and quantitative. Overall quantum yields of 21 and 76 are calculated for the MSA and MESNA systems, reflecting the chain-like nature of the thiol-ene reaction. The higher value for the MESNA grafting is probably related to the lower steric hindrance around the primary thiol group in MESNA as compared to the secondary thiol group in MSA. Nanoporosity and the precise control of chemical functionality of the vast polymer–air interface create possibilities for interesting applications in sensing and optofludics. The demonstrated hydrophilic patterning on NP by thiol-ene photochemistry can also be useful for biochemical and diagnostics applications.

Acknowledgements: We thank Danchip, DTU for providing cleanroom facility and collimated UV source, Nimi Gopalakrishnan (DTU-Nanotech), Mads Brøkner Christiansen (DTU-Nanotech), Anders Kristensen (DTU-Nanotech), and Peter Thomsen (Biomodics, Denmark) for useful discussions. The work reported here was carried out under the LiCorT project financed by the Danish Council for strategic research (grant no. 09-063776/DSF). Kaushal Sagar acknowledges the Department of Chemical and Biochemical Engineering at DTU for the financial aid.

Received: April 13, 2011; Revised: May 16, 2011; Published online: June 20, 2011; DOI: 10.1002/marc.201100243

Keywords: hydrophilic; nanoporous; photo-initiated; thiol-ene

[1] F. Bates, H. Frederickson, *Annu. Rev. Phys. Chem.* **1990**, *41*, 525.
[2] F. Guo, J. Andreasen, M. E. Vigild, S. Ndoni, *Macromolecules* **2007**, *40*, 3669.
[3] S. Ndoni, M. E. Vigild, R. H. Berg, *J. Am. Chem. Soc.* **2003**, *125*, 13366.
[4] M. Ulbricht, *Polymer* **2006**, *47*, 2217.
[5] N. Gupta, C. Hawker, *Nature Chem.* **2010**, *2*, 138.
[6] N. Golapakrishnan, K. Sagar, M. Christiansen, M. E. Vigild, S. Ndoni, A. Kristensen, *Opt. Expr.* **2010**, *18*, 12903.
[7] F. Guo, K. Jankova, M. E. Vigild, S. Ndoni, *Langmuir* **2010**, *26*, 2008.
[8] S. Ndoni, L. Li, L. Schulte, P. Szewczykowski, T. Hansen, F. Guo, R. H. Berg, M. E. Vigild, *Macromolecules* **2009**, *42*, 3877.
[9] L. Li, Y. Wang, M. Vigild, S. Ndoni, *Langmuir* **2010**, *26*, 13457.
[10] W. Risk, H. Kim, R. Miller, H. Temkin, S. Gangopadhyay, *Opt. Expr.* **2004**, *12*, 6446.
[11] T. Posner, *Ber. Dtsch. Chem. Ges.* **1905**, *38*, 646.
[12] H. Kolb, M. Finn, K. Sharpless, *Angew. Chem.* **2001**, *113*, 2056.
[13] C. Decker, *Macromol. Rapid Commun.* **2003**, *23*, 1067.
[14] A. Inglis, C. Barner-Kowollik, *Macromol. Rapid Commun.* **2010**, *31*, 1247.
[15] O. Turunc, M. Meier, *Macromol. Rapid Commun.* **2010**, *31*, 1822.
[16] C. Tornoe, C. Christensen, M. Meldal, *J. Org. Chem.* **2002**, *67*, 3057.
[17] T. Wickard, E. Nelsen, N. Madaan, N. Brummelhuis, C. Diehl, H. Schlaad, R. Davis, M. Linford, *Langmuir* **2010**, *26*, 1923.
[18] J. Justynska, Z. Hordyjewicz, H. Schlaad, *Polymer* **2005**, *46*, 12057.
[19] C. Konak, V. Subr, L. Kostka, P. Stepanek, K. Ulbrich, H. Schlaad, *Langmuir* **2008**, *24*, 7092.
[20] N. Brummelhuis, C. Diehl, H. Schlaad, *Macromolecules* **2008**, *41*, 9946.
[21] C. Hoyle, C. Bowman, *Angew. Chem.* **2010**, *49*, 1540.
[22] C. Decker, T. Nguyen, *Polymer* **2000**, *41*, 525.
[23] X. Sui, L. Ingen, M. Hempenius, G. Vancso, *Macromol. Rapid Commun.* **2010**, *31*, 2059.
[24] A. Wolfberger, B. Rupp, W. Kern, T. Griesser, C. Slugovc, *Macromol. Rapid Commun.* **2011**, *32*, 518.
[25] T. Roper, C. Guymon, E. Jönsson, C. Hoyle, *J. Polym. Sci A.* **2004**, *42*, 6283.
[26] A. Alibeik, A. Rizkalla, K. Mequanint, *Eur. Polym. J.* **2007**, *43*, 1415.
[27] L. Schulte, A. Grydgaard, M. Jakobsen, P. Szewczykowski, F. Guo, M. E. Vigild, R. H. Berg, S. Ndoni, *Polymer* **2011**, *52*, 422.
[28] P. Szewczykowski, *PhD Thesis*, Technical University of Denmark, Denmark **2009**.
[29] J. Rabek, *Photodegradation of Polymers: Physical Characteristics and Applications*, Springer, Berlin, Germany **1996**, Chapter 6.

Appendix D

Kaushal Sagar, Nimi Gopalakrishnan, Mads Brøkner Christiansen, Anders Kristensen and Sokol Ndoni, Photolithographic fabrication of solid-liquid-core waveguides by thiol-ene chemistry, *Journal of Micromechanics and Microengineering* **2011**, *21,* doi:10.1088/0960-1317/21/9/095001

J. Micromech. Microeng. **21** (2011) 095001 (6pp) doi:10.1088/0960-1317/21/9/095001

Photolithographic fabrication of solid–liquid core waveguides by thiol-ene chemistry

Kaushal Sagar[1], Nimi Gopalakrishnan[2], Mads Brøkner Christiansen[2], Anders Kristensen[2] and Sokol Ndoni[2]

[1] Department of Chemical and Biochemical Engineering, Technical University of Denmark, Denmark
[2] Department of Micro- and Nanotechnology, Technical University of Denmark, Denmark

E-mail: mads.christiansen@nanotech.dtu.dk and sond@nanotech.dtu.dk

Received 28 April 2011, in final form 1 July 2011
Published 27 July 2011
Online at stacks.iop.org/JMM/21/095001

Abstract
In this work we demonstrate an efficient and cleanroom compatible method for the fabrication of solid–liquid core waveguides based on nanoporous polymers. We have used thiol-ene photo-grafting to tune and pattern the hydrophilicity of an originally hydrophobic nanoporous 1, 2-polybutadiene. The generated refractive index contrast between the patterned water-filled volume and the surrounding empty hydrophobic porous polymer allows for light confinement within the water-filled volume—the solid–liquid core. The presented fabrication process is simple and fast. It allows a high degree of flexibility on the type and grade of surface chemistry imparted to the large nanoporous area depending upon the application. The fabrication does not need demanding chemical reaction conditions. Thus, it can be readily used on a standard silicon lithography bench. The propagation loss values reported in this work are comparable with literature values for state-of-the-art liquid-core waveguide devices. The demonstrated waveguide function added to the nanoporous polymer with a very high internal surface area makes the system interesting for many applications in different areas, such as diagnostics and bio-chemical sensing.

(Some figures in this article are in colour only in the electronic version)

1. Introduction

Growing interest in the field of optofluidics has resulted in a continuous thrust toward more compact and robust lab-on-a-chip devices. This requires the integration of both fluidics and optical elements on the same chip. For maximum integration and functionality, fluidic channels are used for guiding light and liquid through the same physical volume known as liquid-core waveguides (LCWs) [1, 2]. The overwhelming majority of LCWs is based on the principle of total internal reflection with the liquid core having a higher refractive index than the surrounding cladding material. A class of fluorinated polymers, such as Teflon AF, has been successfully used as cladding in LCWs by many research groups for various chemical and biological applications [3]. Other index-guiding LCWs are fabricated using nanoporous cladding, liquid–liquid core (L^2) waveguides and slot waveguides [4]. Another class of LCWs based on interference is photonic crystal fibers and antiresonant reflecting optical waveguides (ARROWs) [5].

In previous work, we have demonstrated a novel approach for the fabrication of solid–liquid core waveguides (SLCWs) made from nanoporous polymers [6]. The original SLCWs were prepared by hydrophilizing a selective part of the large polymer–air interface of an originally hydrophobic nanoporous polymer by photo-oxidation in the presence of an appropriate lithographic mask under UV. Water exclusively fills the hydrophilic region generating refractive index contrast with the surrounding hydrophobic nanoporous volume filled with air, due to the low-refractive-index air-filled nanoporous polymer surrounding the high-refractive-index water-filled nanoporous core; light guiding takes place under the conditions of total internal reflection. In the present work, we use thiol-ene photo-grafting replacing photo-oxidation approach for hydrophilization of the polymer surface. Surface

modification of the pore wall is done in a nanoporous 1, 2-polybutadiene polymer. Compared to the original SLCWs, the performance of the SLCWs prepared by thiol-ene chemistry has been improved (up to 60%). Thiol-ene reaction is increasingly finding applications in photolithography and micro device fabrications due to its ability to form uniform networks, lower shrinkage and shrinkage stress [7, 8]. The reaction is also quantitative in nature with low oxygen inhibition [9]. Thiol-ene-assisted surface modification has been used for patterning by self-assembled structures using UV photolithography [10, 11].

Photo-grafting of thiol compounds containing hydrophilic groups onto the nanopores' wall results in tuning the hydrophilicity of the polymer. It is performed using standard UV I-line exposure and appropriate lithographic masks. Thus, the process is cleanroom compatible and can be carried out on a standard photolithography bench. It is a fast, clean and robust approach to waveguide fabrication compared to our previous approach of photo-oxidation. It does not need stringent reaction conditions like many traditional chemical reactions. The advantage of using this system is the great degree of flexibility. Thus, it can be used for a variety of thiol molecules depending upon the application without considerable changes in the fabrication protocol.

2. Waveguide fabrication

SLCW fabrication is carried out in three major steps: (1) fabrication of nanoporous 1, 2-polybutadiene polymer films, (2) thiol-ene grafting on the polymer–air interface in the selective volume and (3) a washing step to remove the unreacted thiol from the nanoporous polymer. The second and third steps are performed in a class 100 cleanroom-UV lithography section to avoid contamination and possible overexposure.

2.1. Nanoporous 1, 2-polybutadiene film preparation

The detailed procedure of preparation of a nanoporous polymer can be found elsewhere [12]. A nanoporous polymer is derived from an anionically synthesized 1, 2-polybutadiene-*b*-polydimethylsiloxane (1,2-PB-*b*-PDMS) di-block copolymer. The copolymer solution is prepared in tetrahydrofuran, THF (Sigma Aldrich), with dicumyl peroxide (DCP) (Sigma Aldrich) which acts as a thermal cross-linking agent. Upon adequate mixing, the solution is solvent-casted over a single-side-polished 10 cm diameter silicon wafer (figure 1(*a*)). The silicon wafer is coated with a low-surface-energy fluorinated organosilane layer (tridecafluoro-(1,1,2,2)-tetrahydrooctyl-trichlorosilane or FDTS) using molecular vapor deposition (Applied Microstructures Inc. MVD 100). The low-surface-energy coating of 1–2 nm will avoid adhesion of the contacting polymer to the wafer surface. The silicon wafer is subjected to vacuum drying for 7 h in order to ensure complete drying of the polymer [12]. A dry block copolymer is sandwiched by placing another MVD-coated silicon wafer with 100 μm steel spacers in between to control the resulting polymer film thickness (figure 1(*b*)). The sandwich is pressed in a custom-built pneumatic compression press built in-house under vacuum for 30 min at 4 bar. In the next step, the silicon wafer sandwich is sealed in a steel cylinder filled with nitrogen and heated in an oven at 140 °C for 100 min to carry out cross-linking of the majority block 1,2-PB. At this temperature, the di-block copolymer self-assembles into a gyroid morphology which is captured by the cross-linking reaction. Inert atmosphere in the cross-linking cylinder is desired to avoid thermal oxidation of the polymer from oxygen radicals. The cross-linked polymer is subjected to chemical etching of the PDMS block using tetrabutylammonium fluoride (Sigma Aldrich, 1 M) in THF for 5 h. The film is further washed sequentially in THF and methanol and dried in vacuum (figure 1(*c*)).

2.2. Thiol-ene grafting on the polymer–air interface

Figure 2 shows chemical formulas for mercaptosuccinic acid (MSA) (Sigma Aldrich) and sodium mercaptoethanesulfonate (MESNA) (Sigma Aldrich) used for modification of the nanoporous polymer. 2, 2-dimethoxy-2-phenylacetophenone (DMPA) (Sigma Aldrich) is used as a photoinitiator [13]. MSA with two terminal carboxylic groups is a hydrophilic molecule along with a thiol group. Similarly MESNA consists of a sulfonated salt end group which makes it hydrophilic with a terminal thiol group on the other end. The MSA thiol solution is prepared in ethanol, whereas the MESNA solution is prepared in a 3:1 methanol and water mixture. Concentration of both the thiols is maintained at 500 mM and that of DMPA at 10 mM. Due care is taken to prevent any light contact with the thiol solution to avoid side reactions. The nanoporous polymer is immersed in the thiol solution for 30 min to facilitate loading of solution into the nanopores. Further, the thiol-loaded polymer is aligned with a photolithographic mask and placed in a chamber to carry out photochemistry (figure 3(*a*)). A flood exposure collimated source 1000 W Hg (Xe) (Newport) at I-line (7.65 $\pm$ 0.05 mW cm^{-2}) is used for the thiol-ene grafting.

As can be seen in figure 3(*b*), an oxidized black aluminum chuck is used to hold the lithography mask. This will ensure absorption of UV light passing through the 100 μm thick polymer film by an antireflecting surface. This avoids uncontrolled exposure of the sample from the rear side. The reaction is carried out at 22 $\pm$ 1 °C in the cleanroom.

The thiol-ene reaction is schematically depicted in figure 1(*d*). The photo-grafting reaction begins in the nanopores loaded with thiol and photoinitiator in the region exposed to UV. UV light at 365 nm excites DMPA generating radicals which trigger thiol radical formation. The thiol radicals selectively attack the pendant double bond in the 1, 2-polybutadiene polymer available at the pore wall. Upon grafting thiols onto the pore wall, the opened double bond results in the generation of another thiol radical by the hydrogen abstraction mechanism. The reaction is insensitive to oxygen which makes the conditions less stringent. The reaction time for MSA is 30 min and for MESNA it is 5 min. During the course of reaction, the polymer is in constant contact with an excess of thiol solution in the case of MSA. This prevents crystallization of MSA and DMPA in

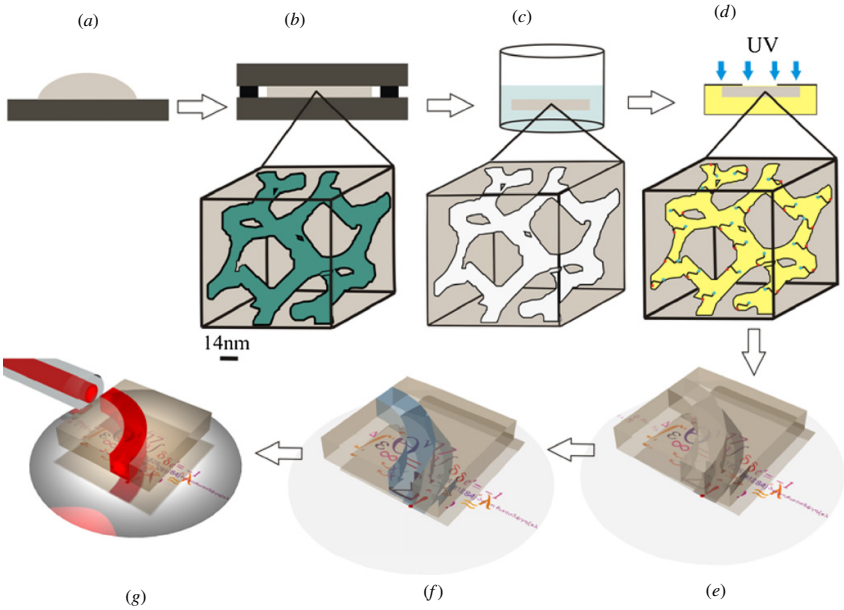

Figure 1. Fabrication process of SLCWs derived from a nanoporous polymer. (*a*) Solvent casting of the polymer on the silicon wafer. (*b*) Sandwiching polymer between silicon wafers and thermal cross-linking. (*c*) Chemical etching of the polymer. (*d*) Thiol-ene photo-grafting under UV. (*e*) Washing of the unreacted thiol solution. (*f*) Filling of water in the hydrophilic core volume. (*g*) Light guiding through the SLCW.

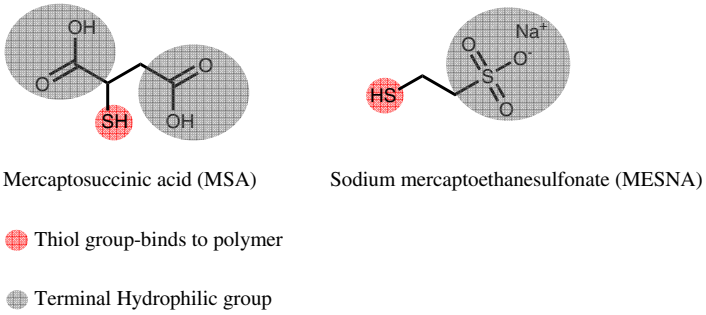

Figure 2. Chemical formulas of the thiol molecules used for photo-grafting.

the pore volume. The same MSA and DMPA concentration is maintained in the excess solution to prevent possible concentration-driven transport of chemicals out of nanopores. In the case of MESNA, no excess solution is required to keep the polymer in wet condition due to limited solvent evaporation during the much shorter irradiation time needed.

2.3. Washing of the nanoporous polymer for excess of thiol solution

After UV exposure, the polymer is removed from the mask and subjected to the washing step. The exposed polymer sample in the MSA solution is ultrasonicated in pure ethanol for 1 h (figure 1(*e*)). This process is carried out in the cleanroom or in a dark room outside with due care to avoid any post-reaction. It is further washed in fresh ethanol for 1 h followed by final THF sonication for 30 min. A similar washing procedure is followed for MESNA in a methanol water mixture and the final wash is done in THF. After adequate drying under vacuum, the samples are loaded with water for waveguiding.

3. Results on surface modification

To measure the degree of completion for the reaction, percentage water uptake is plotted against the exposure time in figure 4. Water uptake is used as a measure of development of the thiol-ene reaction; the results are presented in the form of a contrast curve. This kind of study will provide valuable information about the hydrophobic to hydrophilic transition. The transition from no water uptake to full water uptake will allow us to predict its suitability for photolithographic

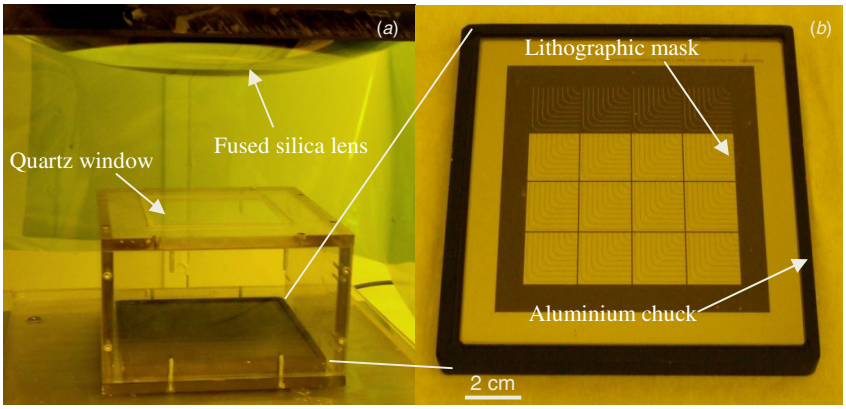

Figure 3. Setup for thiol-ene photochemistry. (*a*) Dedicated chamber for thiol-ene photo-grafting subjected to a collimated UV source. (*b*) Chuck containing a lithographic mask and an aligned polymer in the thiol solution.

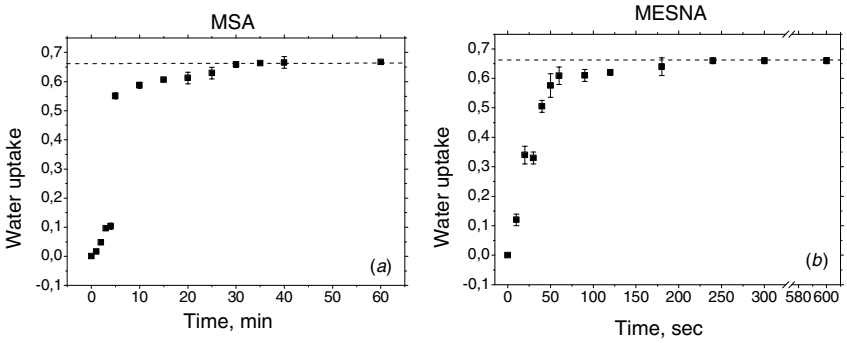

Figure 4. Contrast curves for MSA and MESNA.

patterning. All the reaction conditions are identical to the procedure described in the preceding section. The sample is aligned under the transparent part of the mask which results in a complete exposure of the sample to UV. Water uptake at different exposure times is obtained by gravimetry using the following relation:

$$\text{Water uptake after exposure time } t = \frac{m_{w,t} - m_n}{m_n},$$

where $m_{w,t}$ is the mass after equilibrium water uptake for the sample exposed to UV for a time interval t, and m_n is the mass of the original nanoporous polymer.

The water uptake is calculated with reference to the mass of the pristine nanoporous sample. The estimated specific porosity of the nanoporous polymer after PDMS etching is 0.67 $cm^3\ g^{-1}$. Figure 4(*a*) represents the MSA system for irradiation times between 0 and 60 min. There is no considerable water uptake between 0 and 4 min of exposure time. After 5 min of UV exposure, the samples register a water uptake of 0.55. This demonstrates a sharp contrast for MSA. Water uptake saturates at about 0.67 after 30 min of irradiation time. In the case of MESNA (figure 4(*b*)), the contrast curve shows that the water uptake value reaches to 0.61 after 60 s of irradiation. The rate of uptake reduces after that and reaches to the value of 0.67 after 4 min. Thus, the MESNA thiol system results in a faster reaction compared to MSA. The saturation level of water uptake is the same for both the MSA and MESNA modified samples; it is compatible with complete filling of the available pore volume with water when account is taken of the volume occupied by the grafted thiols.

4. Results on optical characterization

The propagation loss of the waveguides is determined using cutback techniques [6]. In our case, a UV mask is designed with a series of repeating 90° bend waveguides. The radius of curvature is 3 mm for all waveguides, which have different straight propagation lengths. The cross sections of the waveguides are 100 μm × 100 μm, and total lengths range from 4 to 32 mm (see the inset of figure 6).

When immersed in DI water for 5 min, the pores in the UV exposed regions get filled with water, changing the effective refractive index from 1.26 to 1.43. The device is sandwiched between two 100 μm thick low-refractive-index (1.38) fluorinated ethylene propylene (FEP) sheets. These sheets are supported on both sides by 5 mm thick polycarbonate blocks. Such a sandwich design makes handling of the 100 μm thin devices easier. In addition to

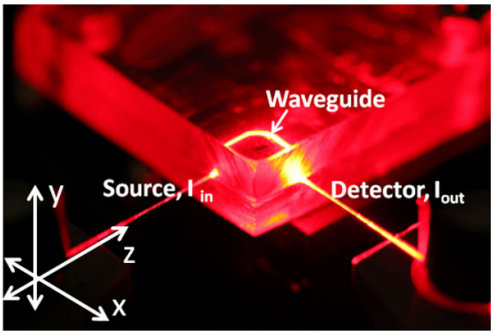

Figure 5. Experimental setup used for the propagation loss measurement of the SLCW. The waveguide device is placed between FEP sheets in a polycarbonate holder.

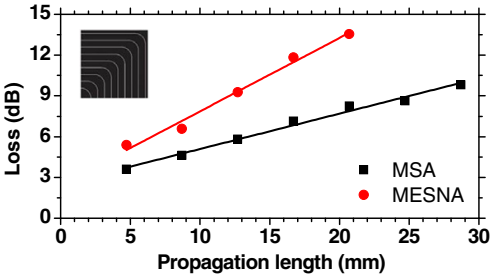

Figure 6. Loss in SLCWs with different lengths as a function of the propagation length. (Inset) 2 cm × 2 cm UV mask design used for loss measurement.

robustness to the system, evaporation problems observed [6] are also considerably reduced with a solid cladding. Moreover, the FEP sheets also reduce the clad–core index mismatch in the *Y*-direction.

A He–Ne laser beam (632.8 nm) is butt-coupled into the waveguide using a 62.5/125 μm multimode (MM) fiber. The light from the waveguide is collected using a 400 μm core MM fiber and guided to a photodiode (Ophir Electronics, PD 300) connected to a computer. Figure 5 shows the experimental setup used.

Propagation loss is evaluated by plotting losses (in dB) from waveguides as a function of the propagation length (figure 6). A linear fit to the data gives the propagation losses in these waveguides. The *Y*-intercept represents the coupling losses and transition losses due to propagation of light in different segments of waveguides (straight and bend sections). A propagation loss of 0.24 ± 0.01 dB mm^{-1} and coupling losses of 2.5 ± 0.2 are obtained in the MSA modified nanoporous SLCWs. In the case of MESNA modification, a propagation loss of 0.54 ± 0.03 dB mm^{-1} and coupling losses of 2.5 ± 0.5 are recorded. The polymer itself is transparent in the entire visible part of the spectrum. However, the attached molecules, in particular MESNA, absorb some light in the blue part of the spectrum, thus increasing the loss at short wavelengths.

5. Discussion and conclusion

In this work, thiol-ene photo-grafting is performed on nanoporous 1, 2- polybutadiene to induce selective hydrophilicity. The thiol-ene approach allows for an easy and efficient surface modification. Thiol-ene photo-grafting is very selective to double bonds. The compatibility of the SLCW fabrication process with cleanroom setup has been shown. It provides a considerable improvement over the photo-oxidation approach used in the previous work [6]. The method has reduced UV exposure time from 24 h in the case of photo-oxidation to 5–30 min in the present case, which is a considerable improvement in the fabrication of the devices. The simplicity of the surface modification approach and the huge surface area of the nanoporous polymer (283 ± 14 m^2 g^{-1}) allow for a high degree of grafting (up to 13 wt%) of thiol groups. The surface density of thiol molecules in the nanoporous system at full water uptake is 1.4–1.8 groups nm^{-2} [13]. The contrast curves in figures 4(*a*) and (*b*) show a rather sharp transition from the condition of almost no water uptake to 80% in MSA and 90% of available porosity in MESNA. The sharpness of the curve indicates a homogeneous process of surface modification, taking place in the entire sample simultaneously. The initial slow water uptake increase (more visible in figure 4(*a*), but also present in figure 4(*b*)) indicates that a certain critical surface density of hydrophilic groups is required for water uptake. Above this limit, the water fills considerable pore volume in the polymer. The high slope of the contrast curve is beneficial for achieving better edge definition after photolithography. This effect is observed in the propagation loss values. The propagation loss value reported in the case of MSA is 0.24 ± 0.01, and in the case of MESNA, it is 0.54 ± 0.03 dB mm^{-1}. These values are lower than those reported earlier (0.62 ± 0.03 dB mm^{-1}) by us with a photo-oxidation approach for surface modification [6]. This might be due to a number of reasons: reduced light scattering attributable to better edge definition could be one of them. Another reason may also be related to better control of the chemical reaction. The photo-oxidation approach formerly used yielded both a strongly heterogeneous modification degree relative to the sample depth and a number of undesired side reactions, which in some cases resulted in absorbed light in the blue part of the spectrum. The propagation loss values reported here are comparable with other state-of-the-art LCWs [14, 15].

Hydrophilization with MESNA is more efficient than in the case of MSA. However, the carboxylic acid end groups of MSA can serve as a favorable starting point for further chemical modification. The thiol-ene approach is versatile with a possibility of grafting different thiol molecules with varied functionality depending upon the application. In this way, the inner surface chemistry of the nanopores can be tailored, e.g. to provide selectivity in optical sensors.

Acknowledgment

This work is supported by the Danish Council for Strategic Reseach through the project LiCorT (grant no 09-063776/DSF) and by the respective Departments of Chemical

& Biochemical Engineering and of Micro and Nanotechnology at the Danish Technical University. MBC acknowledges financial support from the Danish Research Council for Technology and Production Sciences (grant no: 274-09-0105).

References

[1] Holger S and Hawkins A 2008 Optofluidic waveguides: I. concepts and implementations *Microfluid Nanofluid* **4** 3–16

[2] Dallas T and Dasgupta P 2004 Light at the end of the tunnel: recent analytical applications of liquid-core waveguides *Trends Anal. Chem.* **23** 385–92

[3] Datta A *et al* 2003 Microfabrication and characterization of Teflon AF-coated liquid core waveguide channels in silicon *IEEE Sensors J.* **3** 788–95

[4] Wolfe D, Conroy R, Garstecki P, Mayers B, Fischbach M, Paul K, Prentiss M and Whitesides G 2004 Dynamic control of liquid-core /liquid cladding optical waveguides *Proc. Natl Acad. Sci. USA* **101** 12434–8

[5] Hakanson U, Measor P, Yin D, Lunt E, Hawkins A, Sandoghdar V and Schmidt H 2007 Tailoring the transmission of liquid-core waveguides for wavelength filtering on a chip *Proc. SPIE* **6477** 647715-1–10

[6] Gopalakrishnan N, Sagar K, Christiansen M, Vigild M, Ndoni S and Kristensen A 2010 UV patterned nanoporous solid-liquid core waveguides *Opt. Express* **18** 12903–8

[7] Dickey M, Collister E, Raines A, Tsiartas P, Holcombe T, Sreenivasan S, Bonnecaze R and Willson C 2006 Photocurable pillar arrays formed via electrohydrodynamic instabilities *Chem. Mater.* **18** 2043–9

[8] Hagberg E, Malkoch M, Ling Y, Hawker C and Carter K 2007 Effects of modulus and surface chemistry of thiol-ene photopolymers in nanoimprinting *Nano Lett.* **7** 233–7

[9] Bowman C and Hoyle C 2010 Thiol-ene click chemistry *Angew. Chem., Int. Ed.* **49** 1540–73

[10] Besson E, Gue A, Sudor J, Youssoufi H, Jaffrezic N and Tardy J 2006 A novel and simplified procedure for patterning hydrophobic and hydrophilic SAMs for microfluidic devices by using UV photolithography *Langmuir* **22** 8346–52

[11] Crowe J and Genzer J 2005 Creating responsive surfaces with tailored wettability switching kinetics and reconstruction reversibility *J. Am. Chem. Soc.* **127** 17610–1

[12] Schulte L, Grydgaard A, Jakobsen M, Szewczykowski P, Guo F, Vigild M, Berg R and Ndoni S 2011 Nanoporous materials from stable and metastable structures of 1,2-PB-*b*-PDMS block copolymers *Polymer* **52** 422–9

[13] Berthold A, Sagar K and Ndoni S 2011 Patterned hydrophilization of nanoporous 1,2-PB by thiol-ene photochemistry *Macromol. Rapid Commun.*

[14] Papakonstantinou I, Wang K, Selviah D and Fernandez F 2007 Transition, radiation and propagation loss in polymer multimode waveguide bends *Opt. Express* **15** 669–79

[15] Lunt J, Wu B, Keeley M, Measor P, Schmidt H and Hawkins A R 2010 A hollow ARROW waveguides on self-aligned pedestals for improved geometry and transmission *IEEE Photon. Technol. Lett.* **22** 1147–9

The Danish Polymer Centre
Department of Chemical and Biochemical Engineering
Technical University of Denmark
Søltofts Plads, Building 227
DK-2800 Kgs. Lyngby
Denmark

Phone: +45 4525 2800
Web: www.dpc.kt.dtu.dk

ISBN : 978-87-92481-68-9